Chairman:	Prof. Dr. J. Manca Dean Faculty of Science UHasselt
Supervisor:	Prof. Dr. P. Wagner UHasselt
Co-supervisors:	Prof. Dr. K. Haenen UHasselt Dr. J. Vanacken K.U.Leuven
Members of the jury:	Prof. Dr. H.-G. Boyen UHasselt Dr. J.A. Garrido TU Munchen Prof. Dr. P.W. May University of Bristol Prof. Dr. V.V. Moshchalkov K.U.Leuven Prof. Dr. M. Nesladek UHasselt

Contents

Acknowledgements vii

List of abbreviations ix

Samenvatting xiii

I State of the art 1

1 Diamond 3
1.1 Allotropes of carbon . . . 3
1.1.1 Diamond . . . 3
1.1.2 From graphene to graphite and fullerenes . . . 5
1.1.3 Lonsdaleite . . . 5
1.2 Properties of diamond . . . 5
1.3 Classification of diamond . . . 6
1.3.1 Classification by impurity . . . 6
1.3.2 Polycrystalline diamond . . . 8

2 Diamond growth 11
2.1 High-pressure high-temperature (HPHT) . . . 12
2.2 Detonation . . . 12
2.3 Chemical vapor deposition (CVD) . . . 14
2.3.1 Substrate pretreatment . . . 15

II Theory, experiments and results 19

3 The surface of NCD 21
3.1 Contact angle measurements . . . 21
3.1.1 Law of Young-Dupré . . . 21
3.1.2 The ‘OWRK’ method . . . 22
3.2 Oxidation of B:NCD:H . . . 25
3.2.1 Experimental . . . 25
3.2.2 Results and conclusions . . . 27
3.3 The surface energy of NCD:H . . . 29
3.3.1 Introduction . . . 29

3.3.2 Experimental . . . 30
3.3.3 Results . . . 32
3.3.4 Conclusions . . . 40

4 Intrinsic NCD layers 41
4.1 Sample preparation . . . 41
4.1.1 Laser interferometry . . . 41
4.2 Morphology . . . 45
4.2.1 SEM . . . 45
4.2.2 AFM . . . 45
4.2.3 Raman . . . 48
4.3 Conclusion . . . 49

5 Electronic transport measurements 51
5.1 Theory . . . 51
5.1.1 Electronic resistance . . . 51
5.1.2 Electronic mobility . . . 52
5.1.3 Hall effect . . . 53
5.2 Noisy Hall effect measurements . . . 55
5.2.1 Introduction . . . 55
5.2.2 The evaluation of the Hall voltage . . . 55
5.2.3 Boron-doped nanocrystalline diamond . . . 58
5.2.4 Conclusions . . . 65

6 Heavily boron-doped NCD 67
6.1 Introduction . . . 67
6.2 Experimental . . . 67
6.3 Results and discussion . . . 68
6.3.1 Structural properties . . . 68
6.3.2 Electronic properties . . . 75
6.4 Conclusions . . . 83

7 Superconductivity in boron-doped diamond 85
7.1 Introduction . . . 85
7.2 Intrinsic/extrinsic granularity in superconducting B:NCD . . . 87
7.2.1 Electronic transport properties . . . 87
7.2.2 Magnetotransport properties . . . 89
7.2.3 Local study of superconductivity in B:NCD . . . 91
7.2.4 Conclusions . . . 94

8 A biological application of B:NCD in DNA sensors 95
8.1 Introduction . . . 95
8.2 Experimental . . . 96
8.3 Results and discussion . . . 96
8.4 Conclusion . . . 100

Bibliography 101

Publications **109**
Journals 109
Proceedings 110
Abstracts 111
Oral presentations 111
Poster presentations 114

Acknowledgements

After almost one year of job hopping I mailed Prof. Dr. P. Wagner for some information regarding a PhD position at UHasselt. I was astonished by the reply which was written in flawless Dutch and which made me think 'Is this guy really a German?'. Later on, only his German accent revealed his German roots. After an interview, Prof. Dr. Patrick Wagner, Dr. Ken Haenen (now professor) and Prof. Dr. Marc D'Olieslaeger (one of the big bosses at IMO) decided to give me the opportunity to make this thesis. I really thank them for this! Originally I applied for a position in theoretical chemistry since I had a background in this field but (un)fortunately, this job was already taken... Two other non-theoretical positions were suggested. The first position was biosensor related and the second position was diamond/superconductivity related. Due to my interests in physical chemistry, I preferred the second position. Who doesn't want to make diamonds which are superconducting? Ken and Patrick, I will never forget the time you invested in me! There are too many things to mention you did for me.

I strongly acknowledge the FWO for funding, especially Kim and Hans whom picked me, due to the crazy YouTube video (`http://youtu.be/-FKNUd2SkcA`), together with a bunch of young scientists to visit Torino and to be part of the ESOF experience.

Michael Daenen and Oliver Williams, I thank you guys for introducing me in the arts of diamond growth and Hall effect measurements. The knowledge transfer you made really catalyzed my work strongly. Milos Nesladek, thanks for helping my career by involving me in some nice research projects and to introduce me to interesting people! Hans-Gert Boyen, thanks for the interesting discussions during the PhD-meetings and the lessons in high vacuum techniques!

Johnny, thanks for maintaining and repairing all the devices and Johan, thanks for sharing your insights in life and for being Diepenbeek Customs!

For the co-operation with INPAC (KUL) which resulted in, and is still generating, nice publications I thank Prof. Dr. Victor Moshchalkov, Dr. Johan Vanacken, Dr. Bram Willems and Gufei Zhang. Gufei, thanks for taking this co-operation to the next level.

I appreciate the help of our Czech friends Jiri, Vladka, Vlacav, Andrew (Andy) and Frantisek Frendrych and hope to further collaborate with them. I ow you big time!

For the collaboration with Singapore, I thank Candy, Yu and Prof. Dr. Kian Ping Loh.

I also thank the organizers of the Matcon project for inviting me to the University of Oxford. I strongly suggest everyone to visit this historical place!

Vincent, Andrada, Wim Deferme, Diden, Yaso, Paulius, Wiebke, Ludwig, Sien, Wim Dexters, Pieter and Weng Siang, the ‘Wide Bandgappers’ I thank for creating a nice atmosphere and for the help in the lab.

I thank Lieven De Winter, the electronics whisperer; Jan Mertens, my labVIEW teacher; Ward Valve De Ceunick; Erik Thoonen, the only person I know who knows how PC’s really work; Christel Willems and Hilde Pellaers, the ones who watched over my mess with a lot of patience; Dany ‘Foreman’ Polus; Rerlinde Heymans, Lea Verboven and Lisette Luyckx, the guides of the administrative labyrinth; Bart Ruttens and Jan D’Haen, the SEM, TEM and XRD experts; the Bios (lunch and party) group, Ronald, Evy, Peter, Sylvia, Lars, Jan, Rob, Bart, Marloes, Mohammed, Kasper and Anitha; the One group; the researchers of the chemistry departments, Marlies Van Bael, Dirk Vanderzande, An Hardy, Christopher, Daan and Giedrius; the XIOS groep, Thijs, Tim, ...; The Biomed department, Veronique, Natalie, Luc Michiels; Marcel Ameloot; Prof. Dr. M.J. Shöning and his group.

All people I did not mention and helped me in one way or another I would also like to thank!

Last but not least I want to thank my parents, family and friends for the support and the time they took to listen to my gibberish.

Stoffel

List of abbreviations

AFM	atomic force microscopy
B:NCD	boron-doped nanocrystalline diamond
B:NCD:H	hydrogen terminated boron-doped nanocrystalline diamond
BCS	Bardeen Cooper and Schrieffer
BDD	boron-doped diamond
BEN	bias enhanced nucleation
BP	Base pair
c-NCD	‘cauliflower’-type nanocrystalline diamond
CP	Cooper pair
CVD	chemical vapor deposition
DC	direct current
DI	deionized
DLS	dynamic light scattering
DNA	deoxyribonucleic acid
DND	detonation nanodiamond
EELS	electron energy loss spectroscopy
EPR	electron paramagnetic resonance
FWHM	full width at half maximum
FWO	het Fonds voor Wetenschappelijk Onderzoek-Vlaanderen
HPHT	high-pressure and high-temperature
HRTEM	high-resolution transmission electron microscopy
IMO	Institute for Materials Research
INPAC	Institute for Nanoscale Physics and Chemistry
IR	infrared
MCD	microcrystalline diamond
MWPE	microwave plasma enhanced
NCD	nanocrystalline diamond
NCD:H	hydrogen terminated nanocrystalline diamond
NIMS	National Institute for Materials Science
NIRIM	National Institute for Research in Inorganic Materials
NMR	negative magnetoresistance
OWRK	Owens, Wendt, Rabel and Kaelble
PA	polyamide
PBS	phosphate buffered saline
PC	polycarbonate
PE	polyethylene

PMMA	polymethylmethacrylate
PMR	positive magnetoresistance
PP	polypropylene
PS	polystyrene
PTFE	polytetrafluoroethylene
PVC	polyvinyl chloride
QP	single-quasiparticle
RMS	root mean square
S/N	signal-to-noise ratio
SEM	scanning electron microscopy
SIT	superconductor-insulator transition
SNP	single nucleotide polymorphism
STM	scanning tunneling microscopy
STS	scanning tunneling spectroscopy
TEM	transmission electron microscopy
TMB	trimethylboron
TNT	2,4,6-trinitrotoluene
UDD	ultra-dispersed diamonds
UNCD	ultrananocrystalline diamond
UV	ultraviolet
VIS	visible
XPS	x-ray photoelectron spectroscopy
XRD	x-ray diffraction

W	work
γ	surface or interfacial energy
γ^D	disperse fraction of surface energy
γ^P	polar fraction of surface energy
A	surface area
SV	solid/vapor
SL	solid/liquid
LV	liquid/vapor
W_a	work of adhesion
A_{aa}	constant between like molecules
A_{ab}	constant between unlike molecules
ΔF^a_{ab}	free energy of adhesion for the interface between phases A and B
ΔF^n_c	free energy of cohesion for phase N
θ	contact angle
a	slope of a straight line
b	y-intercept of a straight line
n_D	refractive index of diamond
n_{plasma}	refractive index of CVD plasma during diamond growth
n_{air}	refractive index of air
d	thickness
α	angle from the normal of a surface to a light beam above the surface
β	angle from the normal of a surface to a light beam under the surface
m	integer

λ	wavelength
ρ	electronic resistivity
V_ρ	voltage difference for calculating ρ
w	width
I	current
s	length
τ	relaxation time
τ_L	collision time for scattering by phonons
τ_i	collision time for scattering by impurity imperfections
σ	conductivity
m_e	mass of an electron
n	electron density
Q	magnitude of the electronic charge
ρ_L	electronic resistivity caused by thermal phonons
ρ_i	electronic resistivity caused by scattering
q	elementary charge
p	positive charge carrier density
μ_n	mobility of negative charge carriers
μ_p	mobility of positive charge carriers
μ	mobility
μ_L	mobility for scattering by phonons
μ_i	mobility time for scattering by impurity imperfections
$\mathbf{F}$	force (vector)
$\mathbf{E}$	electric field (vector)
$\mathbf{v}$	velocity (vector)
$\mathbf{B}$	magnetic field (vector)
F	force
E	electric field
v	velocity
B	magnetic field
J	current density
J_e	current density of electrons
J_h	current density of holes
v_e	velocity of electrons
v_h	velocity of holes
μ_e	mobility of electrons
μ_h	mobility of holes
R_H	Hall coefficient
r	Hall scattering factor
V_H	Hall voltage
ΔV_H	error on Hall voltage
τ_{cd}	mean size of the crystalline domains
K	shape factor, depending on the shape of the crystallite
φ	line broadening for FWHM
θ_B	Bragg angle
d_{gs}	grain size
T_s	substrate temperature

$1/S(T)$	inverse of a slope of FIG. 6.8(a), plotted in FIG. 6.8(b)
T	temperature
E_a	experimental activation energy
$\rho_{[C/H],T}$	fraction of ρ which is temperature and C/H-ratio dependent
$\rho_{[C/H]=0}$	approximately T-independent fraction of ρ
$[C/H]$	carbon-to-hydrogen ratio
ρ_{SC}	resistivity of a heavily boron-doped single crystal diamond
ρ_{GB}	resistivity contribution of grain boundaries
$\mu_{[C/H]=0}$	approximately T-independent fraction of μ
$C(T)$	inverse of a slope of FIG. 6.9(b)
μ_{SC}	mobility of a heavily boron-doped single crystal diamond
μ_{GB}	mobility contribution of grain boundaries
n_{Hall}	active charge carrier concentration derived from Hall effect measurements
n_{NDP}	total boron concentration derived from neutron depth profiling
T_c	critical temperature for superconductivity
P	pressure
$R(T)$	resistance as a function of temperature
Δ	order parameter for superconductivity
t	time
$Z(t)$	impedance as a function of time
A_1	denaturation-related decay amplitude parameter (impedance)
τ_1	time constant associated with A_1 (impedance)
A_2	medium exchange-related decay amplitude parameter (impedance)
τ_2	time constant associated with A_2 (impedance)
I_t	intensity as a function of time (luminescence)
I_0	remnant background intensity (luminescence)
I_{DNA}	intensity of complementary DNA strand (luminescence)
τ_3	time constant associated with denaturation (luminescence)

Samenvatting

In dit werk ligt de focus op het groeien en het karakteriseren van dunne diamantlagen die vervaardigd zijn met 'chemical vapor deposition' (CVD). De bestudeerde diamantlagen hebben een maximale dikte van 200 nm, bestaan uit vele kristallieten met een gemiddelde diameter kleiner dan 100 nm en behoren tot het nanokristallijn diamant (NCD).

In het eerste hoofdstuk worden de structuur en de bijzondere eigenschappen van monokristallijn diamant beschreven. Aan de hand van het type onzuiverheden (stikstof, boor) en de hoeveelheid onzuiverheden wordt een classificatie gemaakt voor dit mono-kristallijn diamant. Ook polykristallijn diamant wordt besproken en opgedeeld in hoofdzakelijk microkristallijn en nanokristallijn diamant. Microkristallijn diamant bevat kristallieten die gemiddeld groter zijn dan 500 nm en nanokristallijn diamant bevat kristallieten die gemiddeld kleiner zijn dan 500 nm.

In het tweede hoofdstuk wordt dieper ingegaan op het vervaardigen van synthetisch diamant. Monokristallijn diamant wordt het makkelijkst vervaardigd onder hoge druk en hoge temperatuur (HPHT) maar is helemaal niet zo zuiver als CVD diamant. Het kan wel gebruikt worden als basis om een zeer zuivere CVD diamantlaag op af te zetten. Dunne diamantlagen worden voornamelijk vervaardigd door een geschikt staal (silicium, zuiver glas, ...) onder te dompelen in een suspensie van detonatie diamant-korrels welke een gemiddelde diameter van $5 - 10$ nm hebben. Een enkelvoudige laag van deze korrels blijft na spoelen met water over en kan dan met behulp van CVD uitgroeien tot een gesloten NCD-laag. De groei gebeurt op relatief lage temperatuur (≈ 800°C) en op lage druk (≈ 30 mbar). Een overvloed aan waterstofgas en een beetje methaangas (0.5% tot 10%) worden met behulp van microgolven tot een plasma gebracht waardoor het kristalrooster van het diamant wordt uitgebreid. Dit gebeurt door een aaneenschakeling van complexe radicalaire chemische reacties. Door de additie van andere gassen kan men systematisch onzuiverheden toevoegen in het kristalrooster van diamant. In dit werk werd trimethylboraan (TMB) gebruikt om boorgedoteerd diamant (B:NCD) te vervaardigen. Deze p-type dotering is 0.37 eV boven de valentieband gelegen en zorgt voor de blauwe kleur van het diamant en voor elektrische geleiding. Concentraties van bijna 10^{22} cm^{-3} kunnen worden behaald en bij concentraties van $10^{20} - 10^{21}$ cm^{-3} ligt de isolator−metaal transitie. Boven deze transitie wordt diamant supergeleidend op temperaturen lager dan 12 K.

In het eerste deel van hoofdstuk drie wordt nagegaan hoe sterk gedoteerde en wa-

terstof getermineerde B:NCD lagen, gegroeid op zuiver glas, gereinigd kunnen worden met een sterk oxiderend mengsel. Dit onderzoek werd uitgevoerd aangezien meerdere keren werd vastgesteld dat sterk boorgedoteerde lagen aangetast worden en afbladeren tijdens het reinigen op hoge temperaturen met een sterk oxiderend mengsel. Het gebruikte oxiderende mengsel bestaat uit 100 ml 95% zwavelzuur (H_2SO_4) en 50 gr kaliumnitride (KNO_3) verdunt met 100 ml water. Gedurende het oxidatieproces, werden de stalen en het mengsel op een matige 95°C gehouden gedurende 17 uur. Contacthoekmetingen met waterdruppels werden voor, na 3 uur en na 17 uur reageren uitgevoerd. De lagen bleken volledig intact te zijn en een sterke daling in contacthoek werd waargenomen. Een niet destructieve methode voor het reinigen en het oxideren van een oppervlak van een sterk gedoteerde B:NCD laag werd bekomen.
In het tweede deel van hoofdstuk 3 wordt aan de hand van de Owens, Wendt, Rabel en Kaelble ('OWRK') methode de oppervlakte-energie van waterstof beëindigde NCD (NCD:H) lagen bepaald. Eerst worden druppels van zuivere vloeistoffen afgezet op het NCD:H waaruit de contacthoeken worden opgemeten. Met de gekende disperse en polaire oppervlakte-energieën van deze vloeistoffen en met de gemeten waarden van de contacthoeken die ze maken met NCD:H wordt de waarde van de oppervlakte-energie van NCD:H berekend (34 ± 5 mN/m). In een tweede experiment worden alcohol(ethanol)/water mengsels gebruikt met waarden voor de disperse en de polaire oppervlakte-energieën bekomen door Hong en Chen. De waarde van de oppervlakte-energie voor NCD:H (30 ± 10 mN/m) is ongeveer dezelfde als in het voorgaande experiment maar de fout erop is een stuk groter. In het derde experiment gaan de oppervlakte-energieën van de alcohol/water mengsels bepaald worden door ijking op oppervlakken van verschillende polymeren met gekende oppervlakte-energieën. In het tweede experiment is dit volgens de literatuur op slechts één polymeer uitgevoerd. De waarde van de berekende oppervlakte-energie van NCD:H (16 ± 2 mN/m) bevat nu een groot polair deel wat niet meteen verwacht wordt en is ongeveer halveert in waarde. In een laatste experiment worden de oppervlakte-energieën van de polymeren die gebruikt werden voor het ijken van de alcohol/water mengsels eerst geijkt met zuivere vloeistoffen wat uiteindelijk dezelfde waarde voor de oppervlakte-energie van NCD:H (16 ± 4 mN/m) als in experiment drie oplevert. De verhoogde polaire component van de oppervlakte-energie in de laatste twee experimenten is hoogst waarschijnlijk te wijten aan een grotere affiniteit van alcohol voor het oppervlak van NCD:H waardoor de oppervlakte-energie van een alcohol/NCD:H oppervlak in plaats van een NCD:H oppervlak wordt opgemeten. Uit de laatste experimenten kan besloten worden dat de bepaling van een oppervlakte-energie aan de hand van contacthoekmetingen best met zuivere vloeistoffen en niet met alcohol/water mengsels uitgevoerd wordt.

Hoofdstuk vier handelt over ongedoteerde (intrinsieke) NCD lagen van 150 nm dik, gegroeid met verschillende vaste methaanconcentraties (0.5%, 1%, 2%, 4%, 8%). De groeisnelheid neemt behoorlijk toe als functie van de gebruikte methaanconcentratie en werd tijdens de groei gemonitord aan de hand van lazer interferometrie. Op SEM en AFM afbeeldingen is duidelijk zichtbaar dat de diamantkristallieten afnemen in grootte als functie van de methaanconcentratie. Door deze afname in korrelgrootte gaat ook de ruwheid afnemen. Op Raman spectra is een duidelijke in-

tensiteitafname voor de diamantpiek als functie van de methaanconcentratie zichtbaar. Dit is in overeenstemming met de toename van korrelgrenzen voor lagen met kleinere kristallieten. NCD van hoge diamantkwaliteit wordt dus gemaakt met lage methaanconcentraties.

Het vijfde hoofdstuk is gewijd aan het opmeten van moeilijk opmeetbare Hall voltages. Een methode waar gewerkt wordt met een alternerend magneetveld is volledig beschreven inclusief foutberekening. De bekomen formules zijn toegepast op de meetresultaten, bekomen op een dunne (≈ 150 nm) en sterk gedoteerd B:NCD ($\approx 10^{21}$ cm^{-3}) laag. Het Hall voltage van de laag is lineair als functie van het magneetveld tussen 0.1 T en 2.0 T. Bij de lage magneetvelden gaat het Hall voltage op in de ruis maar door meermaals te meten en de bekomen formules toe te passen is het mogelijk een significant signaal te bekomen. Ook een vergelijkende studie tussen 'slechte' zilververf contacten en 'goede' ohmische Ti/Al contacten is uitgevoerd. Hieruit blijkt dat de signaal tot ruisverhouding (S/N) bij de goede contacten bijna tien maal hoger is.

Een systematische studie van de morfologie en de elektronische eigenschappen van sterk boorgedoteerde dunne NCD lagen wordt gepresenteerd in hoofdstuk zes. Deze lagen hebben ongeveer dezelfde dikte (≈ 150 nm), zijn gegroeid met een vaste B/C-verhouding (5000 ppm) maar met verschillende C/H-verhoudingen ($1-5\%$) in de gasfase. De morfologie van de lagen is bestudeerd met XRD, AFM en SEM metingen die bevestigen dat lagere C/H-verhoudingen leiden tot lagen waarin kristallieten gemiddeld groter zijn. Magnetotransport metingen onthullen een verlaging in de resistiviteit en een sterke stijging in de mobiliteit, welke de waarden van sterk gedoteerd monokristallijn diamant benaderen bij een stijging van de gemiddelde korrelgrootte van de lagen. In alle lagen daalt de temperatuursafhankelijkheid van de resistiviteit als functie van de korreltgrootte en is de mobiliteit thermisch geactiveerd. Het is mogelijk om de intra- en intergranulaire contributies voor de resistiviteit en de mobiliteit te scheiden wat erop wijst dat voor deze complexe systemen Matthiessens's rule toepasbaar is. De concentratie van de actieve ladingsdragers is gereduceerd wanneer het B:NCD gegroeid wordt met een lagere C/H-verhouding. Dit is te wijten aan een lagere boorincorporatie en is bevestigd met 'neutron depth profiling' (NDP) en op basis van kritische temperaturen voor supergeleiding.

In de laatste twee hoofdstukken wordt een korte samenvatting gegeven over de onderzoeksresultaten bekomen door andere onderzoeksgroepen op NCD lagen, vervaardigd op IMO.
Hoofdstuk zeven handelt over de elektromagnetische eigenschappen van sterk boorgedoteerde NCD lagen op lage temperatuur (< 80 K). Het lijkt erop dat supergeleiding in granulair materiaal kan zorgen voor een verhoging van de resistiviteit onder invloed van hoge magneetvelden. Om locale eigenschappen op te meten werd 'Scanning Tunneling Microscopy and Spectroscopy' (STM/S) toegepast en deze metingen geven aan dat de supergeleiding lokaal zeer inhomogeen is.
In hoofdstuk acht wordt beschreven hoe men met boorgedoteerd NCD een stabiele en zeer gevoelige DNA sensor kan vervaardigen. Doormiddel van tijdsafhankelijke impedantiemetingen tijdens een denaturatieproces kan men bepalen indien een stukje DNA al dan niet een puntmutatie bevat.

Part I

State of the art

Chapter 1

Diamond

This chapter gives an overview of carbon allotropes with a detailed description of diamond, one of the allotropes. It is explained how to build the crystallographic structures of the allotropes, starting from sp^2 and sp^3 hybridised carbon atoms. When the structure of the allotropes is known, the classification of single crystal diamond is explained. In the last section of this chapter, thin polycrystalline diamond films are discussed.

1.1 Allotropes of carbon

Carbon atoms can arrange themselves in an infinite number of ways but only three crystallographic structures are possible: hexagonal graphite, cubic diamond and hexagonal lonsdaleite (hexagonal diamond). These crystallographic structures are presented in FIG. 1.1 together with the most important allotropes of carbon. These allotropes or a combination of them can be used to build a variety of materials with remarkable properties.

1.1.1 Diamond

Diamond is the first allotrope which is discussed. In order to build a diamond lattice with a ball-and-stick model, all carbon atoms should be sp^3 hybridised. The four orbitals of one carbon atom take as much as space as possible which results in the formation of a tetrahedron. Each orbital points towards one corner of the tetrahedron and the positive carbon core is placed in the center. By attaching the corners of such tetrahedrons, the diamond lattice is formed and all carbon atoms are connected through rigid σ bonds which partly explains some of the remarkable properties of diamond. Between the σ bonds, an angle of 109° 28’ exists, the distance between two neighboring carbon atoms is 1.54 Å and the carbon concentration is $17 \cdot 10^{22}$ cm^{-3}. The cubic unit cell of diamond is shown in FIG. 1.2 [1].

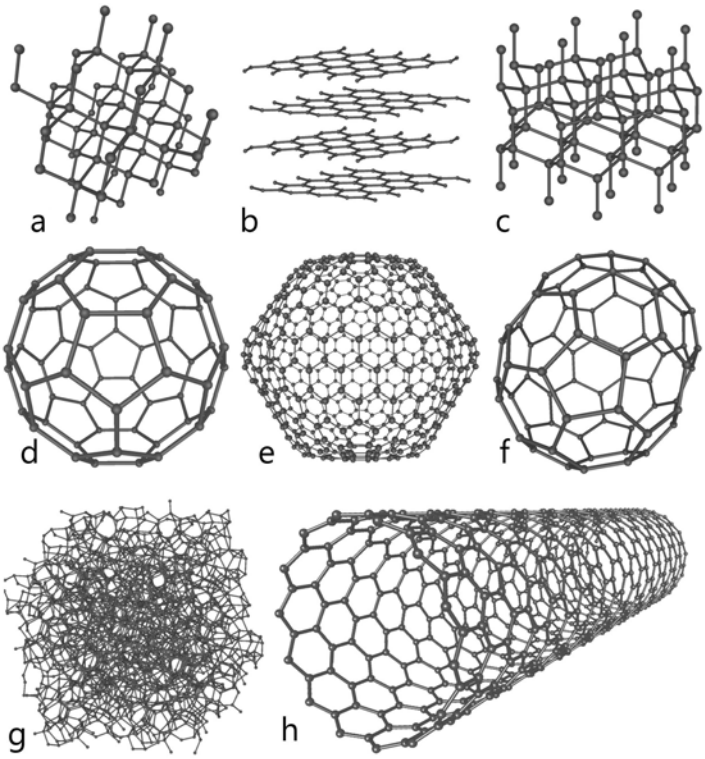

Figure 1.1: Eight allotropes of carbon: a) Diamond, b) Graphite (n-graphene), c) Lonsdaleite, d) C_{60} (Buckminsterfullerene or buckyball), e) C_{540}, f) C_{70}, g) Amorphous carbon, and h) single-walled carbon nanotube or buckytube. This figure was created by Michael Ströck.

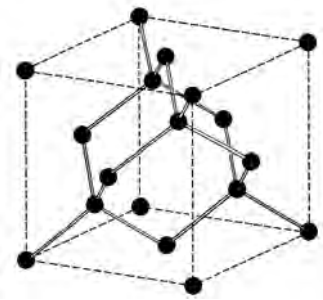

Figure 1.2: The crystal structure of diamond, showing the tetrahedral bond arrangement.

1.1.2 From graphene to graphite and fullerenes

To explain the structure of graphite, it is convenient to start with the explanation of the graphene structure. Graphene is a sheet of sp^2 hybridised carbon atoms. All atoms are attached to each other by σ and π bonds which form a two dimensional honeycomb crystal lattice (hexagonal lattice). When piling the graphene sheets on top of each other at a distance of 3.35 Å, one gets the graphite structure as displayed in FIG. 1.1b. Between each bond, an angle of 120° exists and the average distance between two neighboring carbon atoms in a graphene sheet is about 1.42 Å. The graphene sheets are attached by weak van der Waals interactions, which explains the use of it in pencils. When a graphene sheet is folded in the form of a hollow sphere, ellipsoid or tube, a fullerene is made (FIG. 1.1(d), (e), (f), (h)).

1.1.3 Lonsdaleite

Lonsdaleite (named in honour of Kathleen Lonsdale) resembles diamond since it is also built from sp^3 hybridised carbon atoms. The difference lies in the crystal structure since diamond has a cubic unit cell and lonsdaleite has a hexagonal unit cell. The diamond structure can also be built from rings of six carbon atoms, in the chair conformation. In lonsdaleite, some of the rings are in a less energetically stable boat conformation (FIG. 1.3).

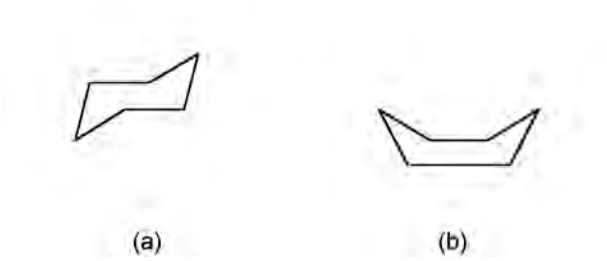

Figure 1.3: The chair (a) and the boat (b) conformations.

1.2 Properties of diamond

In TAB. 1.1, the properties of a perfect single crystal diamond are presented together with the properties of a perfect silicon crystal. It is clear that diamond surpasses silicon in all fields. There are three main reasons why it is not used in microelectronics. First, the use of natural diamond for applications is limited due to the extremely high prices and the near-impossibility to tailor the crystals to workable shapes and sizes. Secondly, natural diamond contains lots of defects which reduces the properties of diamond listed in TAB. 1.1 [2, 3, 4]. Thirdly, the lack of a shallow n-type counterpart for the natural p-type diamond reduces the exploitation of diamond in the field of electronics. All these factors make the practical application of natural diamond nearly impossible. Over the last two decades, the production of synthetically tailored

single crystal and polycrystalline diamond is strongly enhanced. This makes fundamental research possible which delivers the knowhow of creating diamond based devices.

Table 1.1: Overview of some properties of diamond and silicon at room temperature and superconducting properties at low temperatures [2, 3, 4, 5].

Properties	Diamond	Silicon
Thermal expansion (10^{-6} K^{-1})	1.1	2.6
(Linear coefficient)		
Indirect band gap (eV)	5.45	1.1
Carrier mobility ($cm^2V^{-1}s^{-1}$)		
Electron	4500	1500
Hole	3800	600
Breakdown voltage (10^5V cm^{-1})	100	3
Dielectric constant	5.5	11.8
Resistivity (Ω cm)	10^{13}	10^3
Thermal conductivity (W cm^{-1} K^{-1})	20	1.5
Refractive index	2.42	3.5
Hardness (GPa)	98	9.8
Critical temperature for superconductivity (K)	≈ 9	≈ 0.35
(Boron concentrations > $10^{21}cm^{-3}$)		

1.3 Classification of diamond

In this section, the first classification of diamonds is done by the type and the concentrations of impurities. IR spectroscopy turns out to be the most reliable technique for a reliable classification.
The second classification is done by crystallinity, derived from crystallite size and the concentration of other than sp^3 hybridised carbon atoms in polycrystalline diamonds.

1.3.1 Classification by impurity

In 1934, Robertson et al. [6] proposed a way to make a physical classification of diamond. This classification is based on optical measurements which are dominated by nitrogen defects. This is no surprise since roughly 98% of all diamonds contain nitrogen [7]. Later in 1965, a first definite classification of the modern type was given by Dyer et al. [8]. Different classifications based on physical properties, structure and mineralogy prove to be less useful [9].

Type I

When diamonds contain more than 5 ppm of nitrogen, they can be classified as type I. About 78% of all natural diamonds fall in this class and in the next paragraphs, a more detailed classification is presented.

Type Ia This type of diamonds mainly contain non-paramagnetic aggregated nitrogen. To be of pure type Ia, diamond should contain single substitutional nitrogen atoms in concentrations below 10^{16} cm^{-3} [10].
The most important subtypes (IaA, IaB and IaB') are named after the aggregates that are predominantly present in each of the diamonds.
The A center is probably the most common defect in natural diamonds and consists of a nearest-neighbor pair of nitrogen atoms substituting for the carbon atoms. When this diamagnetic center is ionized by UV or deep acceptors, it produces an EPR spectrum which unambiguously proves the N=N structure [11]. When this center is irradiated with IR light, the absorption spectrum has no sharp features, which is distinctively different from the B or C centers. The strongest peak is at 1282 cm^{-1} and is routinely used to estimate the nitrogen concentration in this form [12]. Since no absorption is present in the visible light area, this center is colorless.
The B center consists of a carbon vacancy surrounded by four nitrogen atoms which substitute carbon atoms [13]. It has a characteristic IR absorption spectrum with a sharp peak at 1332 cm^{-1} and a broader peak at 1280 cm^{-1}. Also this center is colorless.
The B' class predominantly contains planar defects in the (100) lattice planes, which are called platelets. These nanometer to micrometer structures were falsely associated with large nitrogen complexes which puts this class historically here. A direct measurement of nitrogen with EELS revealed a very low nitrogen concentration in those platelets [14]. They also produce sharp absorption peaks at $1359 - 1375$ and 330 cm^{-1} in IR absorption spectra. The position of the first peak seems to depend on the platelet size [14].

Type Ib This type of diamonds mainly contain paramagnetic single substitutional nitrogen atoms which are also called C centers. EPR spectra easily detect these C centers [15]. The extra electron which is not chemically bonded acts as a deep donor and radiation with energy greater than 2.2 eV can excite this donor into the conduction band [16]. Therefore, these centers are colored yellow and diamonds which contain them are commonly known as 'canary diamonds'. The yellow color is already observable when a concentration of 10 ppm is exceeded [17]. A sharp peak at 1344 cm^{-1} and a broader feature at 1130 cm^{-1} are observed by IR spectroscopy.

Type II

When a diamond contains less than 5 ppm of nitrogen, it can be classified as type II. This low nitrogen concentration makes no nitrogen-related optical absorption nor paramagnetic signals appear. Historically, type II diamonds are optical transparent up to 230 nm [6].

Type IIa This is the purest form of diamond and is electronically insulating. Only vibrations of the almost non-disturbed diamond lattice are observed [18].

Type IIb This type of diamonds contain boron as an extrinsic substitutional impurity. Only 1% of natural diamonds contain boron and most are blue to gray [19]. In FIG. 1.4 one can see a series of medium to heavy boron-doped diamond films, synthetically produced at IMO. These films have a thickness of 100 nm and are more intense blue with more boron doping. Boron has one electron less than carbon and therefore creates a hole in the band gap which can accept an electron from the valence band. Only a small energy (0.37 eV) [20] is needed for the electron to leave the valence band. This can be accomplished by red light which explains the blue color. The p-type semiconductor properties even occur at room temperature where the holes are thermally released.

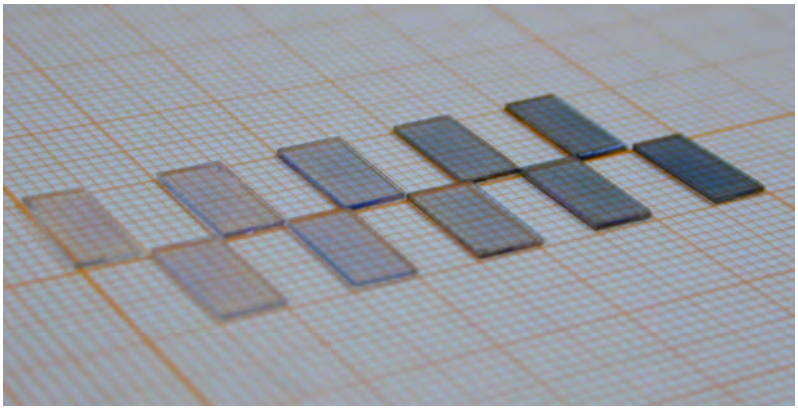

Figure 1.4: A series of medium to heavy boron-doped diamond films. The intensity increases as a function of boron doping.

Lots of diamonds contain sites with different types of impurities. This means that care has to be taken when classifying them.

1.3.2 Polycrystalline diamond

Polycrystalline diamonds are made of a large number of single crystal diamonds (grains), held together by thin layers of amorphous solid (grain boundaries). Grain boundaries influence the diamond properties significantly since they induce disorder. Electrons, phonons and photons are scattered more which results in a decrease in mobility, thermal conductivity and light emission (black diamond). Youngs modulus is also decreased by the amorphous fraction although high values are obtained up to small grain sizes [21]. Grain boundaries are known to contain sp^2 hybridised carbon which results in a decrease of the chemical inertness since sp^2 bonds are in most cases much more reactive than sp^3 bonds. A decreased concentration of sp^3 versus sp^2 bonds for films with smaller grains is characterized by Raman spectroscopy [21, 22, 23, 24, 25].

Microcrystalline diamond

When the average grain size of polycrystalline diamonds exceeds the value of 500 nm, polycrystalline diamonds are classified as microcrystalline diamonds (MCD) [26]. Layers of MCD are synthetically grown by CVD and during this process, the epitaxial orientation of the grains can be tuned [27]. FIG. 1.5 shows the SEM images of (111) and (100) oriented diamond films, obtained for different growth parameters.

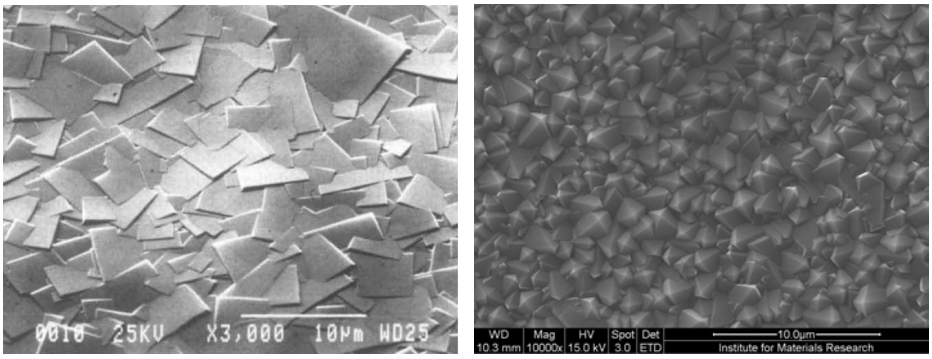

(a) (b)

Figure 1.5: The left panel (a) shows the epitaxially (100) oriented microcrystalline diamond film [27] and the right panel (b) shows the epitaxially (111) oriented microcrystalline diamond film grown at IMO.

Nanocrystalline diamond

When the average grain size of polycrystalline diamond is less than 500 nm, it falls into the class of nanocrystalline diamond (NCD). FIG. 1.6(a) is a SEM image of a roughly 180 nm thick NCD film, produced at IMO. The SEM image of the cross section is presented in FIG. 1.6(b) and was obtained by breaking the film together with the silicon substrate. Diamond films with the smallest grains are called ultrananocrystalline diamond (UNCD) films, which originate first in literature from the Argonne National Laboratory [28] and now also from other labs. FIG. 1.7 shows SEM images of a UNCD film, grown at IMO. In order to grow UNCD films, one has to drive a re-nucleation process during diamond growth. The result of re-nucleation is a decreased average grain size and an increased grain boundary density in the NCD films which can be observed by Raman spectroscopy. Re-nucleation is increased by an increased carbon concentration or by replacing partly hydrogen by argon in the plasma during the CVD procedure. This induces sites where new grains exist and start to grow, suppressing the evolution of the grains near this new growth site. When growing with low re-nucleation, the roughness of NCD films increases with their thickness and grain size. When growing with high re-nucleation, the roughness of the NCD films only depends on the grain size and stays almost the same for all thicknesses. This also means that films grown with a high re-nucleation rate will never reach grain sizes in the region of 500 nm to form MCD.

When the re-nucleation rate is even greater then the re-nucleation rate of UNCD during the CVD growth procedure, no crystalline sp^3 fractions can be detected. This material can't be classified as diamond but is classified as diamond-like carbon.

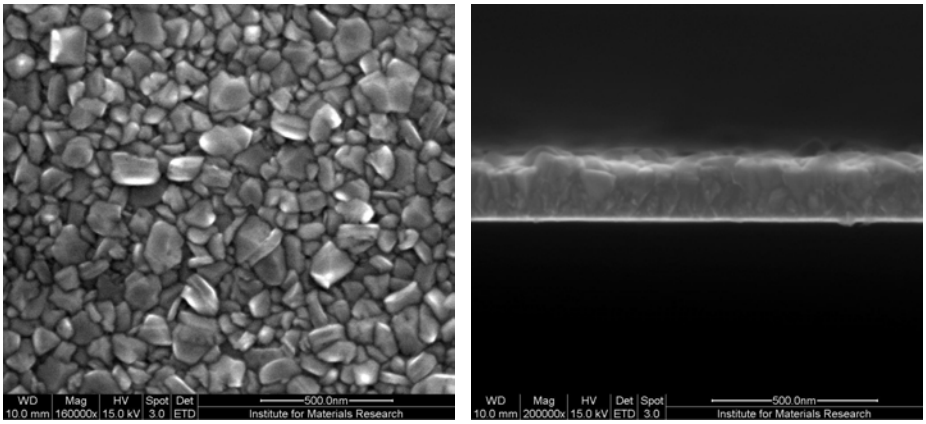

(a) (b)

Figure 1.6: The left graph (a) shows the SEM image of a roughly 180 nm NCD film, grown at IMO, with grains much less than 500 nm in size. The right graph (b) shows the SEM image of the cross section, obtained by breaking the sample.

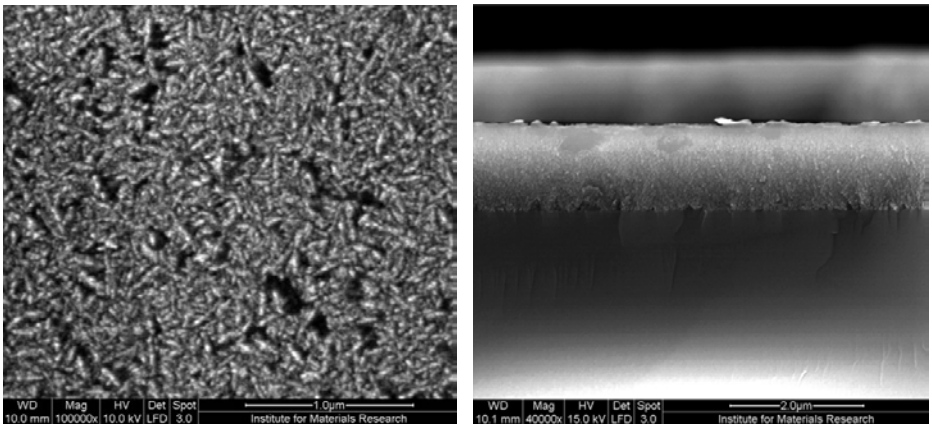

(a) (b)

Figure 1.7: The left graph (a) shows the SEM image of a roughly 1 μm thick UNCD film, grown at IMO. The right graph (b) shows the SEM image of the cross section, obtained by breaking the sample.

Chapter 2

Diamond growth

In this chapter, the growth of the previously classified types of diamonds is explained. The phase diagram of carbon, first published in 1955 by Bundy et al. [29] and updated through the years till 1996 [30], is used for this explanation. FIG. 2.1 shows the phase diagram of carbon, published by Bundy in 1980 [31], which contains all the necessary information for the scope of this work. One can derive from the phase diagram that diamond is metastable and graphite is stable under standard ambient conditions. A high activation energy between graphite and diamond prevents the graphitization of diamond at standard ambient conditions.

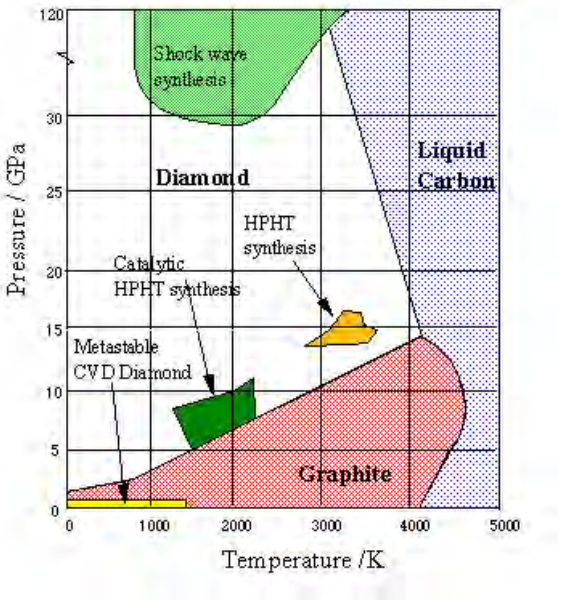

Figure 2.1: The phase diagram of carbon by Bundy, published in 1980 [31].

2.1 High-pressure high-temperature (HPHT)

The way of nature to produce diamond is by high-pressure and high-temperature (HPHT) synthesis under a pressure range of roughly 15 GPa and a temperature of roughly $3000 - 3500$ K. These conditions occur rarely since a deep-origin volcanic eruption at a depth of 150 km should occur. This is three times deeper than the magma source of most volcanoes. At this depth, a correct temperature and pressure can be contained for a long time, resulting in large single crystal diamonds. Through volcanic pipes, the diamond-bearing rock is transported by volcanic action to the surface or near surface [32].
The catalytic HPHT synthesis is done under a pressure range of roughly $5 - 11$ GPa and a temperature range of roughly $1200 - 2200$ K. This was first discovered in the fifties by F. P. Bundy, T. Hall, H. M. Strong and co-workers [29]. They dissolved graphite within molten nickel, cobalt or iron which made it possible to grow diamond. Initially, there was a presumption that the transition metals also act as a catalyst although none of this turned out to be true. The graphite was heated by passing an electric current though the graphite and the high pressure was created by the compression of the graphite, using an hydraulic press. The phase transition of graphite to diamond is accompanied by a volume decrease of 43%, posing problems to maintain a suitable pressure since a sudden pressure drop converts the diamond back to graphite [33]. In the last step, using boiling acids, the metals are dissolved, leaving behind diamond crystals with sizes ranging from nanometers to millimeters [34]. The first man-made diamonds were not of gem quality or size. This problem was solved by adding a seed from natural of HPHT diamond to the feed material.

2.2 Detonation

Detonation nanodiamonds (DND), often called ultra-dispersed diamonds (UDD), have a mean size quoted around 4 nm [35]. They are made from detonation synthesis with trinitrotoluene (TNT) and hexogen [36]. FIG. 2.1 shows the conditions where these nanodiamonds are stable and spontaneously formed. Due to the short duration of the shock wave (1 μs), the diamonds only have a diameter of several nanometers. This results in a specific surface area, greater than 400 m^2/g and with more than 15% of the carbon atoms located at the surface [37]. Initially, the particles form agglomerates but after hot nitric-acid treatment and bead-milling [38], they can be separated. Van der Waals forces still tend to form aggregates which can be separated in water or alcohol by ultrasonification [39]. FIG. 2.2 shows the XRD-spectrum of a UDD powder (IMO) together with a high resolution TEM-image of these UDD particles after separation [40]. The XRD spectrum confirms the high crystallinity of a UDD powder by showing the three most intense diffraction peaks. The TEM-image shows that the UDD-particles are heavily twinned and tend to be aggregated.

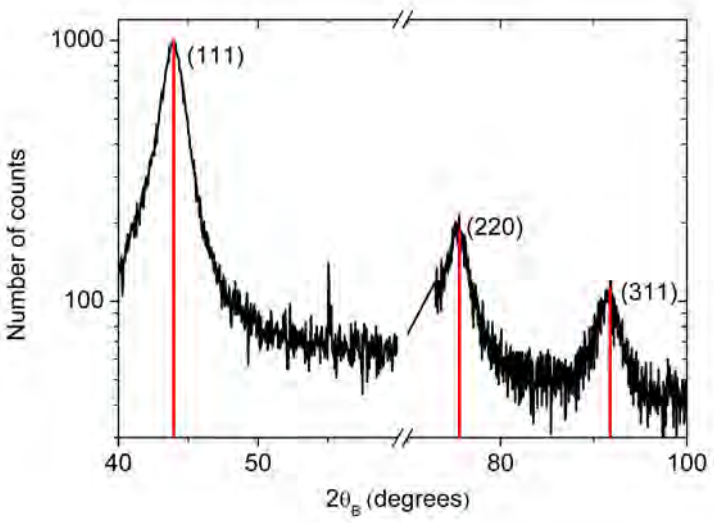

(a)

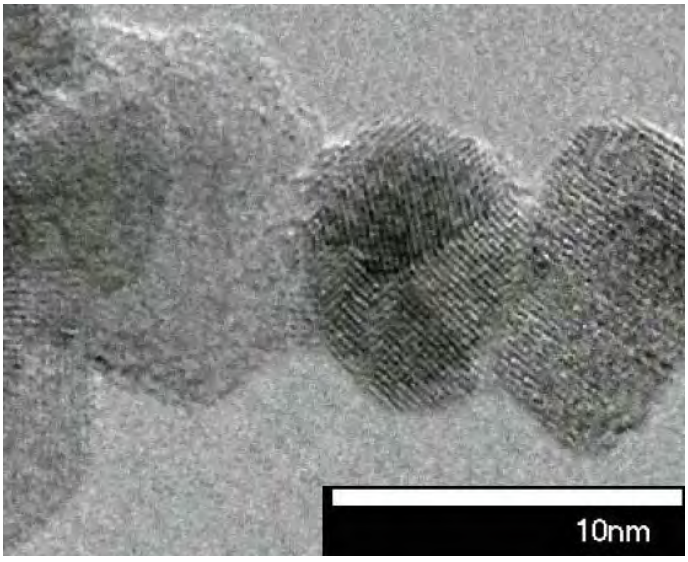

(b)

Figure 2.2: The left graph (a) shows the XRD spectrum of a detonation nanodiamond powder (IMO). The three most intense diffraction peaks of diamond (111), (220) and (311) are clearly observable. The right picture (b) shows a high resolution TEM-image of detonation nanodiamonds. Twinning and the tendency to form aggregates can be observed.

2.3 Chemical vapor deposition (CVD)

Due to the efforts made on the production of HPHT diamonds, other ways of producing diamond were strongly reduced. Still, some research groups tried to synthesize diamonds with other techniques. In 1962, the first successes were reported in the US by Eversole [41] and in 1968 in the former USSR by Derjaguin [42]. In the mid 1970s, Russian scientists finally established chemical vapor deposition as a useful way for producing diamond. This process was optimized with major Japanese research efforts at NIRIM which is now called the National Institute for Materials Science (NIMS).
The phase diagram of Bundy et al. (FIG. 2.1) shows a region where diamond is metastable at relatively low temperatures and pressures. In this region, there is a subregion wherein diamond can be produced with CVD under pressures going from 10 mTorr to 760 Torr (1 atm) [43] and for temperatures below 100°C [44] to more then 1000°C. Bachmann et al. made experiments in different systems under different conditions and found some universal parameters for diamond growth [45]. In 1993, the main principles of this empirical research was understood by a rigorous theoretical description of CVD diamond growth, published by James E. Butler and Richard L. Woodin [46]. Still, lots of efforts are made to understand the complex chemical mechanisms of diamond growth [47, 48, 49].
CVD can technologically be implemented using hot filaments, plasmas, combustion flames and other techniques to drive the process. Typically a small amount of methane or other sources of carbon and an abundance of hydrogen, sometimes mixed with halogens/oxygen, are used as reactants. The initiation of the gaseous chemistry is dominated by the dissociation of $1 - 40\%$ of the molecular hydrogen. The subsequent gaseous chemistry is than driven by reactions of atomic hydrogen with hydrocarbon species. A flow of molecular hydrogen and hydrocarbon radicals to the surface of an already existing diamond initiates the growth on the diamond surface. The diamond which is used as a growth platform is a natural diamond, a HPHT diamond or a detonation nanodiamond. In the next section, this is discussed in more detail. FIG. 2.3 is a schematic of the CVD process, presented by Butler et al. [46]. During the process, sp^2 and sp^3 bonds are formed on the substrate with hydrogen and adsorbed hydrocarbon species. Atomic hydrogen prevents the formation of sp^2 and sp^3 bonds with hydrogen. Therefore, atomic hydrogen prevents the incorporation of defects. It also lowers the growth rate of the adsorbed hydrocarbon species. This implies that high quality diamond is grown at lower rates. Diamond growth is also limited by a low hydrogen abstraction at low temperatures and by thermal desorption of adsorbates at higher temperatures. Taking into account stereochemistry, different growth rates for different crystal orientations and twinning are theoretically approachable [49].

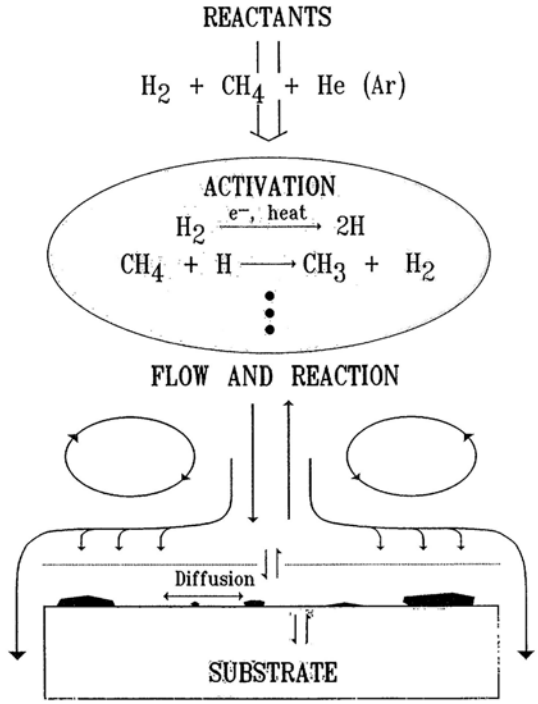

Figure 2.3: A schematic showing the principal elements in the complex diamond CVD process: flow of reactants into the reactor, activation of the reactants by thermal and plasma processes, reaction and transport of the species to the growing surface, and surface chemical processes depositing diamond and other forms of carbon [46].

2.3.1 Substrate pretreatment

When an untreated silicon wafer is introduced in a CVD reactor and a growth run is done, nucleation densities around $10^4 - 10^5$ cm^{-2} occur [50]. With these nucleation densities, polycrystalline films have to grow several micrometers in thickness before being completely coalesced. The only ways for enhancing the nucleation density is using iridium or doing a surface pre-treatment. On single crystal iridium, single crystalline diamond can be grown over large areas [51]. Some surface pre-treatment techniques reach nucleation densities of more than 10^{11} cm^{-2}. This allows the growth of all the polycrystalline diamond films, discussed in section 1.3.2.

Mechanical abrasion techniques

Scratching of a substrate with diamond powder is known to increase the nucleation density [52]. The main mechanism behind this is the embedding of small residual diamond particles in the substrate. Scratches and defects, induced by this procedure, also increase the surface to volume fraction leading to enhanced carbon super-

saturation as well as a lower total free energy of the diamond nucleus due to reduced contact with the substrate surface [53]. Smaller diamond particles tend to result in higher nucleation densities and increase the uniformity [54], presumably due to the large surface to volume fraction of the finer scratches and the increase of residual diamond.

Ultrasonic particle treatment

Ultrasonic treatment of substrates, immersed into a slurry of micron sized diamond particles, enhances the nucleation densities to 10^{10} cm^{-2} [54] and in extreme cases to 10^{11} cm^{-2} [55]. The nucleation mechanism strongly resembles that of mechanical abrasion with the advantage of better uniformity and reduced scratching artifacts. HRTEM investigations show that homoepitaxial growth on the remaining diamond embedded in the diamond substrate is the predominant nucleation mechanism. The nucleation density increases with increasing grain size since small grains have insufficient momentum to penetrate into the substrate [54]. A combination of two particle sizes, $< 0.25\ \mu$m and $> 2\ \mu$m, increases the nucleation density since the bigger particles (diamond or not) drive the smaller diamond particles into the substrate. This is the so-called "hammering" approach [56]. Three dimensional structures can be made by using this technique but large sized diamonds still remain and increase high local disturbances.

Bias enhanced nucleation

Bias enhanced nucleation (BEN) is an in-situ nucleation technique which uses a negatively biased conductive substrate by around $100 - 250$ V DC with respect to the grounded reaction chamber or a second internal electrode. This process is carried out under rather methane rich conditions, compared to high quality diamond growth [57]. It is generally accepted that the mechanism of BEN is based on the sub-plantation model [58, 59] where incident CH_x^+ ions have an optimum energy (≈ 80 eV) to sub-plant them. Still, the correct mechanism of diamond growth is under discussion [58, 59]. When the nucleation is done, diamond layers can be grown by switching over to high quality diamond growth conditions. The only disadvantage of this technique is the limitation to conductive substrates.

Nano-particle seeding

In section 2.2, we already discussed the separation of detonation nanodiamond agglomerates. When these nanodiamonds are immersed in water or alcohol, they form a stable colloidal suspension due to charges on their surface, repelling each other [38, 39]. In FIG. 2.4(a) one can see the results of a DLS measurement which proves that almost all particles are no more aggregated [39]. When performing ζ-potential measurements, one can measure the stability of the suspension. This potential should be higher than 25 mV or lower than -25 mV to form a stable suspension. For untreated detonation diamonds, fully dispersed in water with a high pH, values up to -50 mV can be reached. At a pH of 7, the particles have a ζ-potential between -25 and -30 mV [60]. These particles tend to stick to surfaces which is a property

one uses in the nano-particle seeding procedure. In this procedure, a cleaned substrate on which the nanodiamonds stick well, is immersed in a diamond suspension. The particles attach to the substrate with weak van der Waals forces and when the substrate is removed from the diamond suspension, it is flushed with water on a spin coater and dried during spinning. Now, a layer of ≈ 5 nm particles is formed on the surface of the substrate which is shown in FIG. 2.4(b) by AFM measurements [39]. When applying this technique, the substrate is not damaged, the as-grown diamond layer is very homogeneous, non-conducting substrates can be used and all types of polycrystalline diamond can be grown. The only problem which rises is the growth of films thicker than 200 nm on quartz substrates. This is a problem which still needs to be tackled.

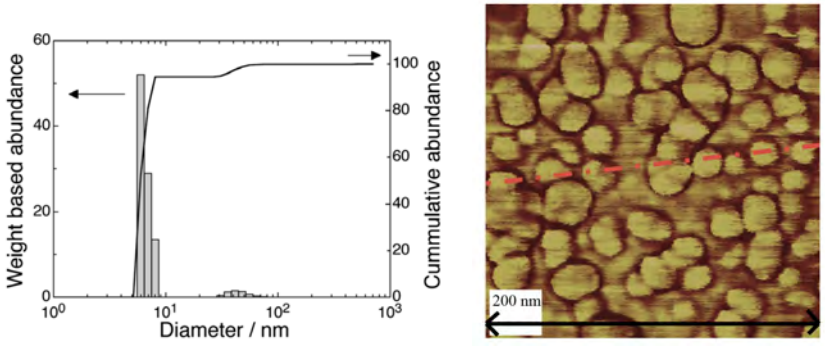

(a) (b)

Figure 2.4: The first panel (a) shows the results of a DLS experiment performed on a detonation diamond suspension of ≈ 5 nm in water. There are almost no aggregates detectable. The second panel (b) shows the AFM image of a nanodiamond seeded (nucleated) substrate surface [39].

Part II

Theory, experiments and results

Chapter 3

The surface of NCD

This chapter shows the results of contact angle measurements performed on NCD surfaces and surface energies calculated from those measurements. The first section gives a theoretical introduction, necessary to interpret and perform contact angle measurements. The second section presents the results of a small cleaning study concerning the surface of hydrogen terminated boron-doped nanocrystalline diamond (B:NCD:H)). In the last section, a study to determine the surface energy of NCD:H is presented. The latter study was mainly performed by Sien Drijkoningen as a part of her bachelor thesis, under my supervision.

3.1 Contact angle measurements

3.1.1 Law of Young-Dupré

When distorting a liquid to increase its surface area by an amount dA, the work required is proportional to the numbers of molecules that must be brought up to the surface, i.e., to dA; one can write:

$$\delta W = \gamma dA \tag{3.1}$$

where γ is the surface (or interfacial) energy which is expressed in mN/m. Young derived an equation which makes a relation between a contact angle of a droplet on a surface and the accompanying surface energy:

$$\gamma_{SV} = \gamma_{SL} + \gamma_{LV} cos\theta \tag{3.2}$$

where the three coefficients γ are the surface energies at the solid/vapor, solid/liquid and liquid/vapor interfaces, respectively [61]. In FIG. 3.1, these surface energies and the contact angle of a sessile water droplet on a NCD:H surface are illustrated. The lengths of the vectors do not correspond to the real values of the surface energies. Dupré defined the work of adhesion, W_a, as [62]:

$$\gamma_{SV} = \gamma_{SL} + \gamma_{LV} - W_a \tag{3.3}$$

which results in the law of Young-Dupré:

$$W_a = \gamma_{LV}(1 + cos\theta). \tag{3.4}$$

In order to calculate γ_{SV}, when knowing the value of γ_{LV} and missing the value of γ_{SL}, a more subtle method, like the 'OWRK' method is required.

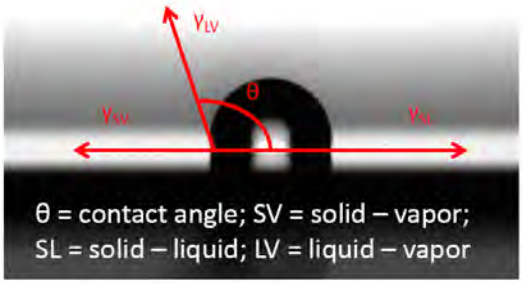

Figure 3.1: A sessile water droplet on a NCD:H surface with the surface energies and the contact angle presented. The lengths of the vectors do not correspond to the real values of the surface energies.

3.1.2 The 'OWRK' method

Berthelot described the constants between like, A_{aa}, and unlike, A_{ab}, molecules in the following relationship [63]:

$$\frac{A_{ab}}{(A_{aa}A_{bb})^{1/2}} = 1. \tag{3.5}$$

Good and Girifalco defined a similar ratio, involving the energies of adhesion and cohesion for two phases. But for generality, they set the ratio equal to θ instead of one and afterwards they tried to estimate the value of θ [64]:

$$\frac{-\Delta F^a_{ab}}{(\Delta F^a_c \Delta F^b_c)^{1/2}} = \theta. \tag{3.6}$$

If ΔF^a_{ab} is the free energy of adhesion for the interface between phases A and B, than $\Delta F^a_{ab} = \gamma_{ab} - \gamma_a - \gamma_b$ with γ_{ab} representing the interfacial energy, γ_a the free energy of phase A and γ_b the free energy of phase B. And if ΔF^n_c is the free energy of cohesion for phase N, than $\Delta F^n_c = 2\gamma_n$ with γ_n the free energy for phase N. These equations can be solved for γ_{ab}:

$$\frac{-(\gamma_{ab} - \gamma_a - \gamma_b)}{2\sqrt{\gamma_a \gamma_b}} = \theta \tag{3.7}$$

$$\gamma_{ab} - \gamma_a - \gamma_b = -2\theta\sqrt{\gamma_a \gamma_b} \tag{3.8}$$

$$\gamma_{ab} = \gamma_a + \gamma_b - 2\theta\sqrt{\gamma_a \gamma_b} \tag{3.9}$$

In analogy with the Dupré EQ. 3.3, Good and Girifalco [64] described the work, W_a, by using the geometric mean of the surface energies of the individual phases:

$$W_a = 2\sqrt{\gamma_a \gamma_b} \tag{3.10}$$

where θ is a function that could only be determined empirically. EQ. 3.10 can be used in the Dupré equation (3.3) so that the next relation exists:

$$\gamma_{SV} = \gamma_{SL} + \gamma_{LV} - 2\theta\sqrt{\gamma_a \gamma_b} \tag{3.11}$$

Owens, Wendt, Rabel and Kaelble ('OWRK') [65, 66] stated that the surface energy can be split in a polar and a disperse fraction:

$$\gamma = \gamma^D + \gamma^P \tag{3.12}$$

The polar fraction is the part of the surface energy that results from interactions of polar groups, e.g. hydrogen bonding, dipole-dipole interaction, while the disperse surface energy results from nonpolar interactions of molecules, e.g. induced dipole-induced dipole interaction. According to this model, the parameter θ represents the interactions by assuming that only interactions of the same type can occur between different phases. This means that polar liquids will only interact with the polar parts of the substrate. Owens, Wendt, Rabel en Kaelble used EQ. 3.11 to get

$$\gamma_{SV} = \gamma_{SL} + \gamma_{LV} - 2\left(\sqrt{\gamma^D_{SV}\gamma^D_{LV}} + \sqrt{\gamma^P_{SV}\gamma^P_{LV}}\right) \tag{3.13}$$

and combined this with Young's equation (3.2):

$$\gamma_{SV} - \gamma_{LV} cos\theta = \gamma_{SL} + \gamma_{LV} - 2\left(\sqrt{\gamma^D_{SV}\gamma^D_{LV}} + \sqrt{\gamma^P_{SV}\gamma^P_{LV}}\right) \tag{3.14}$$

$$\frac{\gamma_{LV}(cos\theta + 1)}{2} = \left(\sqrt{\gamma^D_{SV}\gamma^D_{LV}} + \sqrt{\gamma^P_{SV}\gamma^P_{LV}}\right) \tag{3.15}$$

$$\frac{\gamma_{LV}(cos\theta + 1)}{2\sqrt{\gamma^D_{LV}}} = \sqrt{\gamma^P_{SV}}\sqrt{\frac{\gamma^P_{LV}}{\gamma^D_{LV}}} + \sqrt{\gamma^D_{SV}} \tag{3.16}$$

This equation is in the form of the equation of a straight line, $y = ax + b$ with:

$$y = \frac{\gamma_{LV}(cos\theta + 1)}{2\sqrt{\gamma^D_{LV}}} \tag{3.17}$$

$$a = \sqrt{\gamma^P_{SV}} \tag{3.18}$$

$$x = \sqrt{\frac{\gamma^P_{LV}}{\gamma^D_{LV}}} \tag{3.19}$$

$$b = \sqrt{\gamma^D_{SV}} \tag{3.20}$$

which is graphicalliy illustrated on FIG. 3.2. By measuring the contact angles of different liquids, with known values for γ_{LV}, γ^D_{LV} and γ^P_{LV} the surface energy solid-vapor, γ_{SV} can be determined relatively easily according to Owens, Wendt, Rabel and

Kaelble's ('OWRK') method. The polar fraction γ_{SV}^{P} can be obtained from the slope, while the disperse fraction γ_{SV}^{D} is obtained from the intercept. Based on EQ. 3.12, one can put forward that the surface energy solid-vapor is the sum of both fractions. Once the surface energy solid-vapor is known, the surface energy solid-liquid can be determined by performing contact angle measurements on the NCD:H surface with liquids with a known surface energy liquid-vapor and using the Young equation.

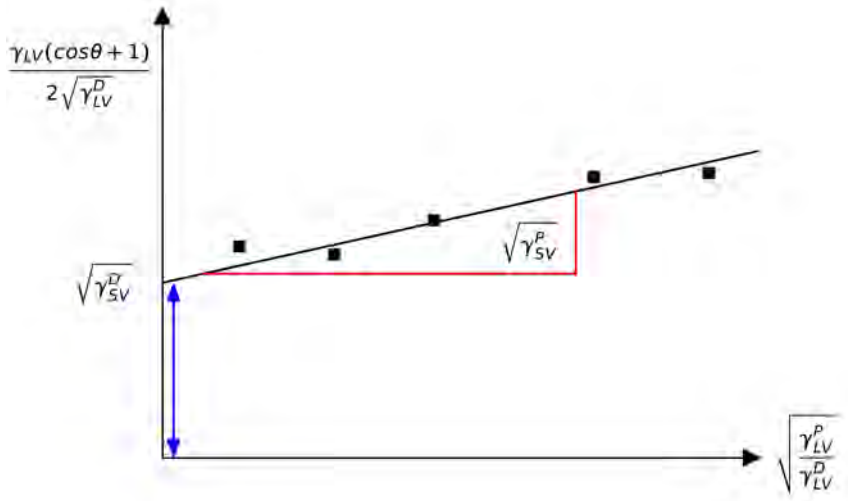

Figure 3.2: An illustration of the use of the 'OWRK' method in determining the surface energy.

3.2 Oxidation of B:NCD:H

Cleaning of diamond surfaces is commonly performed in order to deposit good ohmic contacts [67] and before performing other surface related treatments [68]. Bad contacts induce more noise which makes the signal-to-noise ratio (S/N) decrease. This is shown in chapter 5.2 where the S/N is measured for good and bad contacts. In this section, B:NCD films which are cleaned with a strong oxidizing mixture for several hours are discussed. The surface characterization is done by contact angle measurements in order to monitor the oxygen groups on the surface which lower the contact angle drastically. It is observed that increasing the temperature of a very strong oxidizing mixture too much leads to complete film detachment from a fused silica substrate. Therefore, lower temperatures and a less strong oxidizing mixture were used to keep the diamond films intact.

3.2.1 Experimental

In this work, microwave plasma enhanced (MWPE) CVD is used to grow diamond layers. Two commercial ASTeX reactors of the 6500 type are used for depositing nanocrystalline diamond layers. ASTeX 2 is used for heavily boron-doped diamond and ASTeX 3 is used for non-doped diamond. In FIG. 3.3 one can see the outside (a) and the inside (b) of the AXTeX 2 reactor. In this reactor, microwaves are guided from under the reaction chamber into the reactor chamber. In FIG 3.3(b), a molybdenum substrate holder on which the microwaves are reflected by the walls of the reaction chamber is shown. The microwave source of ASTeX 2 delivers up to 8 kW of microwave power with a minimum of 2.5 kW at a constant frequency of 2.45 GHz. The substrate holder is placed on a water cooled copper stage stage which prevents the substrate heating up too much by the plasma. The reactant gases, introduced at the top of the reactor at a total flow of 500 sccm are hydrogen (H_2), methane (CH_4) and TMB ($B(CH_3)_3$). This flow is regulated by gas flow meters and a rotary pump. The base pressure is $\approx 2 \times 10^{-9}$ bar and can be reached with a turbo pump after closing

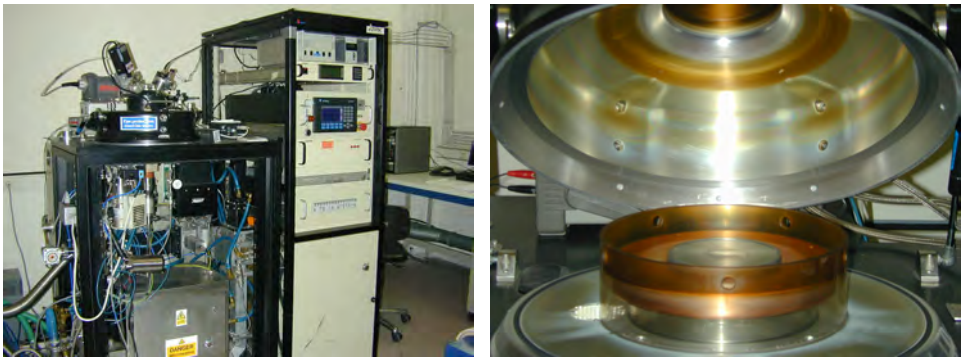

(a) (b)

Figure 3.3: The first panel (a) shows an ASTeX 6500 system (ASTeX 2) and the second panel (b) shows the inside of the reaction chamber.

the reaction chamber.
A Williamson Pro 90 dual wavelength pyrometer is used to monitor the substrate temperature. The pyrometer measures the intensity of electromagnetic waves with wavelengths close to 0.2 mm (far IR) and calculates the temperature of the diamond. During this calculation, the assumption is made that the ratio between the emissivities remains constant. Care has to be taken since this pyrometer interferes with the diamond layer as its thickness evolves. Every ≈ 250 nm there is a minimum or a maximum in the temperature readings which also serves as a thickness monitor during the growth of a diamond layer [69].
The conditions which are used to grow diamond in the ASTeX reactors are $20-50$ torr of gas pressure and $3000-4500$ Watts of microwave power. The temperature can additionally be controlled by a small hole under a hollow substrate holder which is called the plenum. The plenum creates a vacuum which prevents heat transfer from the substrate holder to the copper stage, enabling temperature adjustments.
Four boron-doped nanocrystalline diamond (B:NCD) samples were grown, all with the same temperature (700°C), substrate (fused silica), microwave power (3500 W), B/C-ratio in the gas phase of the reaction chamber (5000 ppm) but with a different C/H-ratio in the gas phase (1%, 2%, 3% and 4%). Cooling down till 400°C was done in a hydrogen plasma in order to generate a B:NCD:H surface. The oxidizing mixture consists of 100 ml of 95% sulphuric acid (H_2SO_4) with 100 ml water and 50 g potassium nitrate (KNO_3). During the oxidation process, the samples and the mixture were kept at 95°C for a total time of 17 hours. At the beginning ($t = 0$ hours), at $t = 3$ hours and in the end ($t = 17$ hours) the contact angles of the four samples were measured after rinsing with DI water. The contact angle measurements are performed with an OCA 15 plus. The shape of the DI water droplet is approached using the 'conic fit' and the contact angle of the droplet is determined with the same model, after manually setting the baseline. The droplet size used in every experiment is 1.0 μl and is dispensed at 0.4 μl/s. The contact angle is independent of the size of the droplet up to 10.0 μl [70], but when the droplet gets bigger, gravity comes into play. Gravitational forces will then start to overpower the cohesive forces in the liquid and because of this phenomenon the measured contact angle will differ from the correct contact angle. Besides gravitational forces, other forces can be present as well. Interactions between the syringe and the liquid are minimized by coating the syringe with vacuum grease, so that the droplet can be deposited neatly without crawling up the syringe. All contact angles are measured as a function of time to eliminate settling and drying effects. When the droplet is settling, the contact angle is too high and when the droplet is drying, the contact angle diminishes. Therefore, an extrapolation of the drying curve to t = 0 is done to obtain the correct contact angle. This is presented in FIG. 3.4 for an intrinsic NCD:H sample right after hydrogenation and 24 hours after hydrogenation. With the deposition of a droplet on a solid surface, a 'receded' (static) contact angle is measured. In FIG. 3.4, a decrease in the contact angle is observed after 24 hours which is attributed to oxidation and contamination of the surface.

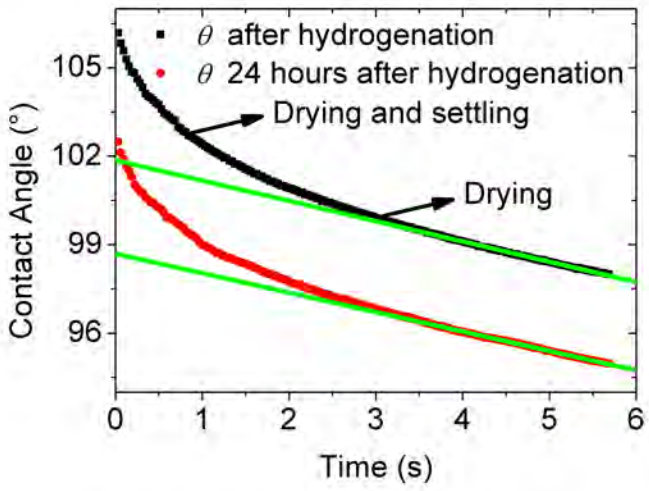

Figure 3.4: Determination of the contact angle as a function of time. The decrease in the contact angle is observed after 24 hours which is attributed to oxidation and contamination of the surface.

3.2.2 Results and conclusions

FIG. 3.5 shows the contact angles before oxidation, after 3 hours and at 17 hours for the sample grown with 1% C/H-ratio. The contact angle at the beginning is rather low for a NCD:H sample since it took some days after hydrogenation before this experiment was conducted. The surface can be partially oxidized (see next section) and contaminated (dust). The contact angle decreases in time due to the oxygen groups which are formed on the NCD surface. They interact better with water though dipole-dipole interactions which makes the water spread more easily. All samples show this behavior and a summary is given in FIG. 3.6. It is clear that the decrease of the contact angle is faster at the beginning of the process. This is explicable since the process is a chemical reaction. When there are no oxygen groups on the surface, the reaction rate is high and when the surface is terminated with oxygen groups, a dynamic equilibrium exists where no additional oxygen groups are added to the surface. This means that the reaction rate decreases and after a certain time is zero. Further experiments are not conducted since it exceeds the objectives of this work. Still, a proof of principle is presented which shows how contact angle measurements can be used to investigate the interaction of chemicals with NCD surfaces. The presented procedure (17 hours) is now used at IMO to oxidize and clean B:NCD layers without having delamination.

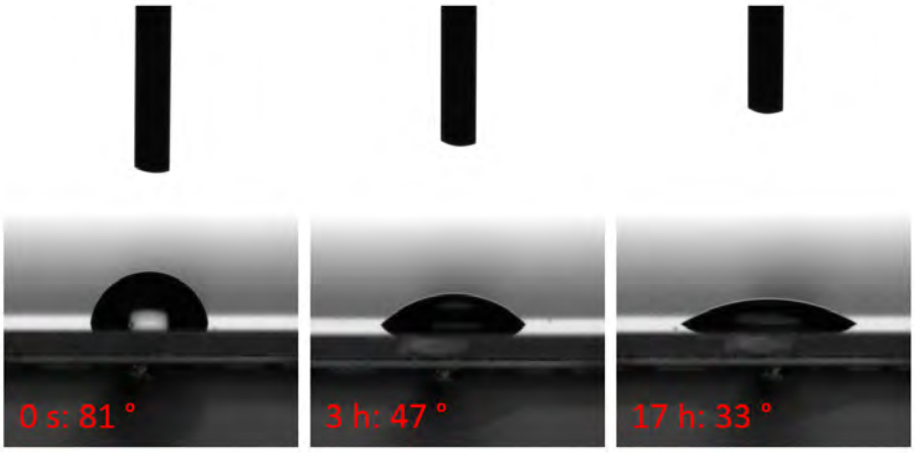

Figure 3.5: Pictures of a water droplet on the NCD surface of the 1% sample, before, during and after oxidation.

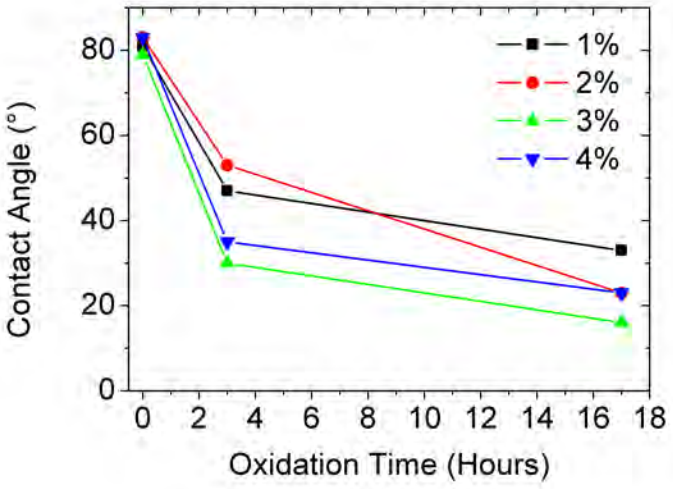

Figure 3.6: A summary of the contact angle values for the four samples, before, during and after oxidation.

3.3 The surface energy of NCD:H

3.3.1 Introduction

Nanocrystalline diamond is a versatile material that is currently being put forward as a material of choice for a variety of applications that make use of its surface properties. In this section, a determination of the surface energy for hydrogen terminated NCD (NCD:H) grown with microwave plasma enhanced chemical vapour deposition in the ASTeX 3 reactor is presented. Five identical NCD:H samples of ≈ 150 nm thick are deposited on silicon substrates and examined with XPS to determine the surface groups and possible surface contaminations. In order to evaluate the surface energy, contact angle measurements are performed using the sessile drop method in combination with data analysis based on the 'OWRK' method. Four possible experiments to evaluate the surface energy of NCD:H are discussed:

- Experiment 1: water, ethylene glycol and diiodomethane
  → ($\gamma = 34 \pm 5$ mN/m)
- Experiment 2: multiple alcohol/water solutions
  → values used from the article of Hong and Chen ($\gamma = 30 \pm 10$ mN/m) [71]
- Experiment 3: multiple alcohol/water solutions
  → calibrated with a variety of polymers ($\gamma = 16 \pm 2$ mN/m)
- Experiment 4: multiple alcohol/water solutions
  → calibrated with a variety of calibrated polymers ($\gamma = 16 \pm 4$ mN/m)

Experiment 1 is the standard way to determine surface energies and this method leads to no significant polar interactions on the surface after data analysis, which is expected from NCD:H, which is hydrophobic in nature [72]. However, the last two methods do show polar interactions on the surface to a certain extent. A possible explanation for this phenomenon is the presence of a higher adhesion force between alcohol (ethanol) and the NCD:H surface than between water and the NCD:H film. This would mean that the last two experiments lead to erroneous data because of the presence of a thin layer of alcohol on NCD:H, effectively leading to a water on alcohol system instead of the envisaged alcohol/water mixture on an NCD:H surface. Therefore, Experiment 1 which is performed with pure liquids seems to be the most reliable to determine the surface energy of NCD:H.

3.3.2 Experimental

Five intrinsic NCD samples of 1 cm by 1 cm are grown on silicon substrates in one growth run using ASTeX 3. Growth was performed during 23 minutes with a 2% C/H-ratio, a pressure of 30 Torr and a temperature of 815°C, as monitored with a dual wavelength pyrometer. When a thickness of 150 nm was reached, growth was stopped. FIG. 3.7(a) shows a SEM image of the pinhole free NCD:H film. All five films are investigated by SEM and none of them contained pinholes. Hydrogenation takes place right before the contact angle measurement to avoid surface contamination and oxidation under ambient conditions. This is performed in ASTeX 3 under the same conditions as growth but without methane in the reaction chamber. An X-ray photoelectron spectroscopy (XPS) spectrum, shown in FIG. 3.7(b), shows very small signals of fluorine and oxygen (≈ 1%) beside the significant carbon peak, demonstrating the very low level of contaminations. Although these are very small, they have to be taken into account in further work.

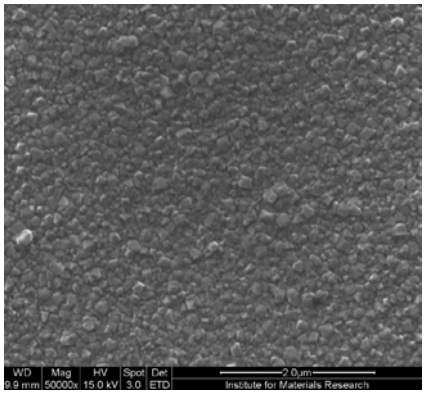

(a)

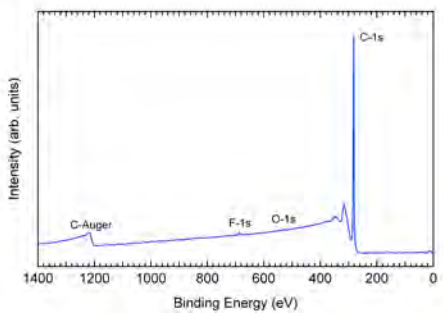

(b)

Figure 3.7: On panel (a), a SEM image of a pinhole free NCD:H film. On panel (b), the XPS spectrum of one NCD:H sample with a small oxygen and fluorine signal next to a clear carbon peak.

The surface energy of the NCD:H layers is calculated using the 'OWRK' method. The easiest way of deriving the surface energy of NCD:H, is using pure liquids with known polar and disperse contributions to the total surface energy. Such an experiment, performed on NCD:H is done with water, ethylene glycol and diiodomethane and is presented in Experiment 1. A second way of determining the surface energy of NCD:H, is using mixtures with unknown polar and disperse parts. These mixtures can be calibrated on surfaces on which the polar and disperse parts are known. In Experiment 2, calibrated surface energy values of alcohol/water mixtures, determined by Hong and Chen [71] are used. The contact angle experiments are then done on the NCD:H surface with the same alcohol/water mixtures as Hong and Chen used. In Experiment 3, the alcohol/water mixtures were calibrated in house on a variety of polymers; i.e. polyamide (PA), polycarbonate (PC), polyethylene (PE), polymethylmethacrylate (PMMA), polypropylene (PP), polystyrene (PS), polytetrafluoroethylene (PTFE), polyvinyl chloride (PVC); since Hong and Chen only used one polymer, PTFE, to calibrate the mixtures, leaving room for interpretation. In the last experiment, one further step was taken, first calibrating the polymers on which then alcohol/water mixtures were used, since the possibility always exist that the used polymers contain some plasticizers, e.g. phthalates, altering surface energy values found in literature.

3.3.3 Results

Experiment 1: Pure liquids

The first determination of the surface energy is a direct application of the 'OWRK' method, only with contact angle measurements of pure liquids on NCD:H. For this purpose ethylene glycol, diiodomethane and water are used to measure the contact angles, because values of their surface energy are reliably known from literature. The values used, were those determined by Ström and coworkers [73]. The 'OWRK' plot which is presented in FIG. 3.8 allows us to determine the surface energy of NCD:H. By using EQ. 3.17-3.20, the polar part is determined by the the slope, while the disperse part can be derived from the intercept of a least squares regression line:

$$\gamma_{SV}^{P} = 0.1 \pm 0.3 \text{ mN/m} \tag{3.21}$$

$$\gamma_{SV}^{D} = 34 \pm 5 \text{ mN/m}. \tag{3.22}$$

The total surface energy:

$$\gamma_{SV} = 34 \pm 5 \text{ mN/m} \tag{3.23}$$

consists only of the disperse part which is expected when a surface is hydrogen terminated. The the error on the latter values is determined from the least squares regression. The main error source seems to be the accuracy of the contact angle value and not the precision of the contact angle value since for every measurement, the contact angle values of five different samples only differed by maximum one degree which is negligible.

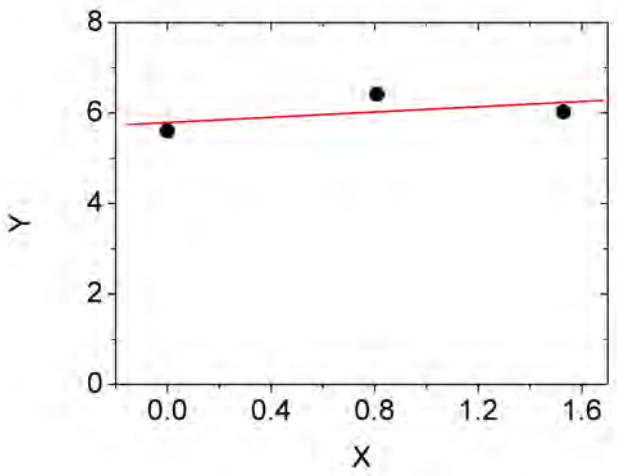

Figure 3.8: The 'OWRK' plot of the contact angle measurements on NCD:H with pure liquids. Y refers to EQ. 3.17 and X refers to EQ. 3.19.

Experiment 2: Multiple alcohol/water solutions → values from Hong and Chen

Pure liquids are mainly used to perform contact angle measurements since mixtures behave in a more complex way which is not incorporated in the 'OWRK' or any other method. Still, Hong and Chen published surface energy values of DLC which are measured with alcohol/water mixtures and calibrated on PTFE [71]. By calibrating, they obtained the polar and the disperse surface energies of different alcohol/water mixtures. In this work, the same alcohol/water mixtures in the contact angle experiments together with the calibrated values for the polar and disperse surface energies of the alcohol/water mixtures, obtained by Hong and Chen. This way, the surface energy of NCD:H using the 'OWRK' method was obtained. In TAB. 3.1 one can see the values of the contact angles measured on the NCD:H samples. The corresponding surface energies, determined by Hong and Chen are also shown in this table. By increasing the amount of alcohol in the mixture, the contact angles decrease and the surface energy of the mixtures also decreases. Especially the polar part of the surface energy decreases drastically with increasing the alcohol concentration. The 'OWRK' plot which is presented in FIG. 3.9 allows us to determine the surface energy of NCD:H with values obtained from Hong and Chen. Again, by using EQ. 3.17-3.20, the polar part is determined by the the slope, while the disperse part can be derived from the intercept:

$$\gamma_{SV}^{P} = 1 \pm 2 \text{ mN/m} \tag{3.24}$$

$$\gamma_{SV}^{D} = 30 \pm 10 \text{ mN/m}. \tag{3.25}$$

The total surface energy:

$$\gamma_{SV} = 30 \pm 10 \text{ mN/m} \tag{3.26}$$

consists only of the disperse part although the error is much larger than in the previous experiment.

Table 3.1: The measured contact angles of the alcohol/water droplets on the NCD:H surface and the corresponding surface energy values of the alcohol/water mixtures determined by Hong and Chen.

alcohol/water (Volume%)	θ (degrees)	γ_{LV}^{D} (mN/m)	γ_{LV}^{P} (mN/m)	γ_{LV} (mN/m)
0	103.1	11.9	60.3	72.2
10	96.6	19.8	31.4	51.2
30	66.8	12.7	23.4	36.1
50	57	13.4	16.6	30
60	30.4	13.5	14.5	28
70	22.6	16.2	11	27.2

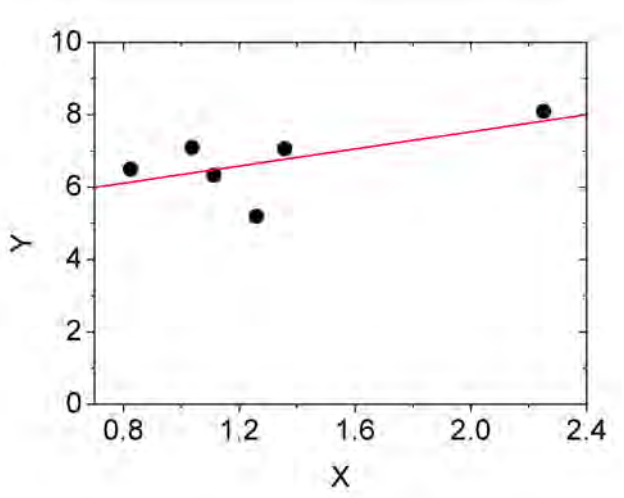

Figure 3.9: The 'OWRK' plot of the contact angle measurements on NCD:H with alcohol/water mixtures and their surface energy values, obtained from Hong and Chen. Y refers to EQ. 3.17 and X refers to EQ. 3.19.

Experiment 3: Multiple alcohol/water solutions → calibrated with a variety of polymers

Since the surface energies of the alcohol/water mixtures in Experiment 2 are only calibrated on one polymer, the decision was taken to calibrate the mixtures on a set of polymers (PA, PC, PE, PMMA, PP, PS, PTFE, PVC). In order to do so, one needs the total surface energy of the mixtures to derive the polar and disperse parts. These values are derived from the work of Vazquez et al. [74] and listed in TAB. 3.2. When using EQ. 3.15, one can calculate the disperse part of the surface energy and by using EQ. 3.12 it is easy to derive the polar part of the surface energy. With all surface energies for the mixtures known, the 'OWRK' method can, without further adaptation, be applied. The 'OWRK' plot which is presented in FIG. 3.10 allows us to determine the surface energy of NCD:H with alcohol/water mixtures calibrated on a variety of polymers. Like in the previous two experiments, EQ. 3.17-3.20 are used to calculate the polar and the disperse parts of the surface energy:

$$\gamma_{SV}^{P} = 10.8 \pm 0.7 \text{ mN/m} \tag{3.27}$$

$$\gamma_{SV}^{D} = 5 \pm 2 \text{ mN/m}. \tag{3.28}$$

In contrast with previous experiments the total surface energy:

$$\gamma_{SV} = 16 \pm 2 \text{ mN/m} \tag{3.29}$$

consists mainly of a polar fraction.

Table 3.2: The surface energies of the alcohol/water mixtures as a function of volume parts are presented, based on values obtained by Vazquez et al. [74].

alcohol/water (Volume%)	γ_{LV} (mN/m)
0	72
10	52
20	41
30	35
40	33
50	31

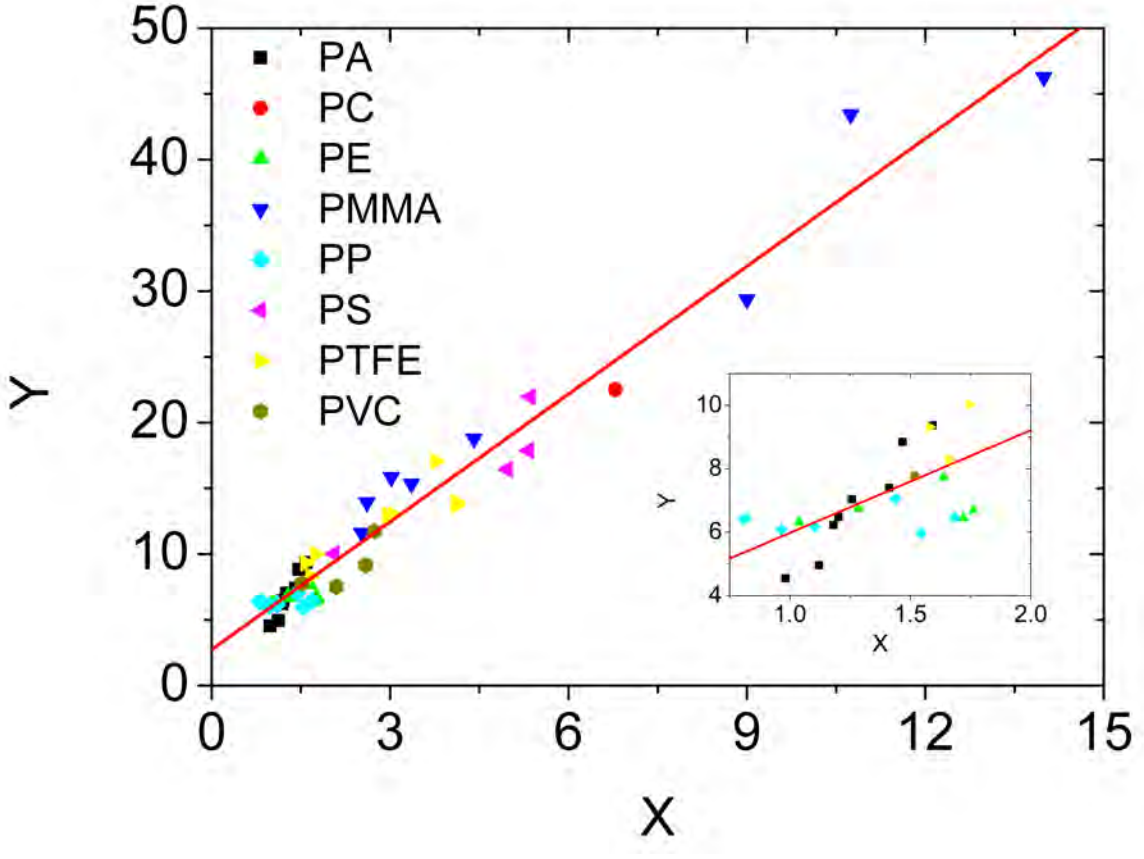

Figure 3.10: The 'OWRK' plot of the contact angle measurements on NCD:H with alcohol/water mixtures and their surface energy values, obtained from a variety of polymers. Y refers to EQ. 3.17 and X refers to EQ. 3.19.

Experiment 4: Multiple alcohol/water solutions → calibrated with a variety of calibrated polymers

The difference with the previous approach is that now the values of the used polymers are not taken for granted but are calculated with the known values for ethylene glycol, diiodomethane and water since the surface tension of these liquids are considered to be more reliable than those of the polymers. The same procedure as in Experiment 1 is followed to determine the polar and the disperse parts of the surface energies of the polymers. TAB. 3.3 shows the values obtained from literature together with the values obtained by the calibration. A 'OWRK' plot of the contact angle measurements on NCD:H with alcohol/water mixtures and their surface energy values, obtained from the variety of calibrated polymers, is presented in FIG. 3.11. Again, EQ. 3.17-3.20 are used to calculate the polar and the disperse parts of the surface energy:

$$\gamma_{SV}^{P} = 7 \pm 2 \text{ mN/m} \tag{3.30}$$

$$\gamma_{SV}^{D} = 9 \pm 4 \text{ mN/m}. \tag{3.31}$$

Like in the previous experiment the total surface energy:

$$\gamma_{SV} = 16 \pm 4 \text{ mN/m} \tag{3.32}$$

contains not only a disperse fraction but also a large polar fraction.

Table 3.3: The values of the surface energies of a variety of polymers found in literature and calibrated by pure liquids. For PP, no reliable contact angles could be measured. The dimensions of the values are in mN/m.

Polymer	$\gamma_{Lit.}^{D}$	$\gamma_{Lit.}^{P}$	$\gamma_{Cal.}^{D}$	$\gamma_{Cal.}^{P}$
PA	35.9	4.9	34.0	8.0
PC	27.7	6.5	40.7	0.1
PE	35.5	0.0	27.0	0.2
PMMA	29.6	11.5	32.0	0.6
PP	30.1	0	/	/
PS	34.5	6.1	31.0	2.0
PTFE	18.4	1.6	0.0	7.9
PVC	39.5	2.0	36.9	0.1

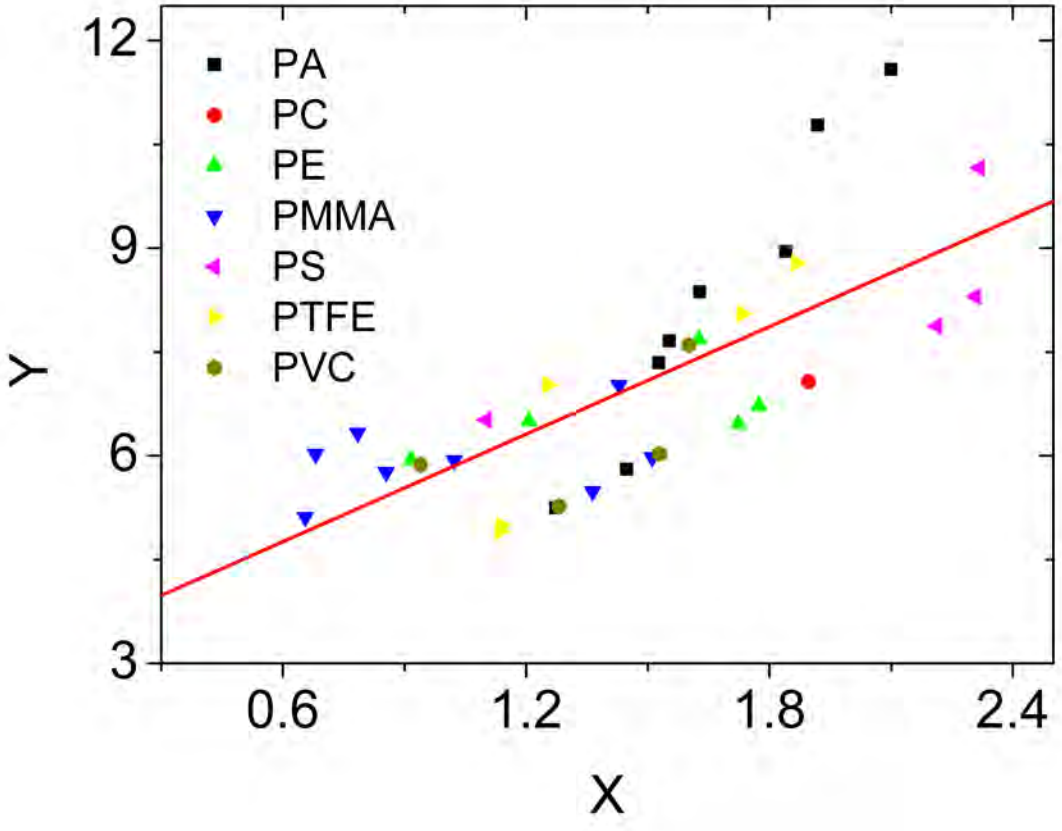

Figure 3.11: The 'OWRK' plot of the contact angle measurements on NCD:H with alcohol/water mixtures and their surface energy values, obtained from a variety of calibrated polymers. Y refers to EQ. 3.17 and X refers to EQ. 3.19.

Comparison between the four experiments

In order to have a clear discussion, different representations of the obtained surface energies are shown. In FIG. 3.12, a histogram of the total surface energies is shown. Here, the polar and disperse parts are separated in order to have an overview of their contributions to the total surface energy. FIG. 3.13 shows separately the polar and the disperse contributions in order to visualize the errors on the values. In FIG. 3.14, the values of the total surface energies of the four experiments are represented together with the error on the values.

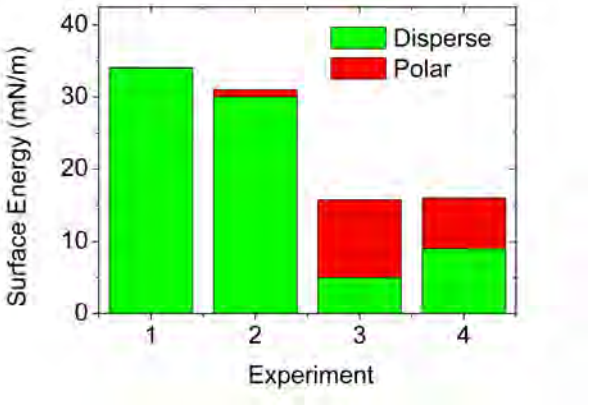

Figure 3.12: The surface energies of NCD:H derived from four experiments. The polar and disperse parts are separated in order to have an overview of their contributions to the total surface energy.

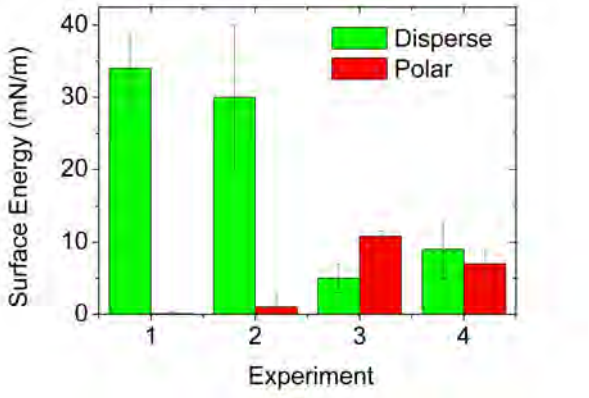

Figure 3.13: The polar and disperse parts of the surface energies, with error bars, obtained from the four experiments.

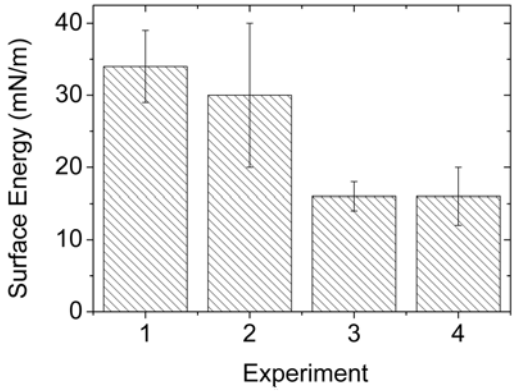

Figure 3.14: The values of the total surface energies derived from the four experiments together with the error bars.

3.3.4 Conclusions

The advantage of the first experiment are the use of pure liquids which is recommended [70] and the small error on the value of the obtained surface energy. The advantage for the second experiment is the use of more liquids which provides more data points to fit on the 'OWRK' plot. Still, the error on the surface energy for this experiment is twice as much as the value derived in Experiment 1, as one has to keep in mind that for every data point on the 'OWRK' plots, five measurements, each on a different NCD:H substrate are performed. This leads to a higher degree of measurement uncertainty, reflected by larger error bars. Therefore, one can conclude that the error on the surface energy obtained with pure liquids is trustworthy. In contrast to Experiment 2 is the fact that in Experiment 3 a different surface energy and with a smaller error was measured. We assume that the latter experiment is conducted more carefully than Experiment 2 since only one polymer was used in the calibration of the alcohol/water mixtures for Exp. 2. Even after recalibrating the polymers in Experiment 4, no evolution towards the values of Experiment 2 is detectable. Interesting is the appearance of a polar contribution to the total surface energy in Experiments 2 and 3. It is believed that this phenomenon can be explained by the presence of a higher adhesion force between alcohol and the NCD:H surface, forming a thin film between the water component of the drop and the diamond surface under study.
In general, it is concluded that the surface energy of NCD:H is $\approx$ 34 mN/m. This is in tune with the value of high quality NCD, obtained by Azevedo et al. ($\approx$ 36 mN/m) [75].

Chapter 4

Intrinsic NCD layers

In this chapter, the growth and characterization of thin intrinsic NCD films is presented. A set of systematically grown samples is used to explain the main features of high and low quality intrinsic diamond. After explaining the sample preparation and the in-situ thickness monitoring, the results of the main characterization techniques are presented and explained.

4.1 Sample preparation

Diamond growth was performed in an ASTeX 6500 series microwave plasma enhanced chemical vapor deposition (MWPECVD) reactor on a polished silicon substrate with a thickness of 500 μm. This substrate was treated with a colloidal seeding suspension of $5-10$ nm detonation diamond [39]. The temperature of the diamond layers was monitored with a Williamson Pro92 dual wavelength pyrometer. Growth was performed in a CH_4/H_2 plasma with methane concentrations of 0.5%, 1%, 2%, 4% and 8%. The substrate temperature was 775°C induced by 3500 W of microwave power and a total pressure of 20 Torr. The growth was stopped when the NCD layer reached a thickness of $\approx$ 150 nm. Cooling after growth was done in a hydrogen plasma till a pressure of 15 Torr and a temperature of 400°C was reached. The thickness of the samples was determined in-situ, by the use of laser interferometry. A 20 mW laser of Altechna which produces light waves with a wavelength of 473 nm, a silicon photo diode and an ampere meter were used. An examination of the surface morphology was performed with a scanning electron microscope (Fei Quanta 200 F). In addition to the SEM characterization, atomic force microscopy (NTEGRA Prima NT MDT) under tapping mode and at standard ambient conditions are done. In order to investigate the diamond quality, Raman spectra are obtained by a Renishaw inVia Raman Microscope. A green laser, producing 25 mW of 514 nm light was used to record the wavelength shift.

4.1.1 Laser interferometry

The grain boundary density decreases with increasing thickness which makes the diamond quality increase. Therefore, it is necessary to create samples with the same

thickness in order to compare the quality of the diamond growth. A good way to monitor the thickness of NCD layers during growth (in-situ) is interferometry. Interferometry makes use of the principle of superposition to combine separate waves together in a way that will cause the result of their combination to have some meaningful property that is diagnostic of the original state of the waves. This works because when two waves with the same frequency combine, the resulting pattern is determined by the phase difference between the two waves. Waves that are in phase will undergo constructive interference while waves that are out of phase will undergo destructive interference. FIG. 4.1 shows the signal detected by the silicon photo diode during the growth of the samples. A clear interference pattern as a function of time is visible. Since the refractive index (n_D) of diamond (≈ 2.4) is higher than the refractive index of the plasma (≈ 1) and lower than the refractive index of silicon (≈ 4.0), the constructive interference is seen at:

$$2n_D d cos\beta = m\lambda \tag{4.1}$$

and the destructive interference is seen at:

$$2n_D d cos\beta = (m - 0.5)\lambda \tag{4.2}$$

where d is the thickness of the film, λ is the wavelength of the laser, m is an integer which starts from one and increases with increasing thickness, and β is the angle from the normal of the NCD surface to the light beam, in the NCD layer. This last angle can be calculated using Snell's law:

$$n_{plasma} sin\alpha = n_D sin\beta \tag{4.3}$$

where α (28°) is the angle of incidence, and n_{plasma} is the refractive index of the plasma. When solving these equations for d, one sees that every ≈ 50 nm a constructive or a destructive interference appears, starting with a destructive interference. The first peak for the samples in FIG. 4.1 is not due to interference but due to the plasma which is warming up. This creates more background light which is absorbed by the photo diode. With all this information it is easy to derive a thickness of ≈ 150 nm for all the films, grown in this work. When timing the growth duration, we directly can calculate the growth rate of the NCD layers for different growth conditions. On FIG 4.2 the growth rates are plotted as function of C/H-ratio. Decreasing the C/H-ratio drastically lowers the growth rate of the NCD layers.

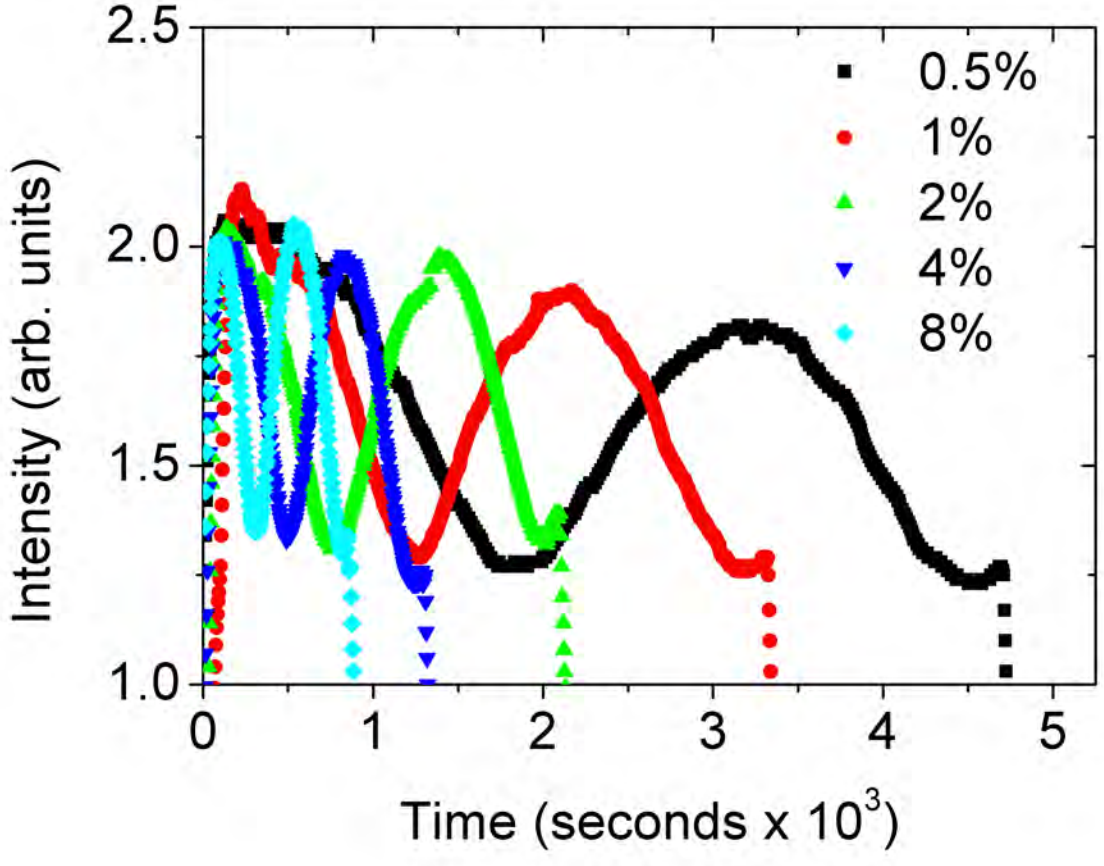

Figure 4.1: Laser interferometry signals of the 0.5%, 1%, 2%, 4% and 8% samples. The growth time systematically increases for samples grown with lower C/H-ratios and a clear interference pattern between the light reflected on the surface of the NCD and the light reflected by the silicon substrate is seen.

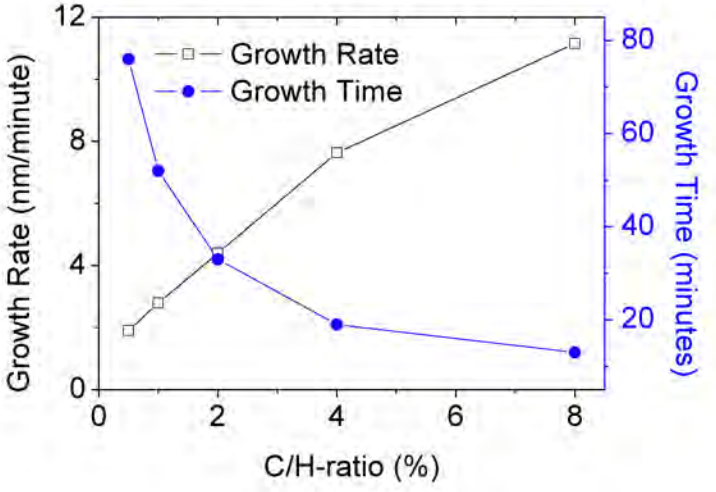

Figure 4.2: Growth rate and growth time plotted as a function of C/H-ratio. Decreasing the C/H-ratio, drastically lowers the growth rate and increases the growth time of the NCD layers.

4.2 Morphology

4.2.1 SEM

SEM measurements are important to investigate the continuity of the NCD film on the substrate. FIG. 4.3 shows that no pinholes are present in the 150 nm thick films which is due to the good seeding density. This good seeding density ensures that the films are fully covering the substrate rapidly after the growth initialization. An evidence for this is seen in FIG. 4.1 where the destructive interference quickly starts after growth initialization. The topography of the NCD films can be investigated by SEM since low energy secondary electrons are ejected from the top layer of the NCD films which reaches several nanometers of depth. These electrons are then collected to form an image. There is no visible grain size orientation although sample 0.5% shows some bigger grains which seem to have a certain orientation. This can be explained by the fact that the slow growth at 0.5% C/H-ratio leads to an earlier orientation preference although further experiments to confirm this need to be done. The grains decrease step by step in size from the 0.5% sample to the 8% sample. **Higher methane concentrations thus lead to a faster growth but also to a faster re-nucleation and smaller grains. This makes the grain boundary density which is related to non-diamond fractions increase.**

4.2.2 AFM

In addition to SEM measurements, AFM measurements are done to investigate more quantitatively the surface morphology of the layers. FIG. 4.4 confirms the grain size decrease as a function of C/H-ratio seen on FIG. 4.3. In order to compare the AFM images of all the samples, the lowest points of each AFM scan are biased to zero. The biggest difference between the highest and the lowest point for all measurements taken, determines the height scale. Only the 0.5% sample has a larger scale since the difference between its scales and the scale of the other samples is much larger. The scale of the 0.5% sample is 200 nm and the scale of the other samples is 120 nm which can be seen on FIG. 4.4. The surface roughness of the samples is determined from the AFM measurements by calculating the standard deviation of the datasets. This is often called the root mean square (RMS) roughness although in mathematics RMS has an other meaning. FIG. 4.4 also summarizes the RMS roughnesses calculated for the samples. It is clear that the sample with the biggest grains leads to a higher surface roughness. The roughness of the intermediate samples seems not to be strongly related to the methane concentration. The roughness of a second set of samples, listed in TAB. 6.1, shows the same trend as this set of samples but there, a much nicer correlation between the methane concentration and the roughness is measured. **By increasing the thickness of samples, the roughness also increases which makes the surface of the films less shiny due to light scattering.**

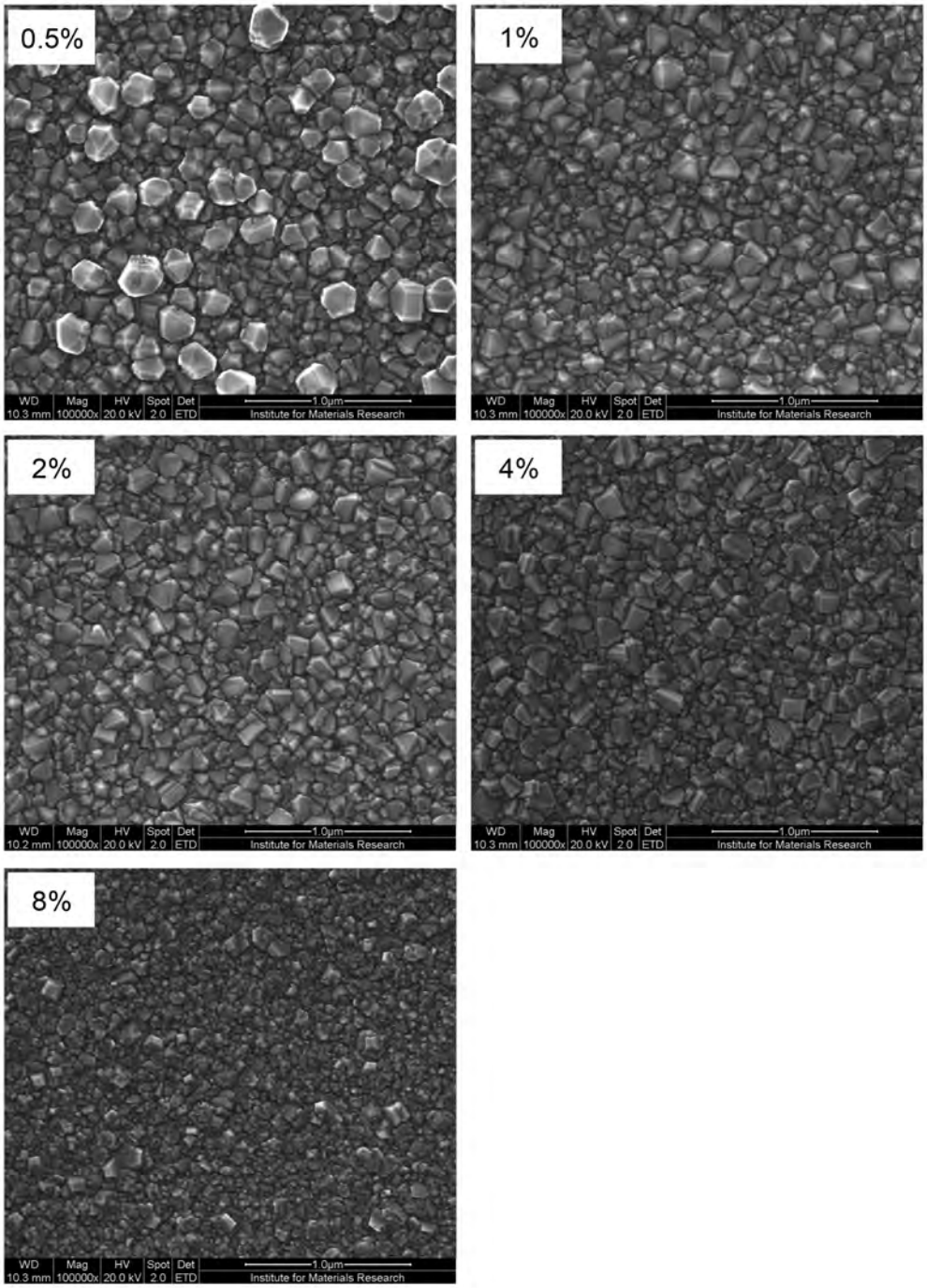

Figure 4.3: SEM images of the 0.5%, 1%, 2%, 4% and 8% samples. A smooth decrease in grain size from the 0.5% to the 8% sample is observed.

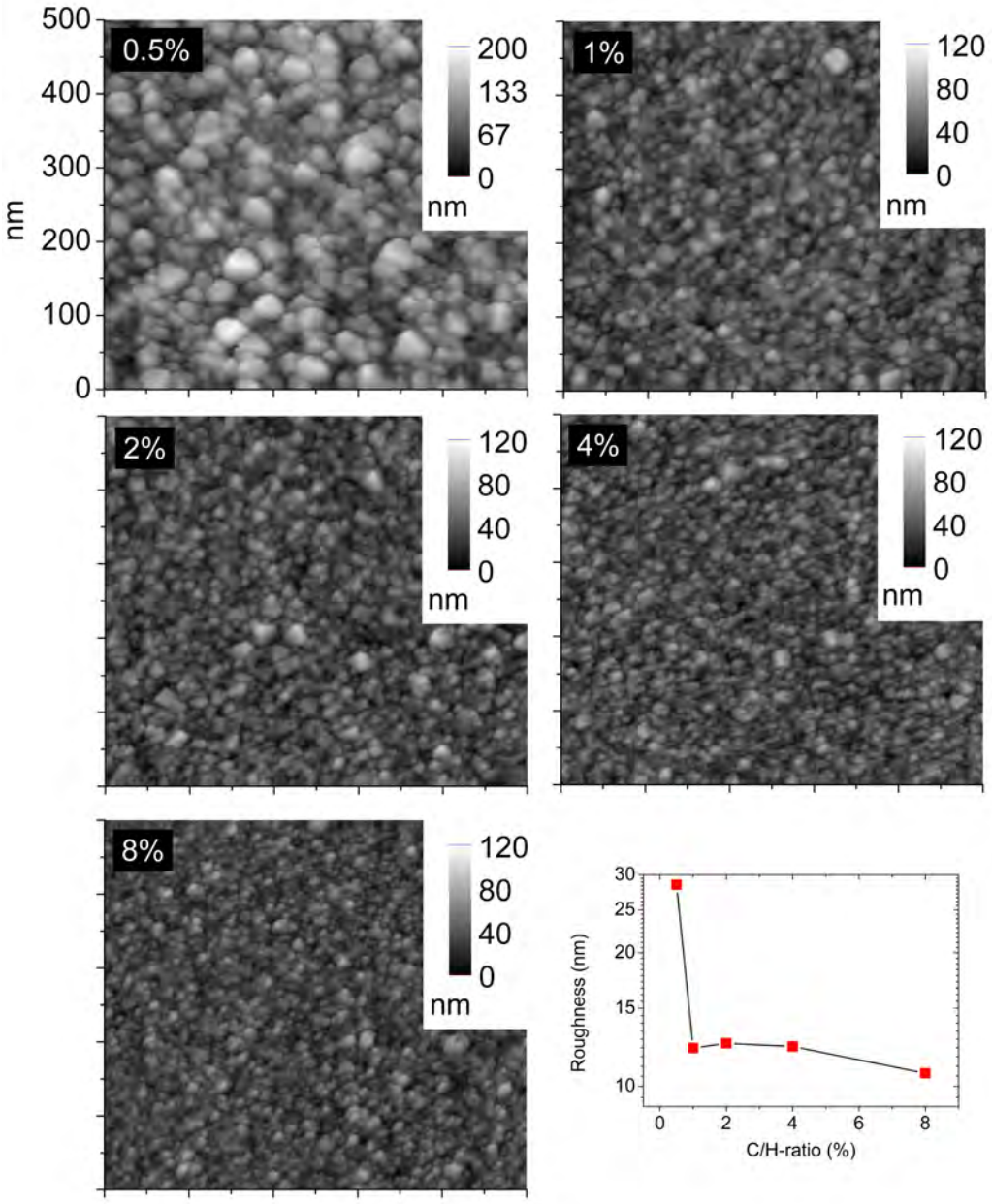

Figure 4.4: AFM images of the 0.5%, 1%, 2%, 4% and 8% samples. A decrease in grain size from the 0.5% to the 8% sample is observable. The RMS roughness of all films is summarized in the graph. A trend of decreasing roughness is observed although the 1% sample has a lower roughness than expected.

4.2.3 Raman

The quality of intrinsic single crystal and polycrystalline diamond layers can be compared by the use of Raman spectroscopy [23, 24]. In FIG. 4.5 we can see the Raman shift signal of the five samples. The diamond peak (P3) at 1332 cm^{-1} is clearly observable for all samples. The maximum of this peak is for each sample biased to the same intensity in order to compare the peak heights. Except for the diamond peak, also the 1150 (P1), 1240 (P2), 1350 (P4), 1480 (P5) and 1550 cm^{-1} (P6) peaks are observed. The peaks at 1350 cm^{-1} and 1550 cm^{-1} are the D and G peaks of amorphous carbon. Since they are broad in comparison with the diamond peak, they are also called the D and G bands. The peak at 1150 cm^{-1} has been attributed to nanocrystalline diamond [76, 77, 78]. Many researchers have since followed this assignment. However, it is demonstrated by analyzing the Raman spectra taken at different excitation energies that this peak and the companion peak at ca. 1480 cm^{-1} are a signature of trans-polyacetylene [79] and have nothing to do with C-C sp^3 vibrations. A detailed discussion of the vibrations and Raman spectra of trans-polyacetylene is found in the contribution of Castiglioni et al . (2004) [80]. In a surface-enhanced Raman spectroscopy study of trans-polyacetylene in CVD diamond, a small peak at ca. 1240 cm^{-1} was also detected [81]. This peak is further evidence of trans-polyacetylene, as it normally has a third peak at this frequency, with smaller intensity than P1 and P5 [82]. Usually this third peak is not observed, due to its small intensity and the dominance of the D band at that frequency. The trans-polyacetylene peak probably represents the sp^2 and hydrogen fractions at the grain boundaries. Since these films are made in a very systematical way, there is a clear evidence that the diamond peak decreases with increasing methane concen-

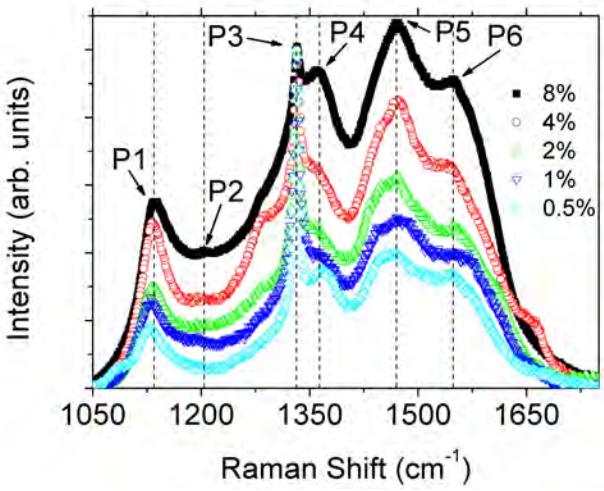

Figure 4.5: The Raman spectra of the 0.5%, 1%, 2%, 4% and 8% samples. The maximum of the diamond peak for each sample is biased to the same intensity. A smooth decrease of the diamond quality as a function of the C/H-ratio is observed.

tration. This is the final proof that the diamond quality increases when it is grown under lower C/H-ratios.

4.3 Conclusion

By preparing samples very systematically, it is possible to generate a series of thin NCD films with varying quality. The systematic set of NCD films is made by fixing all possible parameters but only changing the methane to hydrogen ratio during the MWPECVD process. The grain size of the investigated samples, observed by SEM and AFM, becomes smaller as a function of C/H-ratio. Due to this observation, one can conclude that the grain boundary density increases as a function of C/H-ratio. A higher methane concentration also leads to a lower surface roughness. Smaller grains will logically have less points sticking out of the average surface height which leads to this effect. The Raman spectra of the samples clearly show a nice decrease in diamond quality as a function of a higher C/H-ratio. Carbon phases which are not related to diamond but to defects, including grain boundaries, increase as a function of C/H-ratio with respect to the diamond signal.
Chapter 6 shows how a systematic set of samples can be used in the investigation of the fundamental properties of heavily boron-doped NCD films. Due to the interference of boron with the Raman shift, it is not clear what the quality of these films is. This is one of the main reasons for performing this study. The grain size and the roughness of the films in chapter 6 will be used as a measure for diamond quality.

Chapter 5

Electronic transport measurements

5.1 Theory

5.1.1 Electronic resistance

The best way to measure the electronic resistivity of a material (ρ) is by making a Hall bar shape of this material which is presented in FIG. 5.1. In section 5.2.2, one can find references which describe the geometrical restrictions to obtain trustworthy measurements for shape. By maintaining a constant current (I) between points 1 and 4 and measuring the voltage difference between points 2 and 3 and/or 6 and 5 (V_ρ), it is possible to calculate only the resistivity of a material using Ohm's law. By knowing the thickness (d) of the layer from which the shape is made, the width of the path between points 1 and 4 (w) and the average length between points 2 an 3 (or points 6 and 5) (s), it is possible to calculate the resistivity (ρ) of the conducting material:

$$\rho = \frac{V_\rho d w}{I s} \ . \tag{5.1}$$

When having a temperature controlled cryostat or oven, it is possible to measure the temperature dependence of the resistivity.
The electrical resistivity of most metals is dominated at room temperature by collisions of the charge carriers with lattice phonons and at liquid helium temperatures (4 K) by collisions with impurity atoms and mechanical imperfections in the lattice. The rates of these collisions are often independent to a good approximation, so that if the electric field were switched off, the momentum distribution would relax back to its ground state with the net relaxation time:

$$\frac{1}{\tau} = \frac{1}{\tau_L} + \frac{1}{\tau_i} \tag{5.2}$$

where τ_L and τ_i are the collision times for scattering by phonons and by impurity imperfections, respectively. Due to Ohm's law:

$$\rho = \frac{1}{\sigma} = \frac{m_e}{nQ^2\tau} \tag{5.3}$$

where Q is the magnitude of the electronic charge, m_e is the mass of an electron and n is the electron density, one can write:

$$\rho = \rho_L + \rho_i \tag{5.4}$$

where ρ_L is the resistivity caused by thermal phonons and ρ_i is the resistivity caused by scattering of the charge carrier waves by static defects that disturb the periodicity of the lattice. This empirical observation expresses Matthiessens's rule which is convenient in analyzing experimental data.

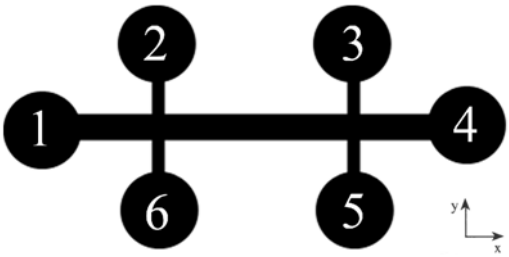

Figure 5.1: The Hall bar shape with numbered contact areas.

5.1.2 Electronic mobility

The conductivity (σ) of a semiconductor is given by:

$$\sigma = \frac{1}{\rho} = q(\mu_n n + \mu_p p) \tag{5.5}$$

where μ_n is the mobility of the negative charges and μ_p is the mobility of the positive charges, n is the electron density of the negative charges, q is the elementary charge and p is the charge carrier density of the positive charge carriers. When negative charge carriers are negligible, the latter equation can be written as:

$$\mu_p = \frac{\sigma}{qp} = \frac{1}{qp\rho} \tag{5.6}$$

Since $1/\mu \propto \rho$ and $\rho \propto 1/\tau$ one can write:

$$\frac{1}{\mu} = \frac{1}{\mu_L} + \frac{1}{\mu_i} \tag{5.7}$$

where μ_L is the mobility contribution of thermal phonons and μ_i the mobility contribution by scattering of the charge carrier waves by static defects that disturb the periodicity of the lattice. The latter equation is the mobility variant of Matthiessen's rule.

5.1.3 Hall effect

The Hall effect was discovered by Hall in 1879 [84]. Hall studied the nature of the force acting on a conductor carrying a current in a magnetic field (**B**). As schematically shown in FIG. 5.2, the charge carriers (p-type sample) in the conductor become deflected by the magnetic field and give rise, when a steady state condition is reached, to a positive electric field (Hall voltage) that is perpendicular to both the current and the magnetic field. For an n-type sample, the electrons are also deflected to the bottom of the sample for the same current direction as that in FIG. 5.2, because they flow in the opposite direction to holes and have opposite charge. The force which acts on the charge carriers, before reaching a steady state condition, is known as the Lorentz force and can be written as a vector expression:

$$\mathbf{F} = Q(\mathbf{E} + \mathbf{v} \times \mathbf{B}) \tag{5.8}$$

where **E** is the electric field and **v** is the instantaneous velocity of the particle. This equation can be reduced for electrons and holes in the case of FIG. 5.2 where **E** and **B** are perpendicular to each other:

$$F_{ey} = -q(E_y + v_{ex}B_z) \tag{5.9}$$

$$F_{hy} = q(E_y - v_{hx}B_z)\ . \tag{5.10}$$

The total current density in the y-direction is given by:

$$J_y = J_{ey} + J_{hy} = qnv_{ey} + qpv_{hy}\ . \tag{5.11}$$

When a steady state condition is reached, there is no force thus no current in the y-direction which gives the following expressions:

$$E_y = -v_{ex}B_z \tag{5.12}$$

$$E_y = v_{hx}B_z \tag{5.13}$$

$$pv_{hy} + nv_{ey}\ . \tag{5.14}$$

When the mobility in all directions is the same and one replaces all the drift velocities of the latter three equations by $v_{hy} = \mu_h E_y$, $v_{hx} = \mu_h E_x$, $v_{ey} = \mu_e E_y$ and $v_{ex} = \mu_e E_x$

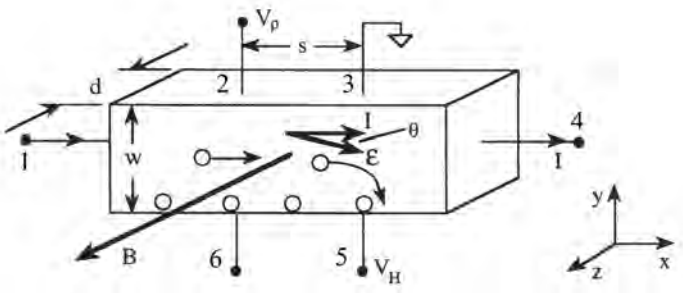

Figure 5.2: Schematic illustrating the Hall effect in a p-type sample. The numbered contacts of FIG. 5.1 are added to the schematic [83].

one gets:

$$E_y = -\mu_e E_x B_z \tag{5.15}$$

$$E_y = \mu_h E_x B_z \tag{5.16}$$

$$p\mu_h E_y + n\mu_e E_y \ . \tag{5.17}$$

Filling in the two expressions of E_y in the latter equation results in:

$$(p\mu_h^2 - n\mu_e^2)E_x B_z = (p\mu_h + n\mu_e)E_y \ . \tag{5.18}$$

The total current density in the x-direction can be written as:

$$J_x = q(nv_{ex} + pv_{hx}) = (p\mu_h + n\mu e)qE_x \tag{5.19}$$

and substituting E_y for EQ. 5.18 and J_x for EQ. 5.19 in the expression of the Hall coefficient, we obtain the expression used in Hall effect calculation for ambipolar conduction:

$$R_H = \frac{E_y}{J_x B_z} = \frac{p\mu_h^2 - n\mu_e^2}{q(p\mu_h + n\mu e)^2} \tag{5.20}$$

$$R_H = \frac{p - nb^2}{q(p + nb)^2} \tag{5.21}$$

where $b = \mu_e/\mu_h$. It is clear that the Hall coefficient depends on both the drift mobility ratio and the concentration of holes and electrons. For $p > nb^2$, R_H will be positive and for $p < nb^2$, it will be negative. When $p \gg n$ or $n \gg p$, the latter relation reduces to:

$$R_H = \frac{1}{qp} \ or \ R_H = -\frac{1}{qn} \ . \tag{5.22}$$

These equations are derived under simplified assumptions of energy-independent scattering mechanisms. With this assumption relaxed, the expression for the hole and electron densities become [85, 86]:

$$R_H = \frac{r}{qp} \ ; R_H = -\frac{r}{qn} \tag{5.23}$$

where r is the Hall scattering factor. The scattering factor depends on the type of scattering mechanism in the semiconductor and generally lies between 1 and 2. For lattice scattering, $r = 3\pi/8 = 1.18$; for impurity scattering $r = 315\pi/512 = 1.93$ and for neutral impurity scattering $r = 1$ [85]. The scattering factor is also a function of magnetic field and temperature; r can be determined by measuring R_H in the high magnetic field limit since $r = 1$ for $B = \infty$.

5.2 Noisy Hall effect measurements

In the next chapter, data from Hall effect measurements is used to determine the charge carrier concentration and mobility in heavily boron-doped nanocrystalline diamond (B:NCD). Due to the low mobility and relative high resistivity of this material, one has to deal with noisy Hall effect measurements. A good estimation of the error on the Hall voltage is necessary to perform a correct data analysis. Therefore, a new algorithm to calculate the Hall voltage and the error on the Hall voltage derived for an alternating magnetic field method is developed. A proof of principle, performed on B:NCD, is demonstrated by investigating the linearity of the Hall voltage as a function of the magnetic field. Also a comparative study between the errors induced by "good" ohmic Ti/Al contacts and "bad" conductive silver paint contacts on B:NCD is performed to optimize the Hall effect measurements.

5.2.1 Introduction

Not only for B:NCD but also for conducting materials with high resistivity values like oxides including cuprates such as $La_{2-x}Sr_xCuO_4$ ($x = 0.2$ and 0.25) [87], manganites such as $Pr_{0.5}Sr_{0.5}MnO_3$ [88], phosphorus-doped diamond [89] and boron-doped diamond [90]; with a low mobility like ZnO [91] and boron-doped nanocrystalline diamond [92, 93]; with non-ohmic contacts [94] or a combination of these properties, a clear Hall effect signal is sometimes difficult to obtain. In this work, we go deeper into the experimental details of Hall effect measurements which are performed on heavily boron-doped nanocrystalline diamond (B:NCD). This material suffers from a high resistivity, compared to metals, and a low mobility due to the influence of grain boundaries [95]. A thin film of B:NCD is deposited by microwave plasma enhanced chemical vapor deposition (MPECVD) [96]. Possible sources of errors for Hall voltages coming from the geometry of a sample and the placement of contacts on this sample [97, 98, 99], and intrinsic factors [100, 101, 102] are studied. Here, the aim is to develop a way of extracting the Hall effect even when measurements are subjected to electronic noise, making it seemingly impossible to extract useful data. In order to do this, a method which involves altering the magnetic field (B) is described. For this method, equations to calculate the Hall voltage (V_H) and the error on V_H (ΔV_H) are derived. To demonstrate the use and the feasibility of these equations, the linearity of the Hall effect as function of the magnetic field is investigated for a thin B:NCD film. Even when measuring at the lowest magnetic fields, where the signal-to-noise ratio (S/N) approaches zero, one is able to identify a significant Hall voltage. A low S/N can also be induced by contacts of a poor quality and to demonstrate this, a quantitative comparison between ohmic Ti/Al [67] and conductive silver paint contacts is intentionally made.

5.2.2 The evaluation of the Hall voltage

The Hall voltage

General equations to calculate V_H and ΔV_H are derived from an alternating magnetic field method. To carry out this method, the current through the sample, the

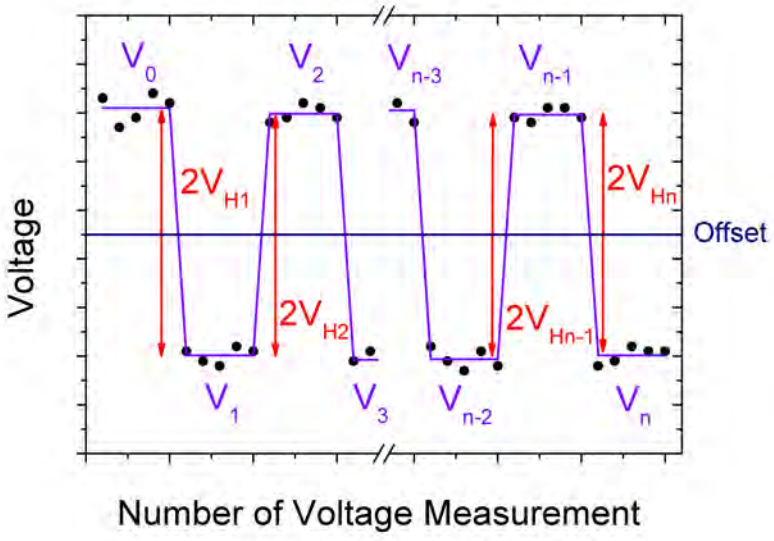

Figure 5.3: A signal of a fictitious Hall effect measurement with an alternating magnetic field, a constant current for one current direction and a constant temperature. This figure is used to theoretically derive the equations for calculating V_H and ΔV_H. The same measurement with the reversed current through the sample is necessary to eliminate intrinsic error sources [100] .

temperature and the magnetic field should be kept quasi constant to obtain a high S/N. By reversing the magnetic field polarity several times during one experiment it is possible to measure more than one value for the Hall voltage in order to get a smaller value for ΔV_H. After using one current direction, the other current direction can be applied for a second Hall measurement. The average of the two Hall voltages for both current directions can be used as the correct Hall voltage. Alternating the magnetic field is necessary to correct for a misalignment voltage. This voltage is induced by an additional longitudinal resistance between the two contacts, used for measuring the Hall voltage. The longitudinal resistance can occur when the two latter contacts are not 100% perpendicularly aligned to the current through the sample. Also, when a film is inhomogeneous [101, 102] or the geometry and the contacts placement is not optimal [97, 98], an error on the Hall voltage is induced. A square sample already has an error on the Hall voltage and big contacts, not placed on the corners even enhances the error. A Hall bar pattern which is discussed later is one of the most accurate geometries and provides a solution to geometry and contact problems. It has to be stressed that with the Hall bar geometry some rules have to be followed in designing it. When the temperature is not perfectly stable and/or the temperature dependence of the resistivity is very high, the offset voltage can drift over time, hindering a correct determination of the actual V_H. A magnet, mostly a non-superconducting electromagnet, which switches rapidly between field

directions can solve the drift and the misalignment voltage to a considerable extent. When experiments with high magnetic fields are conducted and a remnant magnetization of the superconducting coil influences the magnetic field, and/or the material itself shows a magnetic hysteresis, a slow magnetic field reversal is recommended [88, 103]. A thermoelectric voltage, induced by a temperature gradient over the sample which allows two contacts to act as a pair of thermocouple junctions, and a voltmeter offset are also canceled by altering the magnetic field. Even when the misalignment voltage depends on the magnetic field, due to a large magnetoresistance of the material, the misalignment voltage is canceled by altering the magnetic field. If no external transverse temperature gradient exists, the sample can set up its own. The Lorentz force shunts slow and fast electrons to the sides in different numbers and causes an internally generated Seebeck effect. This phenomenon is known as the Ettingshausen effect [104]. Unlike the Seebeck effect, the generated voltage is proportional to both current and magnetic field. By altering the magnetic field or the current, it is not possible to cancel this thermomagnetic voltage. If a longitudinal temperature gradient exists across the sample, then charge carries tend to diffuse from the hot end of the sample to the cold end and this diffusion current is affected by a magnetic field, producing a Hall voltage which is called the Nernst voltage [105]. This voltage can be canceled by switching the current. Also the Righi-Leduc voltage [106] can be canceled this way. The Nernst (diffusion) electrons also experience an Ettingshausen-type effect since their spread of velocities result in hot and cold sides and thus again set up a transverse Seebeck voltage, known as the Righi-Leduc voltage.

Fig. 5.3 will now be used to theoretically derive the equations for V_H and ΔV_H. This figure represents a fictitious Hall effect signal where B is altered n times for a constant current through the sample. This way, it is possible to measure n Hall voltages and to average them. At this point, the current through the sample is still in one direction. For the first Hall voltage (V_{H1}) the first measured voltage (V_0) with magnetic field B and the second voltage (V_1) with magnetic field $-B$ have to be measured. The difference between V_0 and V_1 is twice V_{H1}. This is graphically shown in Fig. 5.3 and described in the following equation:

$$V_H = V_{H1} = \frac{V_0 - V_1}{2} \,. \tag{5.24}$$

The direction of the first magnetic field is not important, it just has to switch to the opposite direction for each next voltage measurement. However, if one wants to calculate the dominant type of charge carriers, the orientation of the magnetic field and the current direction through the sample must be known. The variance of V_0 can be used to calculate ΔV_0. This implies that V_0 is an average value of a couple measuring points. FIG. 5.3 shows five measuring points which are used to calculate V_0 and ΔV_0. If one measures V_0, V_1 and V_2 the averaged Hall voltage is given by:

$$V_H = \frac{V_{H1} + V_{H2}}{2} = \frac{-V_1}{2} + \frac{V_0 + V_2}{4} \,. \tag{5.25}$$

For $n+1$ voltage measurements with n times altering B one measures n Hall voltages with an averaged value expressed as:

$$V_H = \frac{1}{n} \sum_{i \notin 0,n} V_i (-1)^i + \frac{1}{2n} \sum_{i \in 0,n} V_i (-1)^i \,. \tag{5.26}$$

The sign of V_H depends on the dominating type of charge carriers, the magnetic field orientation and the current direction. After changing the current direction, this formula can be applied in the same way to calculate the second V_H and the absolute values of the two Hall voltages can be averaged:

$$V_H = \frac{|V_{H+}| + |V_{H-}|}{2} \tag{5.27}$$

where V_{H+} is the Hall voltage for the first current direction and V_{H-} is the Hall voltage for the reverse current direction.

Error Calculation

In Eq. 5.26 the measured voltages (V_i) are not related and their errors are not related either. Therefore one can apply the general equation of error propagation [107]:

$$\Delta X = \sqrt{\left|\frac{\partial f}{\partial A}\right|^2 \cdot \Delta A^2 \; + \left|\frac{\partial f}{\partial B}\right|^2 \cdot \Delta B^2 \; + \ldots} \tag{5.28}$$

where ΔX is the propagated absolute error, $\partial f/\partial A$ is a partial derivative of a function f to the variable A with error ΔA. Translated to Eq. 5.26, ΔV_H is expressed as:

$$\Delta V_H = \sqrt{\sum_{i \notin 0,n} \left(\frac{\Delta V_i}{n}\right)^2 + \sum_{i \in 0,n} \left(\frac{\Delta V_i}{2n}\right)^2}. \tag{5.29}$$

This equation can easily be programmed to evaluate the values for the two current directions. The end value of ΔV_H can be calculated by applying Eq. 5.28 on Eq. 5.27.

5.2.3 Boron-doped nanocrystalline diamond

Experimental

Diamond growth was performed in an ASTeX 6500 series microwave plasma enhanced chemical vapor deposition (MPECVD) reactor on an electronic isolating fused silica substrate. This substrate was treated with a colloidal seeding suspension of $5-10$ nm detonation diamond [39]. The temperature of the diamond layer was monitored with a Williamson Pro92 dual wavelength pyrometer. Growth was performed in a CH_4/H_2 plasma with a methane content of 1%. Doping was induced by trimethyl boron gas ($B(CH_3)_3$) with a 5000 ppm B/C-ratio in the gas phase. The substrate temperature was 700°C induced by 3500 W of microwave power and a total pressure of 25 Torr. The growth was stopped when the B:NCD layer reached a thickness of ≈150 nm. Cooling after growth was done in a hydrogen plasma till a pressure of 15 Torr and a temperature of 400°C was reached. The thickness of the as grown sample was determined ex-situ, at standard ambient temperatures, by the use of ultraviolet-visible spectroscopy. In order to perform Hall effect measurements, the sample was etched into a Hall bar pattern (FIG. 5.4) using an oxygen plasma (3 min, 300 W, 5.6 μbar) in combination with a protective Al mask (200 nm) produced by magnetron sputtering and lift-off photolithography. This procedure allows the complete removal of the unmasked B:NCD parts, exposing the fused silica substrate.

After removing the Al mask with an Al etchant, six Ti/Al contacts (50 nm/200 nm) with a diameter of 1.5 mm were deposited by magnetron sputtering [108]. Hall- and resistivity measurements were performed in an Oxford instruments MicrostatHe cryostat with a fixed temperature of 400 K. The Hall voltage was measured with a Keithley 2400 SourceMeter. Through the sample, a current of 1.5 mA was provided by a Keithley 6221 current source. Magnetic fields were generated by a tapered pole electromagnet of Brucker which was calibrated by a home build Hall probe. A LakeShore HGT-2010 Hall effect sensor, calibrated up to 2 T, was used in this probe. FIG. 5.5 shows the magnetic field as a function of the current through the coils of the magnet. The magnetization of the setup at 0 A before and after the calibration is negligible. For each magnetic field direction, ten voltage measurements were done to generate an average voltage (V_i) and its error (ΔV_i). The magnet was altered ten times for each current which gave V_{H+} and V_{H-}.

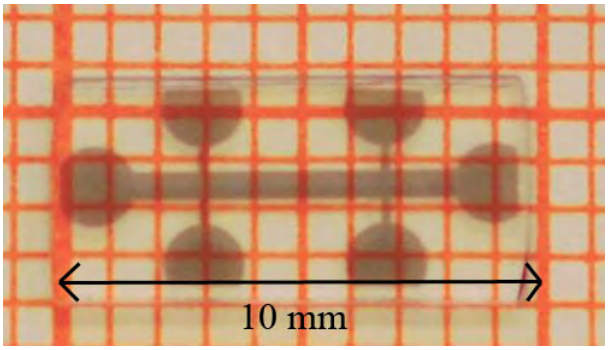

Figure 5.4: A 10 mm by 5 mm Hall bar pattern of 150 nm thick B:NCD on fused silica. The scale is illustrated by millimeter paper. The width of the conduction path is 0.6 mm and the width of the path to the contacts for the voltage measurements is 0.2 mm.

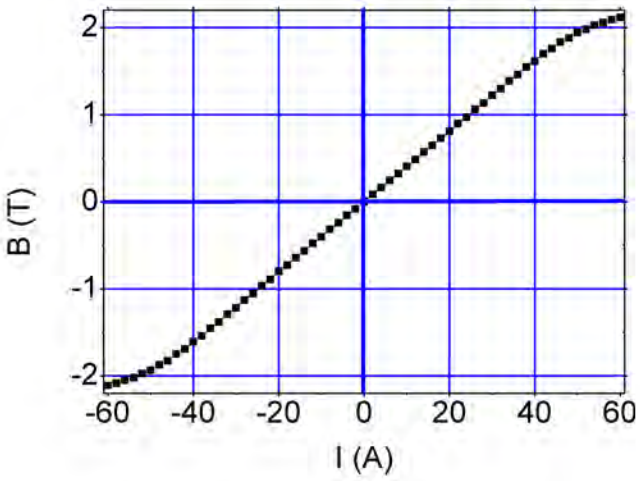

Figure 5.5: The magnetic field as function of the current through the coils of the electromagnet.

The dependence of V_H on B

FIG. 5.6(a) shows the data of the Hall measurements performed on Ti/Al contacts for alternating 0.1 T and 2 T fields. The offset voltage is subtracted from the data and is approximately one thousandth of the voltage over the bar, produced by the 1.5 mA measuring current. The 2 T field generates a clear Hall signal but for the 0.1 T field, no Hall signal is observed since it is below the noise level. Still, after evaluating the data for the 0.1 T field by equations 5.26 and 5.29, a Hall voltage can be extracted from the very noisy data. Table 5.1 summarizes the signal-to-noise ratios for both magnetic fields which are calculated by dividing V_H by ΔV_H. The value for the 2 T field appears to be about twenty times higher than for the 0.1 T field, which is expected when V_H is proportional to the magnetic field. To prove the linear dependence of V_H as a function of B, Hall voltages from 0.1 T to 2 T fields in steps of 0.1 T are measured. FIG. 5.6(b) gives an overview of the Hall voltages as a function of the magnetic field with the least squares regression line ($y = a + bx$). The value of the intercept (a) is 0.6 ± 0.8 μV and of the slope (b) is 35.0 ± 0.6 μV. These low errors prove that V_H is linearly dependent on the applied magnetic field. It also proves that for the 0.1 T field, the values of V_H and ΔV_H are reliable.

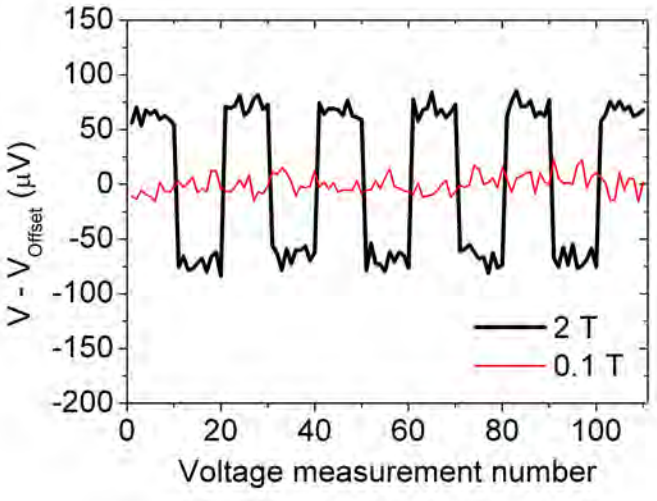

(a)

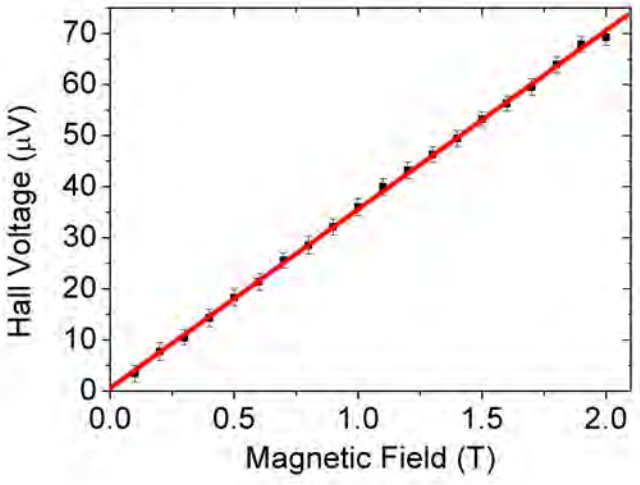

(b)

Figure 5.6: The first graph (a) shows the normalized data of the voltage measurements on the B:NCD sample with Ti/Al contacts for alternating 2 T and 0.1 T magnetic fields. A constant current of 1.5 mA generates an offset voltage of 3.5 mV which is manually subtracted from the original data. The second graph (b) summarizes all the Hall voltages as a function of the magnetic fields, averaged for both current directions. The least squares regression line of these values proves the linear dependence of the Hall voltage on the magnetic field.

The influence of contacts on ΔV_H

The presented method is not only effective for measuring Hall voltages at low magnetic fields but also when the noise is large due to contacts of poor quality. To illustrate this, we deliberately made conductive silver paint contacts and compared them with good ohmic contacts [67, 109, 110]. FIG. 5.7(a) shows the Hall effect measurements for a one current direction and a 2 T alternating magnetic field performed with the ohmic Ti/Al and the bad silver paint contacts. The measurement with the silver paint contacts is much more noisy than the measurement with the Ti/Al contacts. Table 5.1 shows the data, evaluated by equations 5.26 and 5.29, and one can see a S/N which is about twenty times higher for the Ti/Al than for the silver paint contacts. For the Ti/Al contacts, the S/N at 0.1 T is almost the same as for the silver paint contacts at 2 T. FIG. 5.7(b) shows the Hall voltages for the silver paint contacts going from 0.1 T to 2 T in steps of 0.1 T. Here, the results for the least squares regression line ($y = a + bx$) are 0 ± 2 μV for a and 40 ± 10 μV for b. By the use of equations 5.26 and 5.29 the measurements on the silver paint contacts are still significant.

Table 5.1: The values of V_H, ΔV_H and S/N for the 0.1 T and 2 T magnetic fields with Ti/Al contacts and silver paint contacts.

Contacts	B (T)	V_H (μV)$\pm\Delta V_H$	S/N
Ti/Al	2.0	69 ± 2	34.5
Ti/Al	0.1	3 ± 2	1.5
Ag Paint	2.0	80 ± 40	2
Ag Paint	0.1	0 ± 40	0

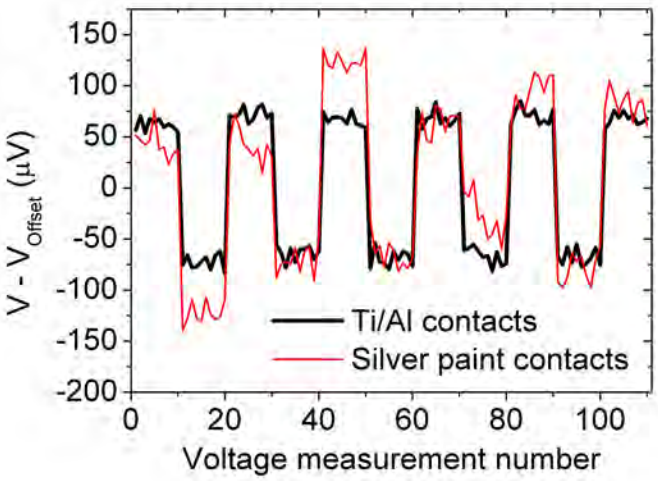

(a)

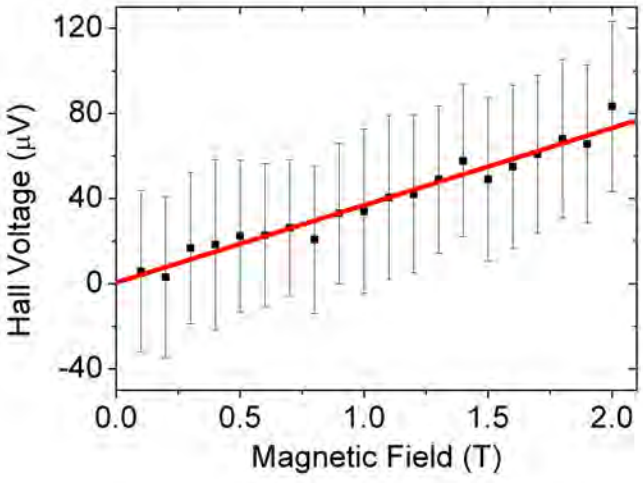

(b)

Figure 5.7: The first graph (a) shows the normalized data of the voltage measurement on the B:NCD sample with Ti/Al and silver paint contacts for an alternating 2 T field. The same offset voltage is generated by a current of 1.5 mA which is manually subtracted from the original data. The second graph (b) summarizes all the Hall voltages as a function of the magnetic fields, averaged for both current directions and performed with silver paint contacts. This proves that the S/N is much higher for silver paint contacts than for Ti/Al contacts.

5.2.4 Conclusions

An alternating field method to measure the Hall effect is described and equations to evaluate the Hall voltage for this method are presented. The strength of this method is the direct elimination of a possible misalignment voltage and/or thermoelectric voltage. The practical use of the alternating magnetic field method and its equations derived in this work is demonstrated by measuring the Hall effect in a thin heavily boron-doped nanocrystalline diamond layer. For this material, the linearity of the Hall voltage as a function of the magnetic field is proven to be linear and the influence of the type of contacts is evaluated. The signal-to-noise ratio of the Hall voltage measured with Ti/Al contacts in a magnetic field of 2 T is 34.5 and for the same experimental conditions the signal-to-noise ratio of the Hall voltage measured on silver paint contacts is just 2. Despite the silver paint contacts generating a low S/N ratio, significant Hall voltages can be measured when performing sufficient measurements with the evaluation procedure presented in this work.

Chapter 6

Heavily boron-doped NCD

6.1 Introduction

A systematic study on the morphology and the electronic properties of heavily boron-doped nanocrystalline diamond (B:NCD) thin films is presented. The films have nominally the same thickness ($\approx$ 150 nm), are grown with a fixed B/C-ratio (5000 ppm) but with different C/H-ratios ($0.5 - 5\%$) in the gas phase. The morphology of the films is investigated by XRD and AFM measurements, which confirm that lower C/H-ratios lead to a larger average grain size. Magnetotransport measurements reveal a decrease of resistivity and a large increase of mobility, approaching the values obtained for single crystal diamond as the average grain size of the films increases. In all films, the temperature dependence of the resistivity decreases with larger grains and the mobility is thermally activated. It is possible to separate the intra- and inter-grain contributions for the resistivity and the mobility, which indicates that in these complex systems Matthiessen's rule is followed. The concentration of active charge carriers is reduced when the B:NCD is grown with a lower C/H-ratio. This is due to a lower boron-incorporation, which is confirmed by neutron depth profiling.

6.2 Experimental

Diamond growth was carried out in an ASTeX 6500 series MWPECVD reactor on an electronically isolating fused silica substrate which was treated with a colloidal suspension of $5 - 10$ nm detonation diamond [39]. The temperature was monitored by a Williamson Pro92 dual wavelength pyrometer. Growth was performed in a CH_4/H_2 plasma with methane concentrations up to 5%. Doping was induced by trimethyl boron gas ($B(CH_3)_3$) with a 5000 ppm B/C-ratio for all samples. The substrate temperature was 700°C induced by 3500 W of microwave power and a total pressure of 25 Torr. The growth was stopped when the B:NCD layers reached a thickness of $\approx$ 150 nm and cooling after growth was done under hydrogen flow. The thickness was determined ex-situ, at standard ambient conditions from interference fringes of a UV-VIS reflection spectrum. In total, ten samples were made by linearly decreasing the C/H-ratio from 5% to 0.5% in steps of 0.5% to generate a set of samples with

grains increasing in size due to the decrease of the C/H-ratio. An examination of the surface morphology was performed with an atomic force microscope (NTEGRA Prima NT MDT) under tapping mode and at standard ambient conditions. The X-ray diffraction study for the (111) crystal plane was carried out with a Siemens D5000 $\theta - 2\theta$ Bragg-Brentano diffractometer using the Cu $K_{\alpha 1}$ line (0.15406 nm). In order to perform electronic transport measurements, the samples were etched into Hall bar patterns (FIG. 5.4) using an oxygen plasma (3 min, 300 W, 5.6 × 10^{-3} hPa) in combination with a protective Al mask (200 nm) produced by magnetron sputtering and lift-off photolithography. This procedure allows the complete removal of the unmasked B:NCD parts, exposing the fused silica substrate. After removing the Al mask with an Al etchant, six Ti/Al contacts (50 nm/200 nm) with a diameter of 1.5 mm were deposited by magnetron sputtering [108]. Resistivity and Hall effect measurements were performed in an Oxford instruments MicrostatHe cryostat. The Hall effect was measured with a tapered pole electromagnet (Bruker) by alternating a 2 T magnetic field, reaching a complete reversal of the field in less than 20 seconds. The total boron concentration, with an error of 10%, was determined with neutron depth profiling [111, 112, 113]. The superconducting properties of the films were measured at the Institute for Nanoscale Physics and Chemistry (INPAC) of the Catholic University of Leuven by Gufei Zhang. A Heliox ^{3}He cryostat from Oxford instruments was used for this measurement.

6.3 Results and discussion

6.3.1 Structural properties

The average grain size for thin NCD layers depends on the thickness of the layers and on the C/H-ratio when all other growth parameters are kept constant. Therefore, all samples were grown to a fixed thickness of 150 ± 15 nm confirmed by UV-VIS reflection interferometry. FIG. 6.1 shows the amount of reflection of some samples. A clear interference pattern as a function of photon energy is visible. Unlike section 4.1.1, the destructive interference is now seen at:

$$2n_D d cos\beta = m\lambda \tag{6.1}$$

and the constructive interference is seen at:

$$2n_D d cos\beta = (m - 0.5)\lambda \tag{6.2}$$

due to the low refractive index of fused silica (≈ 1.46).
The influence of boron doping on the diamond first-order Raman line has been well characterized for single and polycrystalline diamond films, and it has been explained by the Fano-type interference between the continuum of electronic states introduced by the dopants and the discrete zone-center phonon [24]. For heavily boron-doped diamond, the interference dominates and therefore, it is not suitable for characterizing the quality of heavily boron-doped diamond. FIG. 6.2 shows the Raman spectra of the 1%, 2%, 3%, 4% and 5% films with no clear quality difference due to the dominating Fano interference.

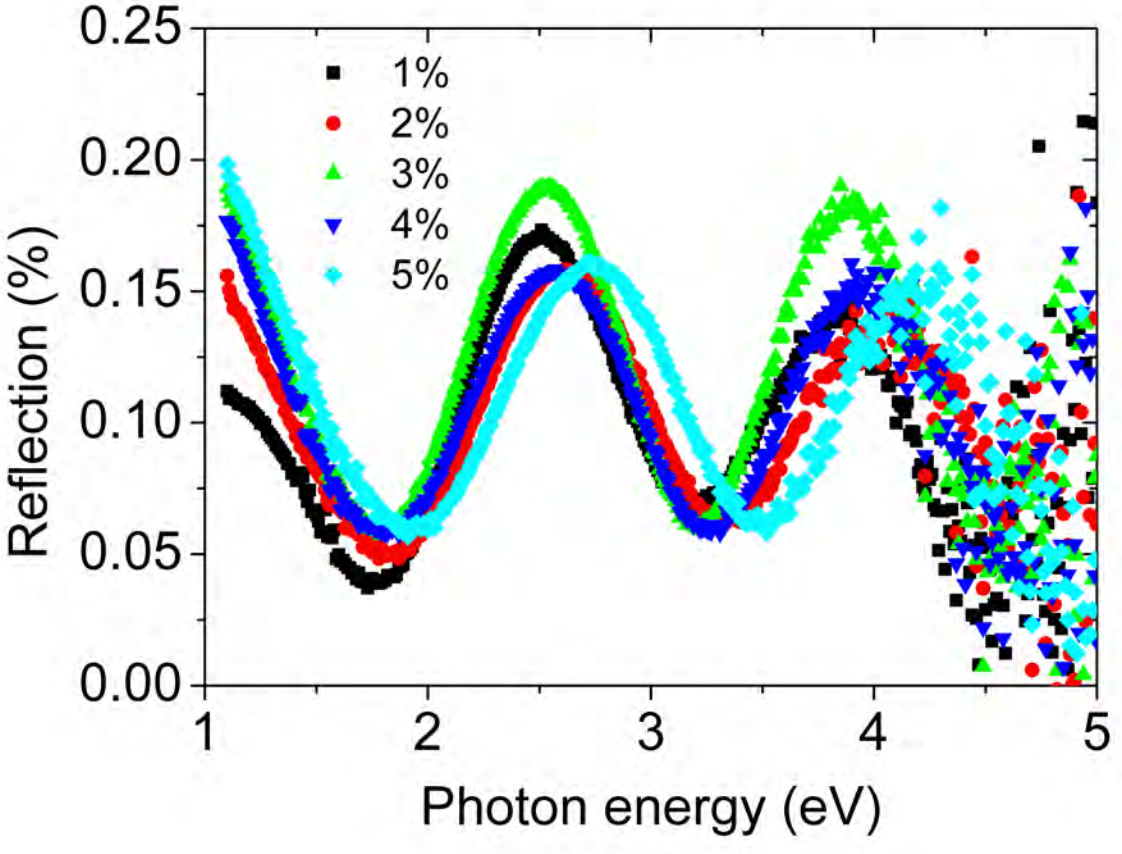

Figure 6.1: The film thickness of the samples is estimated from the interference maxima and minima positions in the reflection spectra.

Table 6.1: Summary of the main morphological characteristics of the B:NCD films as a function of the C/H-ratio. The grain sizes are calculated from XRD spectra and the roughnesses are calculated from AFM measurements.

C/H-ratio (%)	Growth Rate (nm/minute)	Grain Size (nm)	Roughness (nm)
1	2.0	67	18.4
2	3.5	61	15.3
3	4.4	50	13.2
4	4.9	54	12.0
5	5.1	47	8.2

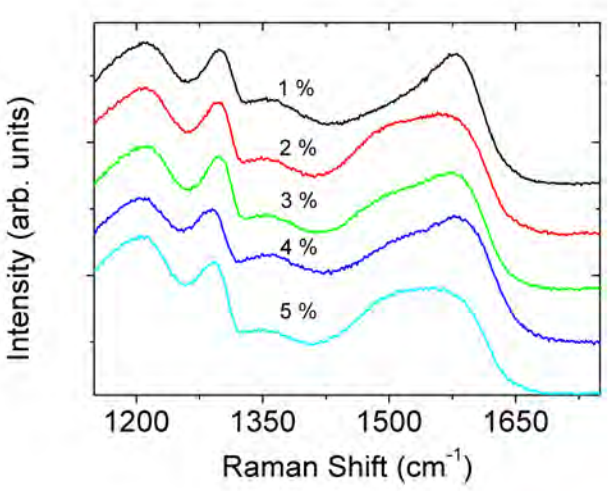

Figure 6.2: The Raman spectra of the 1%, 2%, 3%, 4% and 5% films with no clear quality difference due to the dominating Fano interference.

AFM measurements (FIG. 6.3) show an increasing grain size with decreasing C/H-ratio. The surface roughness (see TAB. 6.1) calculated from the AFM measurements increases from 8 nm to 18 nm with decreasing C/H-ratio. This correlates nicely with the increase in grain size as the C/H-ratio decreases. SEM measurements (FIG. 6.4) also show an increase of grain size with decreasing C/H-ratio. After XRD eperiments, the Scherrer equation was used to calculate the mean size of the crystalline domains in the films [114]

$$\tau_{cd} = \frac{K\lambda}{\varphi cos\theta_B} \leq d_{gs} \tag{6.3}$$

where K is the shape factor which varies with the shape of the crystallite, λ is the X-ray wavelength, β is the line broadening at half the maximum intensity (FWHM) in radians, θ_B is the Bragg angle and d_{gs} is the grain size. This method is used to measure through the complete film and is complementary to AFM which is used to measure the surface size of the grains. It is hard to define the shape factor for these NCD films since the seeds grow as inverted pyramids [115] although in many cases a value of 0.9 is a good approximation [116]. To estimate the FWHM for solving the Scherrer equation, a pseudo-Voigt function fit [117] is used and the instrumental broadening is taken into account. The most intense (111) crystal plane is used since there is almost no preferential crystal orientation for thin NCD layers. FIG. 6.5 shows the number of counts as a function of two times the angle between the incoming X-ray bundle and the sample surface (2θ) together with the pseudo-Voigt function fit to estimate β (0.158 ± 0.003 rad). With decreasing C/H-ratio, the grains are estimated to be ≈ 50 to ≈ 70 nm in diameter (TAB. 6.1) neglecting possible strain in the layers which can give additional broadening. In literature, AFM and STM measurements on thin B:NCD layers [92, 118] give a grain size about twice the value of the XRD values obtained here. This is an acceptable difference since the largest part of the inversed pyramid is present at the surface. A combination of modeling and experimental data gives a formula describing the influence of the C/H-ratio on the maximum grain size in nm [47]

$$d_{gs} = \{2.25 + 0.67exp(3430/T_s)\}\{[H]/[\Sigma CH_x]\} \tag{6.4}$$

where T_s is the substrate temperature in Kelvin, $[H]$ the concentration of atomic hydrogen and $[\Sigma CH_x]$ the concentration of the hydrocarbon radicals ($x < 4$). We can assume that $[H]$ is constant compared to $[\Sigma CH_x]$ for all C/H-ratios used in this work. Since the plasma during the CVD has an abundance of $[H]$ which reacts with the methane, $[\Sigma CH_x]$ decreases linearly when decreasing the C/H-ratio linearly. Also supposing that the latter equation is qualitatively usable for thin NCD films where the grains are not yet fully grown, equation (6.4) can be written as:

$$\frac{1}{d_{gs}} = a[C/H] + b. \tag{6.5}$$

FIG. 6.6 supports this last relation using the grain sizes derived from XRD spectra.

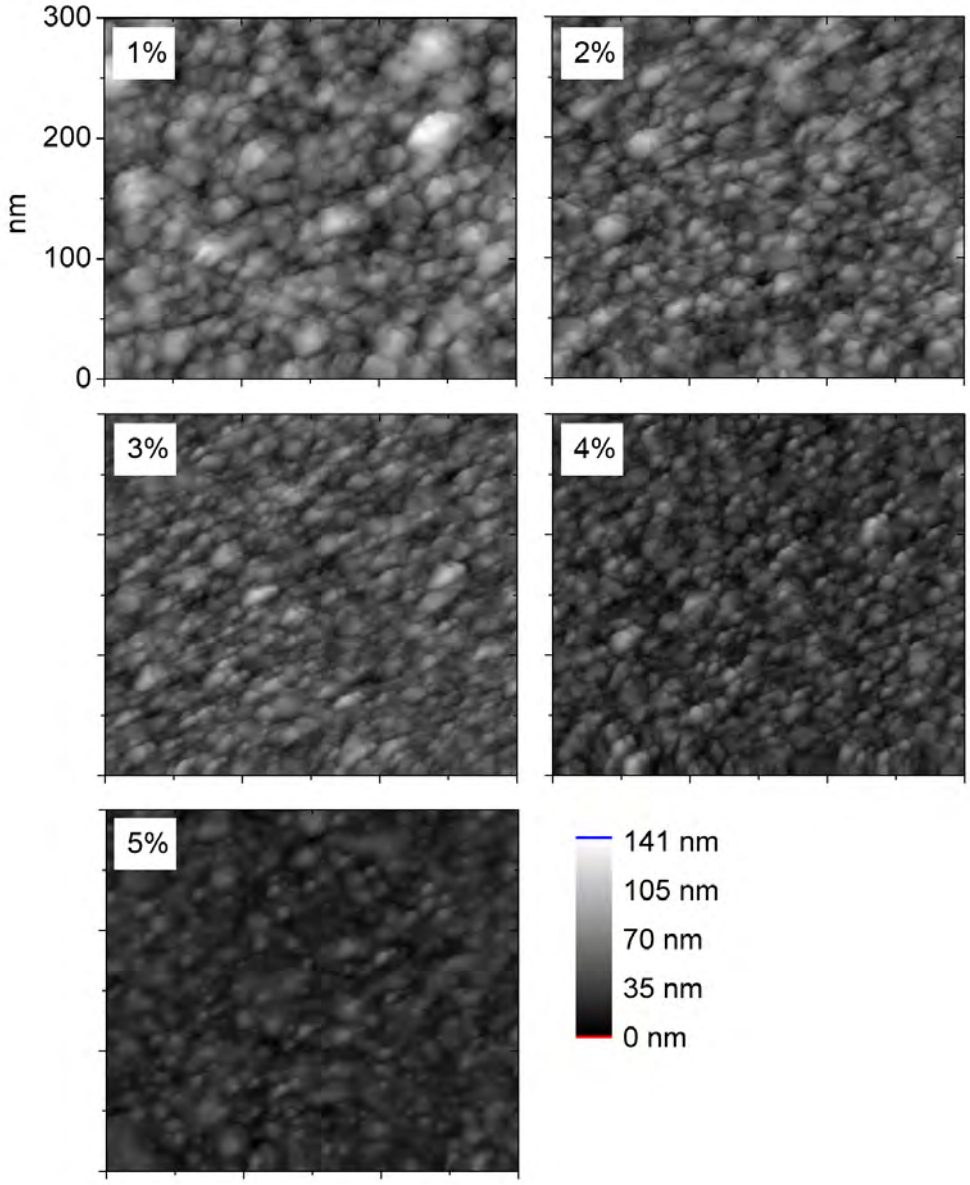

Figure 6.3: AFM images of the 1%, 2%, 3%, 4% and 5% samples. A smooth decrease in grain size and roughness from the 1% to the 5% sample is observable.

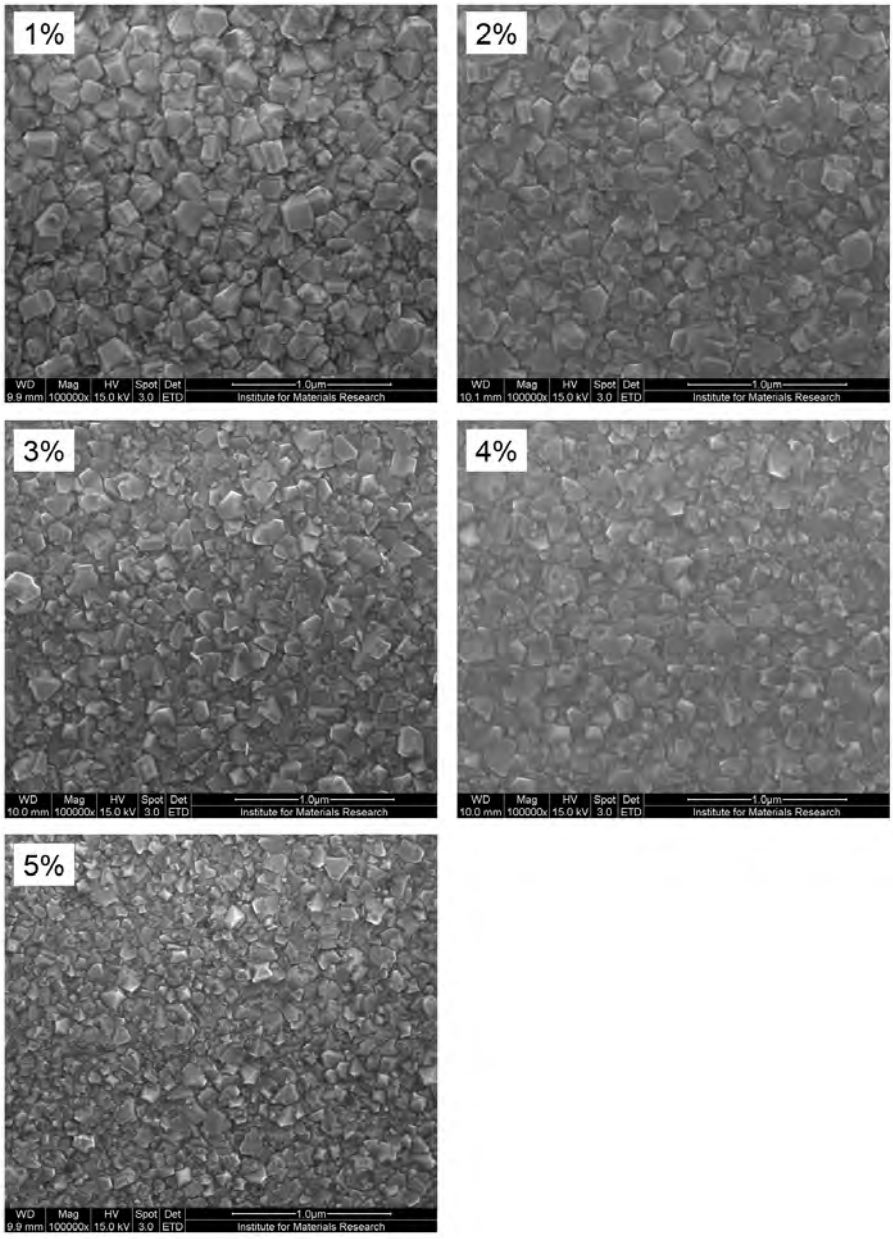

Figure 6.4: SEM images of the 1%, 2%, 3%, 4% and 5% samples. A smooth decrease in grain size from the 1% to the 5% sample like in the AFM images is observable.

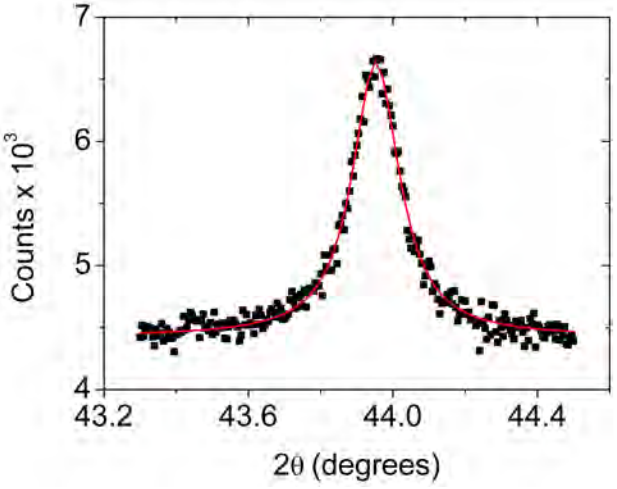

Figure 6.5: The XRD spectrum around the (111) crystal plane for the 1% sample together with the pseudo-Voigt function fit.

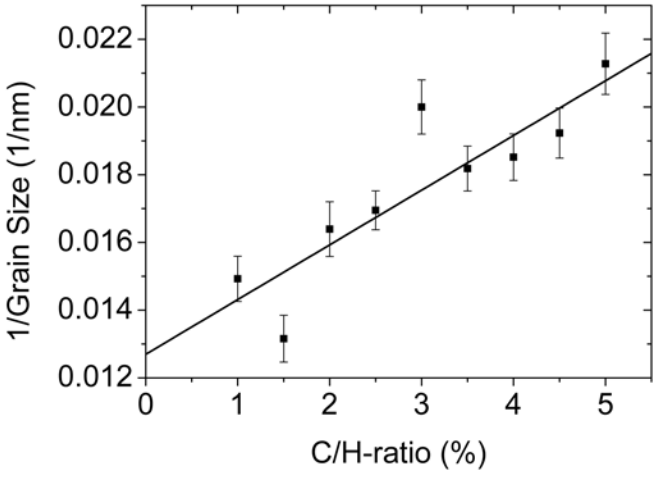

Figure 6.6: Relation between the average grain size of the thin B:NCD layers derived from XRD measurements and the C/H-ratio during the growth of the layers.

6.3.2 Electronic properties

In heavily boron-doped single crystal diamonds, the change in resistivity as a function of temperature ($\partial\rho/\partial T$) is small on the metallic side of the metal-insulator transition [119, 120, 121]. For a grain boundary which can be represented as a potential barrier for charge carriers, $\partial\rho/\partial T$ is negative due to thermal activation [92, 122]. This means that more charges will pass the grain boundaries as they gain energy by increasing the temperature. Within the investigated temperature range, we assume that a grain boundary has a higher resistivity than a heavily boron-doped diamond grain, which effectively is and behaves as a single crystal. First, we can see in FIG. 6.7 that the resistivity for the samples investigated in this work decreases with a decreasing C/H-ratio. Second, $|\partial\rho/\partial T|$ decreases also with a decreasing C/H-ratio. The 1% sample, with the lowest resistivity and the lowest $|\partial\rho/\partial T|$, has resistivity properties closer to those of a heavily boron-doped single crystal diamond than the 5% sample [119]. The 5% sample, with smaller grain size and thus more grain boundaries, shows the highest resistivity and the highest $|\partial\rho/\partial T|$, and thus shows resistivity properties closer to that of a grain boundary than the 1% sample. If the grains are assumed to have the same resistivity, we can conclude that a higher grain boundary density increases the resistivity and the temperature dependence of the resistivity. This fits with the properties of the grain boundaries earlier described. We believe that the decrease in grain boundary density, related to the decrease in C/H-ratio, is the factor with the largest influence on the resistivity. To confirm the increased temperature dependence of the resistivity, the resistivity of all samples is fitted using an exponential dependence with $1/T$ to calculate the experimental activation energies (E_a). TAB. 6.2 summarizes the values for calculations in the $300-400$ K range and a clear increase as a function of the C/H-ratio is observed. This is direct evidence that a higher grain boundary density, related to an increased C/H-ratio, increases E_a which was already proposed in literature and now strongly confirmed [92, 122]. The activation energy of the 0.5% sample was additionally measured to prove that E_a goes to zero for the C/H-ratio extrapolated to 0%.

Resistivity

Although heavily boron-doped nanocrystalline diamond films have a complex electronic behavior, a logarithmic relation between the conductivity and the temperature is observed at lower temperatures. This can be related to a theoretical model for granular systems [123]. However, at higher temperatures the behavior cannot be described in a satisfactory manner by the currently available theoretical models summarised by Beloborodov et alii [124]. Therefore, empirical equations following Matthiessen's rule, are derived in the following part. FIG. 6.8(a) shows linear fits of the resistivity as a function of the C/H-ratio and as becomes clear the intercepts of those linear fits have approximately the same value. Now, one can construct the following equation

$$\rho = \rho_{[C/H]=0} + \rho_{[C/H],T} \tag{6.6}$$

where $\rho_{[C/H]=0}$ represents the approximately temperature independent resistivity of a hypothetical sample grown with no methane. In the light of the results discussed before, such a sample would correspond to a single grain without grain boundaries

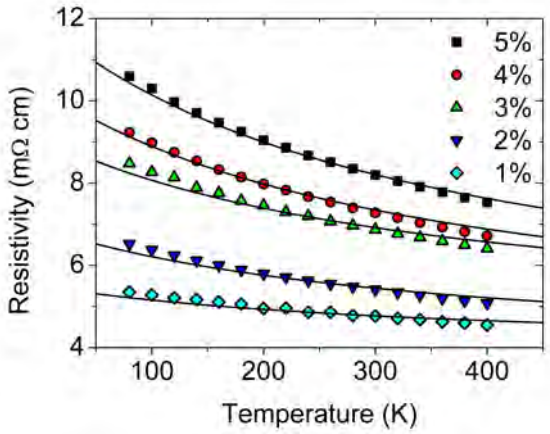

Figure 6.7: Resistivity as a function of temperature for different C/H-ratios. The black lines represent the fittings using equation (6.7) with $\rho_{[C/H]=0}$ as the only fitting parameter.

present. The temperature and the C/H-ratio dependence are represented by $\rho_{[C/H],T}$. When the inverse of the slopes in FIG. 6.8(a) ($1/S(T)$) are plotted as a function of temperature, an unexpected linear relation appears (FIG. 6.8(b)). Now, $\rho_{[C/H],T}$ can be replaced in equation (6.6) which gives:

$$\rho = \rho_{[C/H]=0} + \frac{[C/H]}{a + bT}. \tag{6.7}$$

Equation (6.7) is used to fit the temperature dependence of the resistivity in FIG. 6.7 with $\rho_{[C/H]=0}$ as the only fitting parameter. A similar fit function was recently applied successfully to the temperature-dependent resistivity of ultra-thin graphite flakes [125]. The values of a and b are derived from the linear fit of FIG. 6.8(b) and the value of $\rho_{[C/H]=0}$ is derived from the intercept of FIG. 6.8(a) ($\approx$ 4 mΩ cm). At high temperature, the resistivity of the grain boundaries is reduced. For low C/H-ratios, the grain boundary density in the films is also reduced. So, for films grown with a low C/H-ratio and measured at high temperatures, $\rho_{[C/H]=0}$ becomes dominant. In addition, because the temperature dependence of $\rho_{[C/H]=0}$ is negligible [119], we can approximate that $\rho_{[C/H]=0}$ is the resistivity contribution of a heavily boron-doped single crystal diamond (ρ_{SC}) as earlier proposed. The second resistivity contribution ($\rho_{[C/H],T}$), has a strong temperature dependence and increases linearly with C/H-ratio. The grain boundary density also increases with the C/H-ratio and therefore, this second resistivity contribution can be seen as the contribution of the grain boundaries (ρ_{GB}) to the resistivity. Now, the total resistivity is the sum of two independent resistivity contributions and Matthiessen's rule is fulfilled:

$$\rho = \rho_{SC} + \rho_{GB}. \tag{6.8}$$

A theory, proposed by P. Sheng [126], where the contribution of the grain boundaries to the electronic conduction of some disordered materials is explained by a

fluctuation-induced mechanism should be kept in mind. At this moment, not enough specific information about the structure of NCD is known to test this theory.

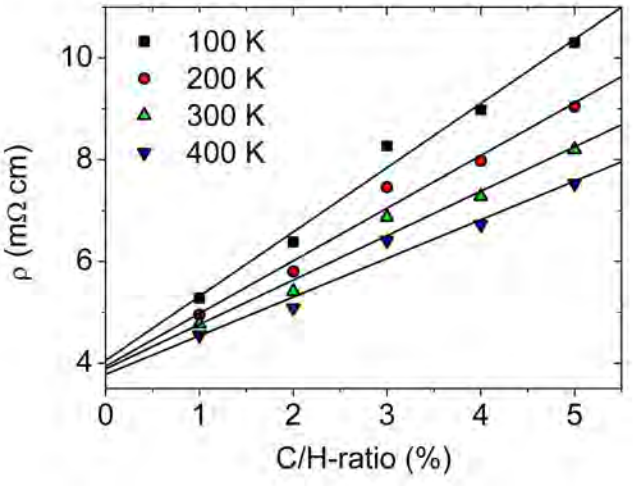

(a)

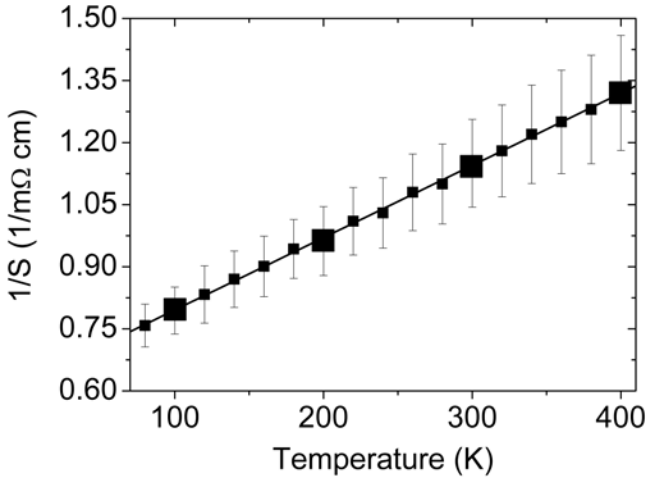

(b)

Figure 6.8: Panel (a) shows the resistivity as a function of the C/H-ratio measured at different temperatures. For sake of clarity, not all available data points obtained at other temperatures are plotted. The large data points on panel (b) are the inverse slope values of the linear fittings of the top panel, plotted as a function of temperature. The small data points are the inverse slope values of the linear fittings for the temperatures which are not shown on panel (a).

Mobility

Due to scattering at boron impurities, the hole mobility in a heavily boron-doped single crystal diamond is strongly reduced, compared to a lightly boron-doped single crystal diamond [90, 119]. Grain boundaries also reduce the mobility by scattering and this is clear in FIG. 6.9(a) where the mobility in the layers is strongly reduced as a function of the C/H-ratio. The mobilities in the investigated films are calculated with the assumption that no n-type carriers are present [85]. FIG. 6.9(a) also shows that the change in the charge carrier mobility as a function of temperature ($\partial\mu/\partial T$) is positive. Therefore, the hole mobility in all samples is thermally activated. When comparing the mobility values of the 1% and 5% samples, two observations can be made. First, the mobility of the former is comparable to that of a highly boron-doped single crystal diamond [119] (≈ 4 cm^2/Vs) but lower due to the contributions of grain boundaries. Second, as grain boundaries are more present in the 5% sample, the mobility shows a decrease with increasing C/H-ratio. For all temperatures, the inverse of the mobility is linear as function of the C/H-ratio (FIG. 6.9(b)) so the mobility can be expressed as

$$\frac{1}{\mu} = \frac{1}{\mu_{[C/H]=0}} + \frac{[C/H]}{C(T)} \tag{6.9}$$

where $1/\mu_{[C/H]=0}$ is approximated as a constant intercept in FIG. 6.9(b). Since $\mu_{[C/H]=0}$ approaches the value of boron-doped single crystal diamond [119] and is approximately temperature independent, it can be interpreted as the hole mobility in a heavily boron-doped single crystal diamond (μ_{SC}). $C(T)/[C/H]$ is the contribution of the grain boundaries to the hole mobility since $C(T)$, the inverse of the slopes in FIG. 6.9(b), increases with temperature due to the thermally activated grain boundaries. This means that there are less collisions of the holes with the grain boundaries at higher temperatures since the holes contain more energy to cross the potential barriers of the grains. Also a higher C/H-ratio makes the mobility go down since more holes will be scattered when the grain boundary density is higher. Again, Matthiessen's rule is fulfilled since the inverse of the mobility contribution of the grain boundaries is added to the inverse of the mobility in the diamond grains (heavily boron-doped diamond) giving the total inversed mobility presented in the following equation:

$$\frac{1}{\mu} = \frac{1}{\mu_{SC}} + \frac{1}{\mu_{GB}}. \tag{6.10}$$

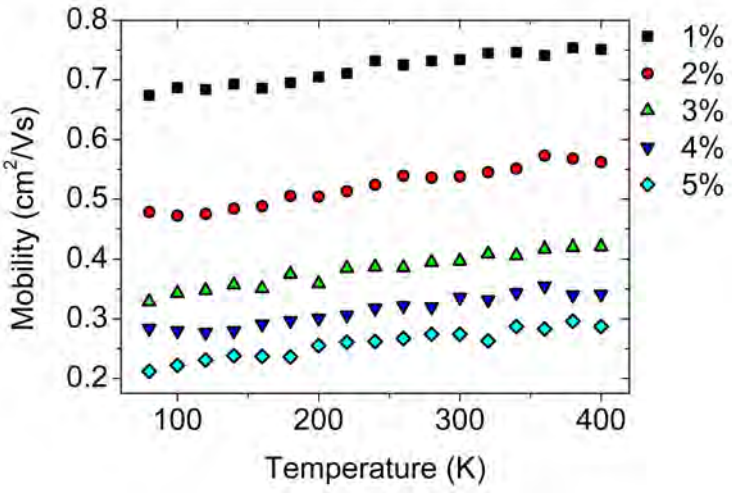

(a)

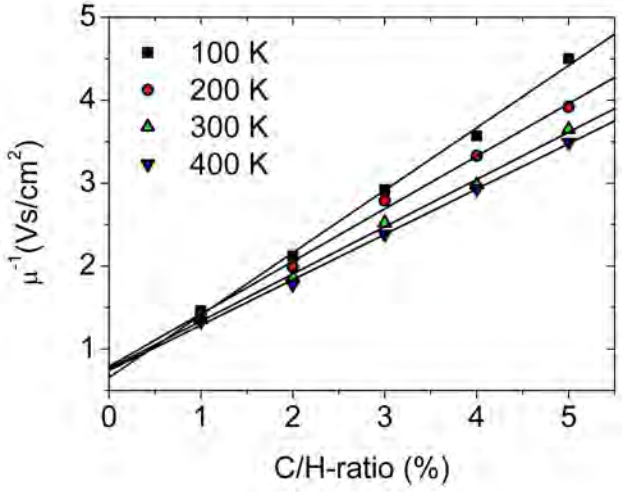

(b)

Figure 6.9: Panel (a) shows the mobility as a function of temperature for different C/H-ratios. All samples show a small increase in mobility as a function of temperature. Panel (b) shows the inverse mobility values as a function of the C/H-ratios measured at different temperatures.

Charge carriers

Active charge carrier concentrations for the B:NCD films (n_{Hall}) greater than 10^{21} cm^{-3} are derived from Hall effect measurements and total boron concentrations (n_{NDP}) are derived from neutron depth profiling (FIG. 6.10(a)). Charge carrier concentrations calculated from Hall effect measurements show a linear relation with C/H-ratio and the boron concentrations calculated from NDP show an increase with the C/H-ratio (FIG. 6.10(b)). At the highest measuring temperature, about $50 - 70\%$ of the boron atoms are active. For a higher C/H-ratio, more boron is incorporated actively into the diamond lattice, which was earlier observed in single crystal diamond [127]. The inactive incorporation of boron increases also and even more than the inactive incorporation. This could indicate that the inactive boron is going to the grain boundaries. At different growth conditions, 'cauliflower'-type nanocrystalline (c-NCD) and ultrananocrystalline (UNCD) CVD diamond films can be generated and the affinity of boron to the surface of the grains and to the grain boundaries becomes more important [25, 128]. Since the morphology of the latter films differ from the morphology of the films in this work, other transport mechanisms than suggested in this work are most probably occurring there.

Superconducting properties

FIG. 6.11 shows that the critical temperature (T_c) of the samples follow the total boron concentration measured by neutron depth profiling. The values are listed in TAB. 6.2. This means that an increased boron incorporation due to a higher C/H-ratio during growth, wins in terms of critical temperature from the smaller grains. The 1% sample is not perfectly aligned with the other samples. This can be addressed to several causes. The most probable cause is the fact that growing a very systematical series of samples is technically disfavored by background boron incorporation and by small changes in the behavior of the reactor. On FIG. 6.10(a) one can see that the 1% sample is also a little bit thicker and has a less homogeneous B-incorporation as a function of the depth, compared to the other samples. This less homogeneous growth is very clearly seen for the 0.5% sample in chapter 4 which can be addressed to orientation preference of the growth direction of the crystallites.

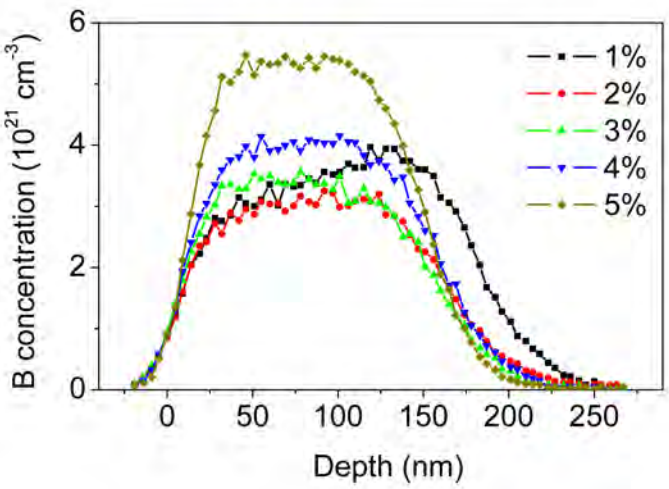

(a)

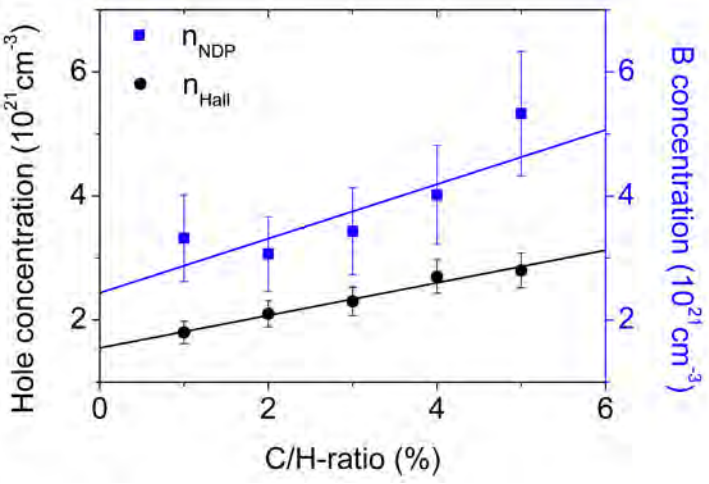

(b)

Figure 6.10: Panel (a) shows the neutron depth profiling spectrum of boron for the NCD layers. Panel (b) shows the total boron concentration (n_{NDP}) and the hole concentration (n_{Hall}) as a function of the C/H-ratio, listed in TAB. 6.2.

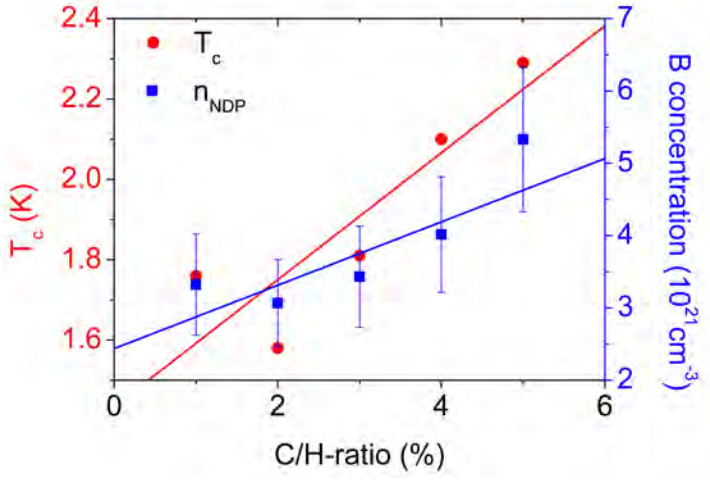

Figure 6.11: The total boron concentration (n_{NDP}) and the critical temperature for superconductivity (T_c) as a function of the C/H-ratio.

Table 6.2: Summary of the main electronic characteristics of the B:NCD films as a function of the C/H-ratio.The electronic properties, except for the experimental activation energy and the critical temperature, are presented for a temperature of 400 K.

C/H-ratio (%)	ρ (mΩ cm)	n_{Hall} (10^{21}cm^{-3})	n_{NDP} (10^{21}cm^{-3})	μ (cm^2/Vs)	E_a (meV)	T_c (K)
0.5	/	/	/	/	4.0	/
1	4.6	1.8	3.3	0.77	5.4	1.76
2	5.1	2.1	3.1	0.59	7.3	1.58
3	6.4	2.3	3.4	0.43	8.0	1.81
4	6.7	2.7	4.0	0.34	9.2	2.10
5	7.5	2.8	5.3	0.30	9.6	2.29

6.4 Conclusions

The results in this work confirm that a low C/H-ratio, during the growth of heavily boron-doped nanocrystalline diamond on the metallic side of the metal-insulator transition, leads to larger grains and a higher surface roughness than for a high C/H-ratio. Electronic transport measurements reveal a lower resistivity and a higher hole mobility for lower C/H-ratios. The difference in resistivity as a function of the temperature is less pronounced for lower C/H-ratios and the mobility is thermally activated. Since the grain boundary density is higher for films grown with high C/H-ratios, their electronic transport properties resemble more the electronic transport properties of grain boundaries. It is proposed in this work that grain boundaries are responsible for the differences in the electronic transport properties of the examined films. The contributions for the resistivity and mobility of the grain boundaries and the heavily boron-doped grains can be independently identified whereby Matthiessen's rule is followed. Novel empirical formulas are proposed which describes the resistivity and the mobility in a polycrystalline material as a function of the growth conditions. These growth conditions are related to the mean size of heavily doped grains. It is also proved for B:NCD that the boron-incorporation and the active charge carrier concentration increases significantly when the B/C-ratio is kept constant and the C/H-ratio is increased. Remarkable is the increase of the critical temperature when the grain size becomes smaller and the boron incorporation increases.

Chapter 7

Superconductivity in boron-doped diamond

The aim of this chapter is to give a brief overview about superconductivity in nanocrystalline diamond films. Especially the results obtained in the light of a co-operation with the Catholic University of Leuven (low temperature transport measurements) and Hasselt University (diamond growth) granted by FWO are presented.

7.1 Introduction

The discovery of superconductivity in heavily boron-doped diamond by Ekimov et al. in 2004 was on a polycrystalline diamond sample, prepared by a high pressure/high temperature process [129]. FIG. 7.1 shows a SEM image of this heavily boron-doped diamond sample and a graph of the electronic transport properties vs. temperature at different pressures. Later, superconductivity in diamond was confirmed for heavily boron-doped polycrystalline [130] and single crystalline [131] diamond films, grown by CVD. Wang et al. [132] recorded one of the highest critical temperatures ($\approx$ 10 K) on a thick polycrystalline film, grown by hot-filament chemical vapor deposition. The highest T_c ($\approx$ 11.4 K) is recorded by Takano et al. on a (111) oriented homoepitaxial diamond [4]. Here, the heavily boron-doped layer was grown with MWPECVD on a HPHT diamond. One has to take into account that in the latter references, the T_c is defined as the temperature at the onset of superconductivity. The onset of superconductivity is at the point where one can see a deviation of resistance from the 'normal' resistance of a sample due to a phase transition to the superconducting phase. Boron-doped nanocrystalline diamond films are also superconducting but at lower offset temperatures than for microcrystalline or single crystal diamond with the same boron content [118, 123, 133, 134]. An offset temperature is the temperature where the resistance of a sample is unmeasurable small. Due to the polycrystalline character of the B:NCD films, the transition form onset to offset temperature is wide. Sample 5% of chapter 6 even has an onset temperature of 10.8 K but needs to be cooled down to 1.8 K to reach the offset temperature.
Most experimental [135, 136, 137, 138, 139] and theoretical work [140, 141, 142,

143, 144] suggest a standard Bardeen Cooper and Schrieffer (BCS) model involving a phonon-mediated pairing mechanism [145]. Bustarret et al. [131] also showed that homoepitaxial diamond layers doped with boron in the $10^{20} - 10^{21}\text{cm}^{-3}$ range are type II superconductors with sharp transitions (0.2 K).

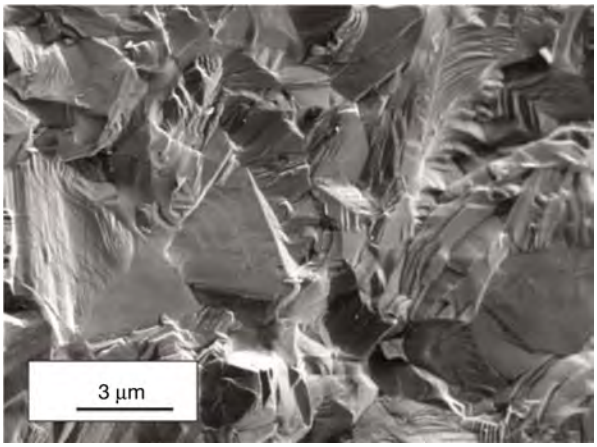

(a)

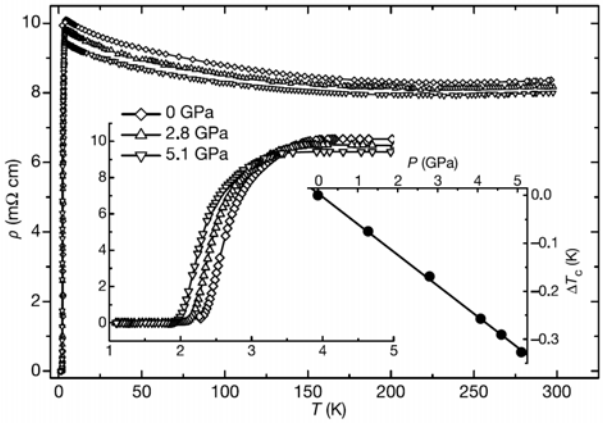

(b)

Figure 7.1: Panel (a) shows a SEM image of superconducting microcrystalline diamond and panel (b) shows the resistance as a function of temperature and pressure. These figures are obtained from the work of Ekimov et alii [129].

7.2 Intrinsic/extrinsic granularity in superconducting B:NCD

A series of B:NCD samples with critical offset temperatures under 3 K were prepared with MWPECVD on electronically insulating fused silica substrates. The electronic transport properties of these B:NCD samples show pronounced granular effects and it turns out that this granularity is both intrinsic as well as extrinsic. In using scanning tunneling microscopy/spectroscopy techniques to measure the intrinsic granularity, meaning that within physical grains, a strong intragrain modulation of the order parameter is measured. As a consequence of these granularities, the transport properties show evidence of (i) strong superconducting fluctuations and (ii) Cooper pair tunneling and/or quasiparticle tunneling. The latter effects explain the observed negative magnetoresistance.

7.2.1 Electronic transport properties

The electronic transport of films with varying boron concentrations are presented in FIG. 7.2. This figure shows the resistivity vs. the temperature in a log-log scale for a set of thin B:NCD films with a systematic increase of the B-doping (from a to e). The onset of a superconducting transition can be seen in samples d and e. The broadness of their transitions can be explained by modeling the film as an irregular distribution of Josephson junctions linking the superconducting grains/islands together. The $R(T)$ behavior shown in FIG. 7.2 is typical for granular films in which the superconductor-insulator transition (SIT) has been observed upon increasing the film thickness, i.e. by decreasing the number of grain boundaries [146, 147, 148]. The broad superconducting transition in samples (d) and (e) can be explained by inhomogeneous boron doping of the samples (resulting in a distribution of T_c values). Upon decreasing the temperature, first higher doped regions become superconducting opening non-percolating zero resistance channels. Further cooling down of the sample implies the appearance of a larger number of superconducting regions and a macroscopic zero resistance state is achieved once the Josephson coupling between them provides the percolating superconducting paths. TAB. 7.1 shows the onset, the middle and the offset critical temperatures of the samples in chapter 6. Here, one can clearly see that a decreased average grain size increases the superconducting transition even more. The 5% sample has the highest boron concentration which makes some grains become superconducting at higher temperatures than for the other samples. The macroscopic effect is an increase in onset temperature. Due to the increased grain boundary density in the 5% sample, more grains need to couple (Josephson coupling) to reach the offset temperature with the effect that the transition from onset to offset is broad. One can conclude that the transition becomes smaller when the grain boundary density decreases and the boron incorporation increases.

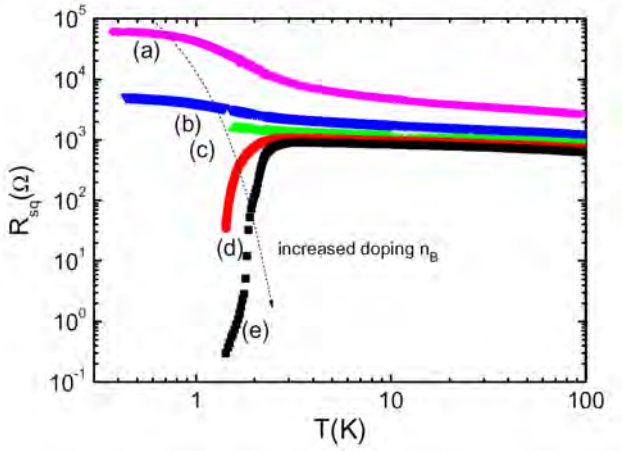

Figure 7.2: Resistance versus temperature for thin B:NCD films with a systematic change of the boron concentration

Table 7.1: The onset, middle and offset critical temperatures of the samples in chapter 6 as a function of growth conditions and grain size.

C/H-ratio (%)	Grain Size (nm)	T_c(onset) (K)	T_c(mid) (K)	T_c(offset) (K)	Transition (K)
1	67	7.0	1.76	1.35	5.6
2	61	6.77	1.58	1.25	5.52
3	50	7.66	1.81	1.41	6.25
4	54	9.30	2.10	1.66	7.64
5	47	10.8	2.29	1.84	8.96

7.2.2 Magnetotransport properties

In FIG. 7.3, a negative magnetoresistance (NMR) regime can be observed for sample (b) which does not show a global superconducting state in the measured temperature range. Achatz et al. also observed this behavior in a similar B:NCD sample and summarized possible theories for explaining this behavior [123]. Handling all these theories in detail goes beyond the scope of this work although the percolation theory, already used in the previous section, will be used to explain the observations.

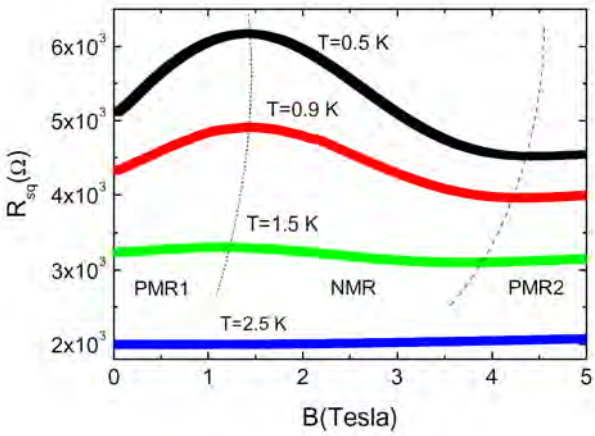

Figure 7.3: The magnetoresistance of sample (b) measured between 0.5 K and 2.5 K with a magnetic field orientation perpendicular to the surface of sample (b).

The magnetic field effect on the resistance is significant in both insulating samples (a) and (b) but the strongest effect is seen in sample (b) and therefore, in what follows, the discussion will be focused on sample (b). When switching on a magnetic field (B), the resistivity increases as a function of the magnetic field due to the decoupling between the grains. This is graphically presented in FIG. 7.4 when going from region I to region II. Since the boron concentration of sample (b) is larger than that of sample (a), sample (b) has a higher coupling density which can be broken by a magnetic field. This is macroscopically translated into a higher positive magnetoresistance (PMR1) for sample (b). This fits with the experiment which is discussed in more detail by Willems et al. [149]. The PMR (region PMR1) of sample (b) which is more pronounced at lower temperatures, can be observed on FIG. 7.3. When increasing the magnetic field even further, the Cooper pair transfer between grains vanishes, and transport occurs through single-quasiparticle tunneling. This is graphically shown in FIG. 7.4 when going from region II to region III. The density of states of the single-quasiparticles is reduced due to remaining Cooper pairs inside the grains. This makes the total tunneling current decrease, which results in an additional increase of the resistivity (still region PMR1). Hence, suppression of the superconducting fluctuations by further increasing the magnetic field is translated into a decrease of the resistance because the density of states of the single-quasiparticles now increases [124]. Although superconductivity is usually associated with a drop in resis-

tivity, this result shows that under certain conditions, the onset of superconductivity actually can increase the resistance of (granular) materials. The PMR2 (FIG. 7.3) at high fields is attributed to orbital shrinking effects which start to decouple the overlapped boron orbitals [149].

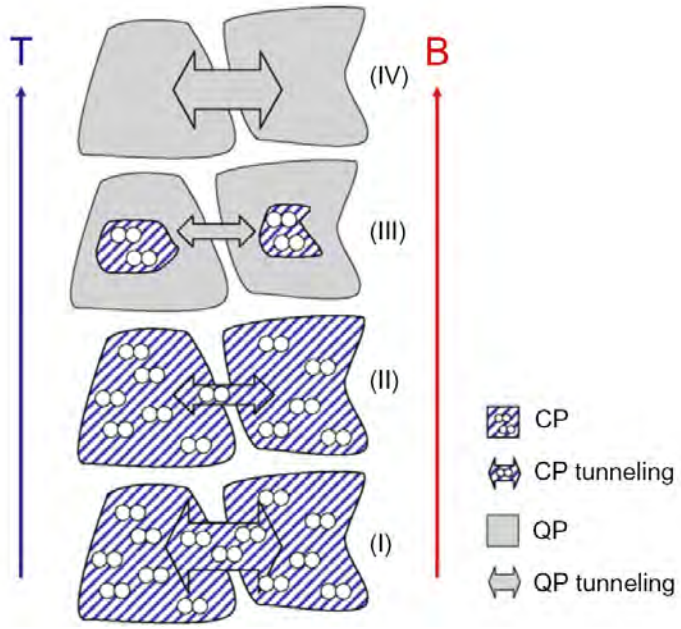

Figure 7.4: Schematic description of the coupling processes between the grains of superconducting B:NCD films. CP stands for Cooper pair and QP stands for single-quasiparticle.

7.2.3 Local study of superconductivity in B:NCD

Low temperature scanning tunneling microscopy and spectroscopy (STM/S) experiments are performed on a superconducting B:NCD film in order to compare the extrinsic versus the intrinsic granularity of this film. Although the morphology of the granularity can be easily observed via SEM, it is interesting to analyze how superconductivity inside the grains would be. To figure out this unknown, low temperature STM/S measurements are performed in Madrid (Laboratorio de Bajas Temperaturas, Departamento de Fisica de la Materia Condensada, Universidad Autonoma de Madrid, Spain) by I. Guillamon, H. Suderow and S. Vieira. A more detailed explanation can be found in a work of Willems et al. [118, 150]. The main results are shown in FIG. 7.5. (right panel) shows the STS map of an area 560 nm by 560 nm. Local spectroscopic characteristics were obtained by deriving the $I(V)$ dependencies which means that the conductivity (σ) was determined by changing the voltage of the STM/S tip with respect to the B:NCD layer while measuring the current:

$$\sigma(V) = \frac{dI}{dV}. \tag{7.1}$$

The dark spots with conductivity σ_D denote the normalized current σ_{norm} minus the background current $\sigma(0)$. The regions of superconductivity are highly inhomogeneous over the surface, even within a single grain. Cross-sectional analysis of the STS maps shows that the order parameter (Δ) changes typically over 30 nm, a considerable smaller length compared to the grain size. By taking the difference of the conductivity values of the upper and the lower dashed horizontal lines in the graph of FIG. 7.5, one approximates the magnitude of the order parameter at point (a). Doing this for the upper and the middle horizontal dashed lines, one approximates the size of the order parameter at point (b). The larger the value of this order parameter, the deeper the point where the order parameter was measured is in the superconducting state. The order parameter and the tunnel current are proportional to each other. The transition from the superconducting to the normal regions inside the grains is rather smooth, with no important changes in the noise of the data. The latter rules out surface contamination as causing the variation in Δ and constitutes a proof for the inhomogeneities as being intrinsic to the crystallite granules [151]. A possible cause for the change in Δ could be attributed to the inhomogeneous boron incorporation by the diamond grains [152]. The latter might affect the critical temperature locally since it varies with the boron incorporation. Other explanations, involving the particular band structure of boron-doped diamond cannot be excluded either. The order parameter can have a certain symmetry which makes conduction in certain directions of the crystal lattice more favorable. By performing STM/S on a spot, warming the sample up, cooling it down again, performing STM/S on the same spot and comparing the two measurements which are performed under identical conditions, should answer the change in Δ. When this is due to inhomogeneous boron incorporation, the two identical measurements should result in similar STS maps. When the change in Δ is not caused by inhomogeneous boron incorporation, the two identical measurements can result in dissimilar STS maps.

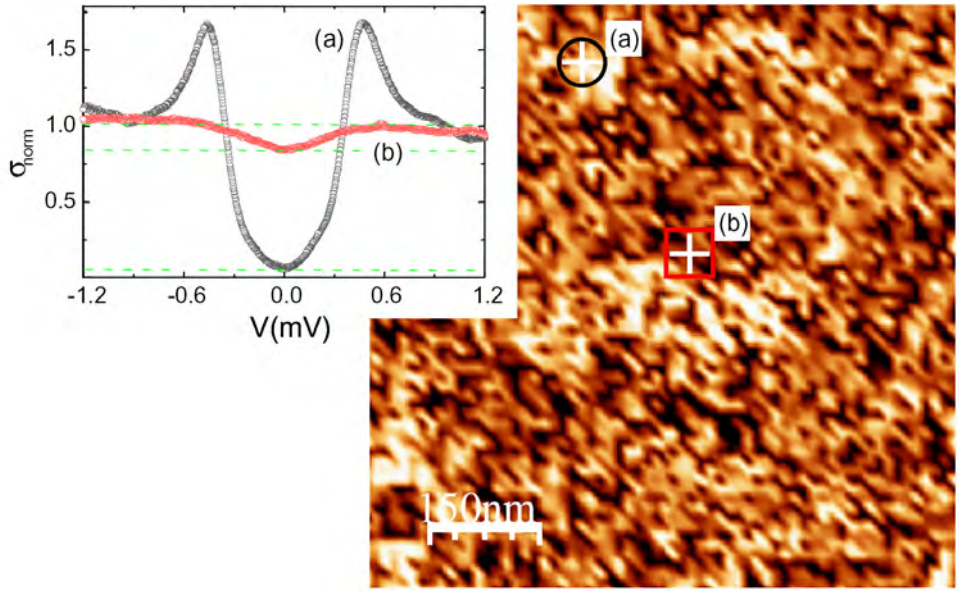

Figure 7.5: STS spectrum taken at 100 mK at position (a) and (b) within one particular grain (left panel). The right panel is the STS map of an area of 560 nm by 560 nm which shows a spatial gap distribution.

In order to perform STM/S measurements on isolated nanocrystalline grains, there are two main problems to tackle. The first problem is to grow isolated grains with a controlled surface density. Reaching a density of several grains per 1 μm^2 in a controlled way is optimal for STS/M measurements. The second problem is to have a substrate which is highly conductive at very low temperatures without becoming superconducting itself.
The first problem was tackled by diluting a detonation diamond seeding suspension. We started to make a suspension of 0.5 gams detonation diamond in 1 liter of DI water. A part of this suspension was diluted 10, 100, 1000 and 10000 times. Then, five 1 cm by 1 cm silicon substrates were seeded in one of the five seeding suspensions as described in the previous chapters. Growth was performed in ASTeX 2 with 7000 ppm B/C, 3% C/H-ratio, at 800°C for 20 minutes. SEM images of the as grown samples, presented in FIG. 7.6, show a clear decrease in grain density as a function of the degree of dilution of the seeding suspension. The sample which is 1000 times diluted shows the best grain density to investigate with STM/S. In order to solve the second problem, we need to repeat the latter experiment on a substrate which is highly conductive at very low temperatures without becoming superconducting itself.

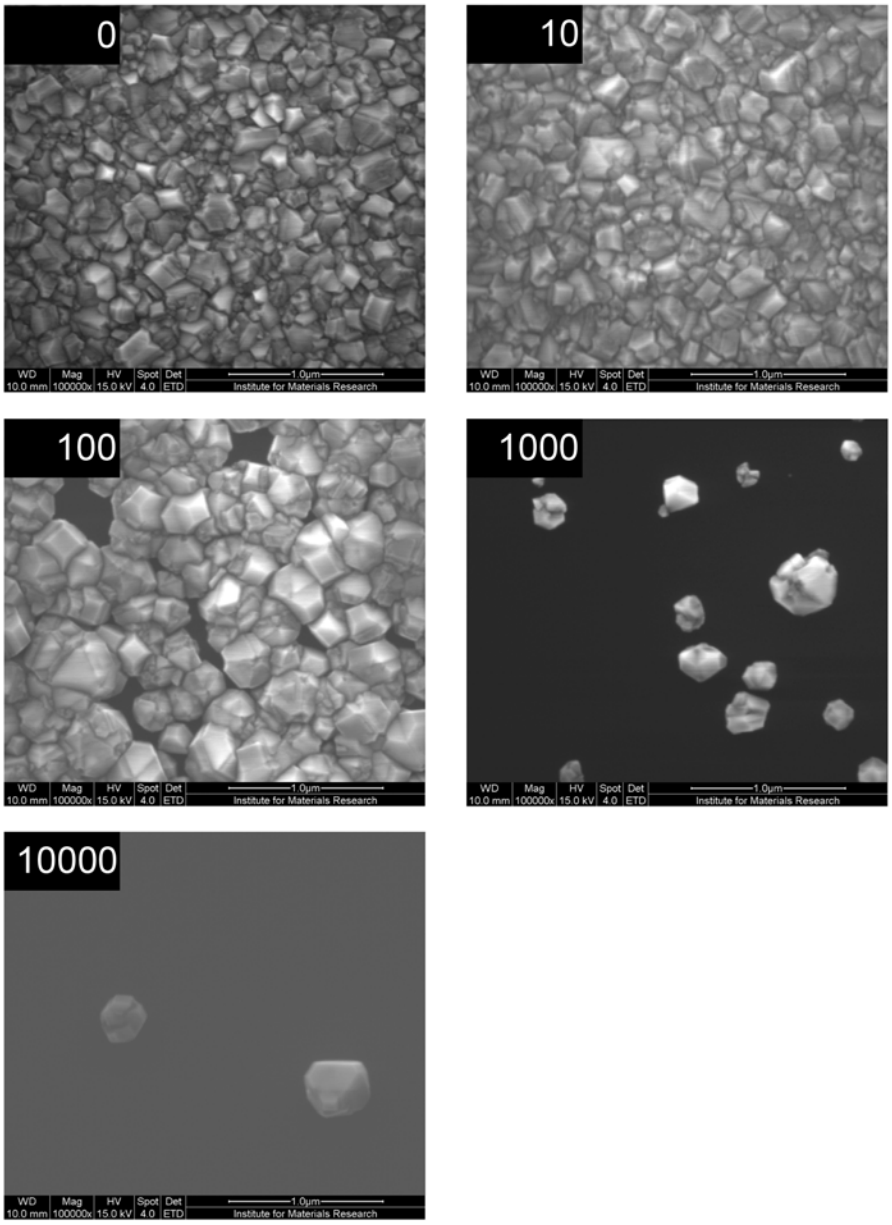

Figure 7.6: SEM images of the five substrates after growth, seeded with a 0, 10, 100, 1000 and 10000 times diluted seeding suspension of 0.5 grams/liter detonation diamond.

7.2.4 Conclusions

It is possible to grow heavily boron-doped single crystal, microcrystalline and nanocrystalline diamond with critical onset temperatures above 10 K. The amount of grain boundaries in the different types of diamond films influences the temperature difference (transition) from critical onset to critical offset temperature. This can be attributed to Josephson coupling between grains.

The magnetotransport properties of nanocrystalline diamond films differ strongly from single crystal diamond films due to decoupling and single-quasiparticle tunneling between grains. Superconductivity is usually associated with a drop in resistivity. Here, it is shown that under certain conditions superconductivity increases the resistivity of granular materials.

Local electronic transport measurements, performed by STM/S, show a highly irregular transport behavior over length scales smaller than the grain size of B:NCD. This can be attributed to inhomogeneous boron incorporation or the particular band structure of boron-doped diamond.

A straight forward way of controlling the seeding density is developed. Using this technique, it is possible to investigate nano-sized boron-doped diamond grains in future work.

Chapter 8

A biological application of B:NCD in DNA sensors

A substantial part of the time given for this thesis, consisted of tuning growth properties of (B:)NCD layers for biological sensor applications. Therefore, this last chapter is devoted to DNA characterization with B:NCD as a platform, published by collegue B. van Grinsven and coworkers [153].

8.1 Introduction

One of the central challenges in human genomics is the detection and identification of single-nucleotide polymorphisms. Here, a straightforward method to detect these polymorphisms is presented:

Electronic monitoring of DNA denaturation by NaOH using electrochemical impedance spectroscopy in combination with fluorescence imaging as a reference technique.

Probe DNA, consisting of a 36-mer fragment was covalently immobilized on B:NCD-diamond electrodes [154] and hybridized with four different types of 29-mer target DNA. First a complementary strand (with a fluorescent label), than single-nucleotide defects at two different positions and also a non-complementary random sequence. The mathematical separation of the impedimetric signals into the time constant for NaOH exposure and the intrinsic denaturation-time constants gives clear evidence that the denaturation times reflect the intrinsic stability of the DNA duplexes [155]. The sensor electrodes can be used repetitively. These elements suggest that the monitoring of chemically induced denaturation at room temperature is an interesting approach to measure DNA duplex stability as an alternative to thermal denaturation at elevated temperatures, used in DNA-melting experiments and single nucleotide polymorphism (SNP) analysis [156].

8.2 Experimental

FIG. 8.1 shows the schematic layout of the impedimetric flow cell. The working electrode which is made out of DNA on B:NCD with highly doped silicon as a substrate, can be monitored with the fluorescence microscope while a gold wire serves as a counter electrode. The liquids (1×PBS buffer and 0.1 M NaOH) are sequentially administered by a syringe-driven pump system connected to a 3-way valve. The temperature of the liquid (about 25°C) in the cell and of the copper back contact is measured by thermocouples (not shown). All connections to the impedance analyzer are done by mini-coax cables. To ensure a low electrical resistivity of the diamond

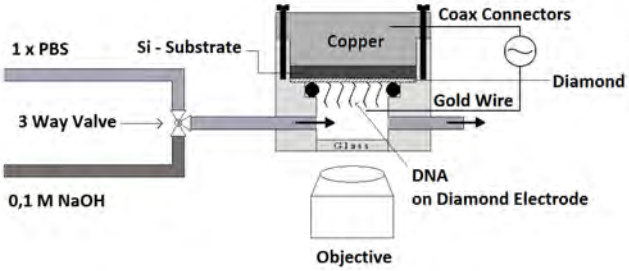

Figure 8.1: The impedimetric flow cell.

layer (in the order of 1 Ω cm), the CVD deposition was done with an admixture of TMB to methane with a concentration ratio of 200 ppm B/C. The as-prepared diamond electrodes were hydrogenated in a hydrogen plasma (50 Torr, 800°C, power 4000 W, duration of 1 minute) to facilitate the attachment of the fatty acid linker molecules which bind covelently to a DNA strand.

8.3 Results and discussion

FIG. 8.2 shows the impedance profile of the denaturation of full-match DNA on the B:NCD sample. At t = 0, 0.1 M NaOH enters the cell and replaces the 1×PBS buffer, causing a drop of the fluorescence intensity and the impedance. This emerges from the denaturation and the change of liquids, while the fluorescence drop stems from DNA denaturation only. The extraction of the time constants τ_1 (denaturation) and τ_2 (exchange of fluids) is based on the Fits 1 and 2, as described by:

$$Z(t) = Z(t=\infty) + A_1 exp\left(-\frac{t}{\tau_1}\right) + A_2 exp\left(-\frac{t}{\tau_2}\right) \tag{8.1}$$

$$Z(t) = Z(t=\infty) + A_2 exp\left(-\frac{t}{\tau_2}\right). \tag{8.2}$$

A double-exponential fit according to EQ. 8.1 for superimposed, independent decay processes is known e.g., from the decomposition of biomass (tomato leaves) and the mass loss of tomato DNA as a function of time [155]. The parameter A_1 represents the denaturation-related decay amplitude and τ_1 the associated time constant; the

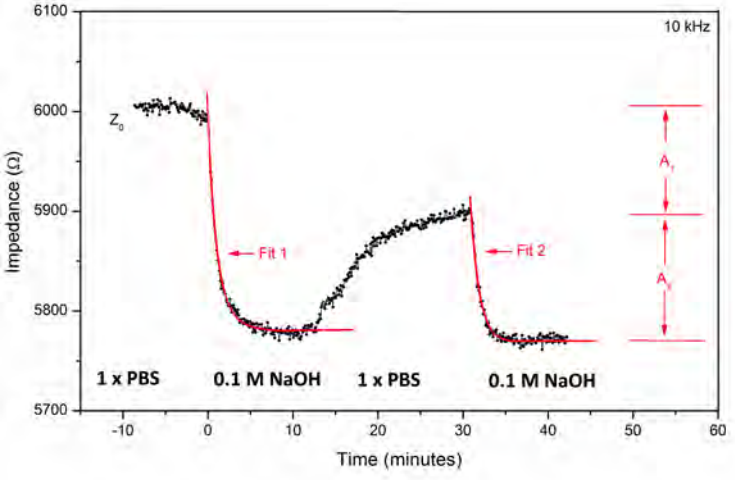

Figure 8.2: The impedance profile of the denaturation of full-match DNA on the B:NCD sample.

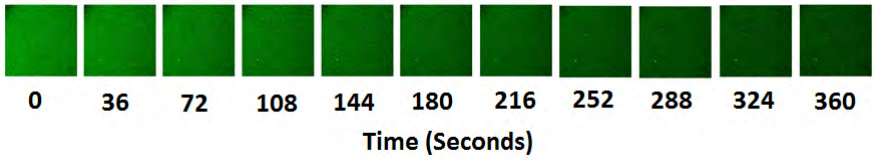

Figure 8.3: Series of confocal fluorescence images of the diamond electrode during the denaturation of complementary DNA at selected times.

amplitude A_2 refers to the impedance drop by the medium exchange and τ_2 is the corresponding time constant. The fit according to EQ. 8.2 describes solely the influence of the medium exchange from 1×PBS to 0.1M NaOH after the denaturation has taken place and is therefore representative for the medium exchange as such. The first time constant, derived from the impedimetric data (τ_1) is 2.24 ± 0.14 min. To determine τ_2 = 0.97 ± 0.06 min, the cell was refilled with 1×PBS buffer at t_1 = 12 min and flushed with 0.1 M NaOH at t_2 = 30 min. The amplitudes A_1 and A_2 indicate the respective influence of denaturation and liquids exchange on the impedance changes. First EQ. 8.2 was fitted to determine τ_2 and A_2. These values were than used to fit EQ. 8.1 for obtaining the values of τ_1 and A_1. To cross-check the electronically determined τ_1, time-lapse fluorescence imaging was performed during the denaturation step and the intensity $I(t)$ was averaged over an area of 900 by 900 mm^2. Selected images with intervals of 36 seconds, taken during the first 6 minutes of the dynamic imaging, are shown in FIG. 8.3. The area-averaged intensity values are described with the fit according to EQ. 8.3:

$$I(t) = I_0 + I_{DNA} exp\left(-\frac{t}{\tau_3}\right). \tag{8.3}$$

I_{DNA} is the intensity of the luminescence of the complementary strand and I_0 is the remnant background intensity. The fluorimetric result for the denaturation-related time constant τ_3 = 2.4 min, is within the error margins, perfectly consistent with the electronically determined τ_1. The determination of τ_3 is insensitive to the medium composition and truly reflects the progressing denaturation at the B:NCD surface. In conclusion, the electronically determined denaturation time constant τ_1 is a reliable measure for the duration of the chemically induced denaturation process.

FIG. 8.4 gives an overview of the denaturation steps performed on B:NCD with complementary target DNA(a), with a mismatch at base pair 20 (b), a mismatch at base pair 7(c), and a random target sequence (d). All data described as *chemical denaturation* are normalized to the impedance value at the moment when 0.1 M NaOH enters the cell and fitted with the double exponential EQ. 8.1 (Fit 1) as described before. The curves denoted as *medium exchange* refer to the second replacement of 1×PBS by 0.1 M NaOH after the actual denaturation step. These data are normalized with respect to the equilibrium impedance value at the time t_2 obtained after refilling the cell with 1×PBS buffer (Fit 2 according to EQ. 8.2). TAB. 8.1 summarizes the obtained values. It is clear that the thermodynamically most stable system is the hybridized DNA system with the complementary DNA strand. All other systems have τ_1 values which are significantly much lower. The τ_2 values are all the same which reflects the repeatability of the measurement.

Table 8.1: Summary of τ_1 and τ_2 values for different types of target DNA.

target DNA	τ_1 (minutes)	τ_2 (minutes)
Complementary	2.3 ± 0.1	0.52 ± 0.08
Mismatch BP20	1.38 ± 0.05	0.50 ± 0.09
Mismatch BP7	1.16 ± 0.04	0.46 ± 0.06
Random	0.59 ± 0.08	0.46 ± 0.04

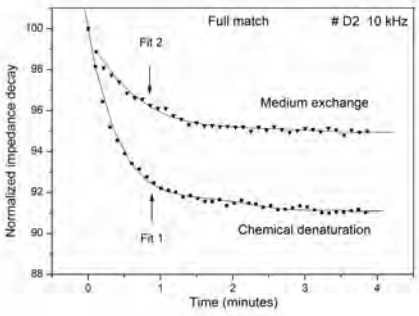

(a)

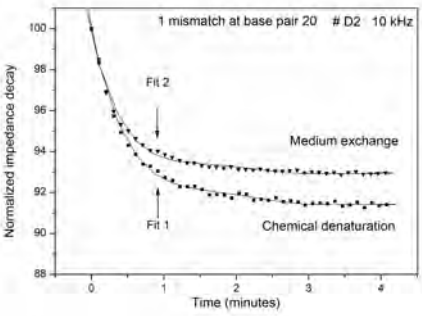

(b)

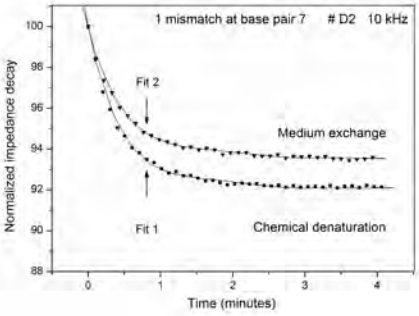

(c)

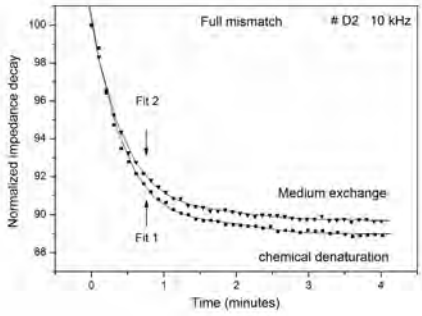

(d)

Figure 8.4: The denaturation steps performed on B:NCD with complementary target DNA(a), mismatch at base pair 20 (b), mismatch at base pair 7(c), and the random target sequence (d).

8.4 Conclusion

Impedance spectroscopy performed on diamond-based sensor electrodes, to monitor the kinetics of chemically induced DNA denaturation in real-time was done. The probe DNA was covalently bonded onto the electrodes and for four different types of target DNA (complementary, random, single mismatches at two different positions), denaturation time constants were measured. All time constants are at the scale of minutes while the denaturation takes the longest for complementary DNA duplexes. In addition, the method is intrinsically label-free (note that labels were only used to allow for fluorescence imaging as a reference technique) and as-prepared electrodes can be used repetitively, thanks to the strong covalent link between probe DNA and the diamond platform and the chemical inertness of diamond as such. Finally, the proposed method has the potential to be downsized and parallelized towards a microarraylike format as illustrated by the diamond-based microelectrode arrays with spot sizes of just 50 μm as described by Bonnauron and coworkers [157].

Bibliography

[1] C. Kittel, Introduction to Solid State Physics (John Wiley & Sons, New York, 1996).

[2] J. L. Davidson, Synthetic Diamond: Emerging CVD Science and Technology (Wiley-Interscience, New York, 1994).

[3] E. Bustarret, C. Marcenat, P. Achatz, J. Kacmarcik, F. Levy, A. Huxley, L. Ortega, E. Bourgeois, X. Blase, D. Debarre, and J. Boulmer, Nature **444**, 465 (2006).

[4] Y. Takano, T. Takenouchi, S. Ishii, S. Ueda, T. Okutsu, I. Sakaguchi, H. Umezawa, H. Kawarada, and M. Tachiki, Diamond Relat. Mater. **16**, 911 (2007).

[5] J. Isberg, J. Hammersberg, E. Johansson, T. Wikstrom, D. J. Twitchen, A. J. Whitehead, S. E. Coe, and G. A. Scarsbrook, Science **297**, 1670 (2002).

[6] R. Robertson, J. J. Fox, and A. E. Martin, Phil. Trans. R. Soc. London A **232**, 463 (1934).

[7] J. E. Field, The Properties of Natural and Synthetic Diamond (Academic Press, London, 1992).

[8] H. B. Dyer, F. A. Raal, L. Dupreez, and J. H. N. Loubser, Philos. Mag. **11**, 763 (1965).

[9] A. M. Zaitsev, Optical Properties of Diamond: a Data Handbook (Springer-Verlag, Berlin, 2001).

[10] M. R. Brozel, T. Evans, and R. F. Stephenson, Proc. R. Soc. London, Ser. A **361**, 107 (1978).

[11] O. D. Tucker, M. E. Newton, and J. M. Baker, Phys. Rev. B **50**, 15586 (1994).

[12] S. R. Boyd, I. Kiflawi, and G. S. Woods, Philos. Mag. B **69**, 1149 (1994).

[13] A. T. Collins, Diamond Relat. Mater. **8**, 1455 (1999).

[14] I. Kiflawi, J. Bruley, W. Luyten, and G. V. Tendeloo, Philos. Mag. B **78**, 299 (1998).

[15] W. V. Smith, P. P. Sorokin, I. L. Gelles, and G. J. Lasher, Phys. Rev. **115**, 1546 (1959).

[16] K. Iakoubovskii and G. J. Adriaenssens, J. Phys.: Condens. Matter **12**, L77 (2000).

[17] Nassau and Kurt, Gems made by man (Gemological Institute of America, Santa Monica, Calif, 1980).

[18] R. Louden, Adv. Phys. **13**, 423 (1964).

[19] M. O'Donoghue, Synthetic, imitation, and treated gemstones (Butterworth-Heinemann, Boston, 1997).

[20] A. T. Collins, Phil. Trans. R. Soc. London A **342**, 233 (1993).

[21] O. A. Williams, A. Kriele, J. Hees, M. Wolfer, W. Muller-Sebert, and C. E. Nebel, Chem. Phys. Lett. **495**, 84 (2010).

[22] S. Buhlmann, E. Blank, R. Haubner, and B. Lux, Diamond Relat. Mater. **8**, 194 (1999).

[23] A. C. Ferrari and J. Robertson, Phil. Trans. R. Soc. London A **362**, 2477 (2004).

[24] S. Prawer and R. J. Nemanich, Phil. Trans. R. Soc. London A **362**, 2537 (2004).

[25] P. W. May, W. J. Ludlow, M. Hannaway, P. J. Heard, J. A. Smith, and K. N. Rosser, Diamond Relat. Mater. **17**, 105 (2008).

[26] O. A. Williams, M. Daenen, J. D'Haen, K. Haenen, J. Maes, V. V. Moshchalkov, M. Nesladek, and D. M. Gruen, Diamond Relat. Mater. **15**, 654 (2006).

[27] C. Wild, N. Herres, and P. Koidl, J. Appl. Phys. **68**, 973 (1990).

[28] D. M. Gruen, MRS Bulletin **26**, 771 (2001).

[29] F. P. Bundy, H. T. Hall, H. M. Strong, and R. H. Wentorf, Nature **176**, 51 (1955).

[30] F. P. Bundy, W. A. Bassett, M. S. Weathers, R. J. Hemley, H. K. Mao, and A. Goncharov, Carbon **34**, 141 (1996).

[31] F. P. Bundy, J. Geophys. Res. **85**, 6930 (1980).

[32] E. Erlich and W. D. Hausel, Diamond deposits: Origin Exploration, and history of discovery (Littleton, CO : Society for Mining, Metallurgy, and Exploration, 2002).

[33] R. J. Wedlake, The Properties of Diamond (Academic Press, London, 1979).

[34] P. W. May, Phil. Trans. R. Soc. A **358**, 473 (2000).

[35] I. I. Kulakova, Phys. Solid State **46**, 636 (2004).

[36] V. V. Danilenko, Phys. Solid State **46**, 595 (2004).

[37] O. A. Shenderova, V. V. Zhirnov, and D. W. Brenner, Crit. Rev. Solid State Mater. Sci. **27**, 227 (2002).

[38] E. Osawa, Diamond Relat. Mater. **16**, 2018 (2007).

[39] O. A. Williams, O. Douheret, M. Daenen, K. Haenen, E. Osawa, and M. Takahashi, Chem. Phys. Lett. **445**, 255 (2007).

[40] K. Iakoubovskii, K. Mitsuishi, and K. Furuya, Nanotechnology **19**, 155705 (2008).

[41] W. G. Eversole, Synthesis of diamond, numbers 3030187 and 3030188, 1962.

[42] B. V. Derjaguin, D. V. Fedoseev, V. M. Lukyanovich, B. V. Spitsyn, A. V. Ryanov, and A. V. Lavrentyev, J. Cryst. Growth **2**, 380 (1968).

[43] F. G. Celii and J. E. Butler, A. Rev. phys. Chem. **42**, 643 (1991).

[44] K. Tsugawa, M. Ishihara, J. Kim, Y. Koga, and M. Hasegawa, Phys. Rev. B(12) (2010).

[45] P. K. Bachmann, D. Leers, and H. Lydtin, Diamond Relat. Mater. **1**, 1 (1991).

[46] J. E. Butler and R. L. Woodin, Phil. Trans. R. Soc. A **342**, 209 (1993).

[47] P. W. May, M. N. R. Ashfold, and Y. A. Mankelevich, J. Appl. Phys. **101**, 053115 (2007).

[48] M. Eckert, E. Neyts, and A. Bogaerts, J. Phys. D: Appl. Phys. **41**, 032006 (2008).

[49] J. E. Butler, Y. A. Mankelevich, A. Cheesman, J. Ma, and M. N. R. Ashfold, J. Phys.: Condens. Matter **21**, 364201 (2009).

[50] W. S. Yang and J. H. Je, J. Mater. Res. **11**, 1787 (1996).

[51] K. Ohtsuka, K. Suzuki, A. Sawabe, and T. Inuzuka, Japanese Journal of Applied Physics Part 2-Letters **35**, L1072 (1996).

[52] M. A. Prelas, G. Popovici, and L. K. Bigelow, Handbook of Industrial Diamonds and Diamond Films (Marcel Dekker, New York, 1998).

[53] P. A. Dennig and D. A. Stevenson, Appl. Phys. Lett. **59**, 1562 (1991).

[54] P. Ascarelli and S. Fontana, Appl. Surf. Sci. **64**, 307 (1993).

[55] S. Iijima, Y. Aikawa, and K. Baba, Appl. Phys. Lett. **57**, 2646 (1990).

[56] R. Akhvlediani, I. Lior, S. Michaelson, and A. Hoffman, Diamond Relat. Mater. **11**, 545 (2002).

[57] S. Yugo, T. Kimura, and T. Muto, Vacuum **41**, 1364 (1990).

[58] J. Robertson, Diamond Relat. Mater. **4**, 549 (1995).

[59] Y. Lifshitz, T. Kohler, T. Frauenheim, I. Guzmann, A. Hoffman, R. Q. Zhang, X. T. Zhou, and S. T. Lee, Science **297**, 1531 (2002).

[60] O. A. Williams, J. Hees, C. Dieker, W. Jager, L. Kirste, and C. E. Nebel, ACS Nano **4**, 4824 (2010).

[61] T. Young, Philos. Trans. Soc. London **95**, 65 (1805).

[62] A. Dupre and P. Dupre, Theorie Mechanique de le Chaleur (Gauthier-Villars, Paris, 1869).

[63] D. Berthelot, Compt. Rendus **126**, 1857 (1898).

[64] L. A. Girifalco and R. J. Good, J. Phys. Chem. **61**, 904 (1957).

[65] D. Owens and R. Wendt, J. Appl. Polym. Sci. **13**, 1741 (1969).

[66] D. H. Kaelble, Journal of adhesion **2**, 66 (1970).

[67] T. Tachibana, B. E. Williams, and J. T. Glass, Phys. Rev. B **45**, 11975 (1992).

[68] J. A. Garrido, A. Hardl, S. Kuch, M. Stutzmann, O. A. Williams, and R. B. Jackmann, Appl. Phys. Lett. **86** (2005).

[69] M. Daenen, O. A. Williams, J. D'Haen, K. Haenen, and M. Nesladek, Phys. Status Solidi A **203**, 3005 (2006).

[70] P. de Gennes, F. Brochard-Wyart, and D. Quere, Capillarity and Wetting Phenomena (Springer-Verlag, New York, 2004).

[71] L. Chen and F. C. Hong, Diamond Relat. Mater. **12**, 968 (2003).

[72] L. Ostrovskaya, V. Perevertailo, V. Ralchenko, A. Saveliev, and V. Zhuravlev, Diamond Relat. Mater. **16**, 2109 (2007).

[73] G. Strom, M. Fredriksson, and P. Stenius, J. Colloid Interface Sci. **119**, 352 (1987).

[74] G. Vazquez, E. Alvarez, and J. M. Navaza, J. Chem. Eng. Data **40**, 611 (1995).

[75] A. F. Azevedo, J. T. Matsushima, F. C. Vicentin, M. R. Baldan, and N. G. Ferreira, Appl. Surf. Sci. **255**, 6565 (2009).

[76] R. J. Nemanich, J. T. Glass, G. Lucovsky, and R. E. Shroder, J. Vac. Sci. Technol. A **6**, 1783 (1988).

[77] R. E. Shroder, R. J. Nemanich, and J. T. Glass, Phys. Rev. B **41**, 3738 (1990).

[78] W. A. Yarbrough and R. Messier, Science **247**, 688 (1990).

[79] A. C. Ferrari and J. Robertson, Phys. Rev. B **63**, 121405 (2001).

[80] C. Castiglioni, M. Tommasini, and G. Zerbi, Phil. Trans. R. Soc. London A **362**, 2425 (2004).

[81] T. Lopez-Rios, E. Sandre, S. Leclercq, and E. Sauvain, Phys. Rev. Lett. **76**, 4935 (1996).

[82] E. Ehrenfreund, Z. Vardeny, O. Brafman, and B. Horovitz, Phys. Rev. B **36**, 1535 (1987).

[83] D. K. Schroder, Semiconductor material and device characterization (John Wiley & Sons, New York, 1998).

[84] E. H. Hall, Amer. J. Math. **2**, 287 (1879).

[85] R. A. Smith, Semiconductors (Cambridge University Press, Cambridge, 1959).

[86] E. H. Putley, Contemp. Phys. **16**, 101 (1975).

[87] C. Uher and A. B. Kaiser, Phys. Lett. A **125**, 421 (1987).

[88] P. Wagner, D. Mazilu, L. Trappeniers, V. V. Moshchalkov, and Y. Bruynseraede, Phys. Rev. B **55**, 14721 (1997).

[89] K. Haenen, A. Lazea, J. Barjon, J. D'Haen, N. Habka, T. Teraji, S. Koizumi, and V. Mortet, J. Phys.: Condens. Matter **21**, 364204 (2009).

[90] J. Pernot, P. N. Volpe, F. Omnes, P. Muret, V. Mortet, K. Haenen, and T. Teraji, Phys. Rev. B **81**, 205203 (2010).

[91] I. Kim, K. S. Lee, T. S. Lee, J. H. Jeong, B. K. Cheong, Y. J. Baik, and W. M. Kim, J. Appl. Phys. **100**, 063701 (2006).

[92] W. Gajewski, P. Achatz, O. A. Williams, K. Haenen, E. Bustarret, M. Stutzmann, and J. Garrido, Phys. Rev. B **79**, 045206 (2009).

[93] P. Achatz, E. Bustarret, C. Marcenat, R. Piquerel, T. Dubouchet, C. Chapelier, A. M. Bonnot, O. A. Williams, K. Haenen, W. Gajewski, J. A. Garrido, and M. Stutzmann, Phys. Status Solidi A **206**, 1978 (2009).

[94] S. A. Grot, G. S. Gildenblat, C. W. Hatfield, C. R. Wronski, A. R. Badzian, T. Badzian, and R. Messier, IEEE Electron Device Lett. **11**, 100 (1990).

[95] S. D. Janssens, P. Pobedinskas, V. Petrakova, M. Nesladek, K. Haenen, and P. Wagner, MRS Proceedings **1282** (2011).

[96] W. Kulisch and C. Popov, Phys. Status Solidi A **203**, 203 (2006).

[97] J. Volger, Phys. Rev. **79**, 1023 (1950).

[98] J. Haeusler and H. J. Lippmann, Solid-State Electron. **11**, 173 (1968).

[99] D. W. Koon, Rev. Sci. Instrum. **61**, 2430 (1990).

[100] D. C. Look, Electrical Characterization of GaAs Materials and Devices (John Wiley & Sons, Chichester, 1989).

[101] N. Yom-Tov, C. Saguy, A. Bolker, R. Kalish, and Y. E. Yaish, J. Appl. Phys. **108**, 043711 (2010).

[102] T. Matsumura and Y. Sato, J. Mod. Phys. **1**, 340 (2010).

[103] P. Wagner, I. Gordon, A. Vantomme, D. Dierickx, M. J. V. Bael, V. V. Moshchalkov, and Y. Bruynseraede, Europhys. Lett. **41**, 49 (1998).

[104] Y. Komori, S. Sakuma, and T. Okamoto, Phys. Rev. Lett. **99** (2007).

[105] T. Klein, Z. Pribulova, R. Piquerel, H. Cercellier, J. Marcus, and C. Marcenat, Phys. Rev. B **83** (2011).

[106] J. J. Bissell, C. P. Ridgers, and R. J. Kingham, Phys. Rev. Lett. **105** (2010).

[107] S. L. Meyers, Data Analysis for Scientists and Engineers (Wiley, New York, 1975).

[108] V. Mortet, M. Nesladek, K. Haenen, A. Morel, M. D'Olieslaeger, and M. Vanecek, Diamond Relat. Mater. **13**, 1120 (2004).

[109] H. Shiomi, H. Nakahata, T. Imai, Y. Nishibayashi, and N. Fujimori, Jpn. J. Appl. Phys. 1 **28**, 758 (1989).

[110] G. S. Gildenblat, S. A. Grot, and A. Badzian, Proc. IEEE **79**, 647 (1991).

[111] V. Hnatowicz, J. Vacik, and D. Fink, Rev. Sci. Instrum. **81**, 073906 (2010).

[112] A. Kromka, L. Grausova, L. Bacakova, J. Vacik, B. Rezek, M. Vanecek, O. A. Williams, and K. Haenen, Diamond Relat. Mater. **19**, 190 (2010).

[113] J. Vacik, V. Hnatowicz, J. Cervena, S. Posta, U. Koster, and G. Pasold, AIP Conf. Proc. **1099**, 836 (2009).

[114] H. G. Jiang, M. Ruhle, and E. J. Lavernia, J. Mater. Res. **14**, 549 (1999).

[115] C. Wild, P. Koidl, W. Muller-Sebert, H. Walcher, R. Kohl, N. Herres, R. Locher, R. Samlenski, and R. Brenn, Diamond Relat. Mater. **2**, 158 (1993).

[116] B. D. Cullity and S. R. Stock, Elements of X-Ray Diffraction (Addison-Wesley, Reading, MA, 1956).

[117] G. K. Wertheim, Rev. Sci. Instrum. **45**, 1369 (1974).

[118] B. L. Willems, V. H. Dao, J. Vanacken, L. F. Chibotaru, V. V. Moshchalkov, I. Guillamon, H. Suderow, S. Vieira, S. D. Janssens, O. A. Williams, K. Haenen, and P. Wagner, Phys. Rev. B **80**, 224518 (2009).

[119] T. H. Borst and O. Weis, Diamond Relat. Mater. **4**, 948 (1995).

[120] T. Klein, P. Achatz, J. Kacmarcik, C. Marcenat, F. Gustafsson, J. Marcus, E. Bustarret, J. Pernot, F. Omnes, B. E. Sernelius, C. Persson, A. F. da Silva, and C. Cytermann, Phys. Rev. B **75**, 165313 (2007).

[121] J. J. Mares, P. Hubik, J. Kristofik, and M. Nesladek, Sci. Technol. Adv. Mater. **9**, 044101 (2008).

[122] C. E. Nebel, Semicond. Sci. Technol. **18**, S1 (2003).

[123] P. Achatz, W. Gajewski, E. Bustarret, C. Marcenat, R. Piquerel, C. Chapelier, T. Dubouchet, O. A. Williams, K. Haenen, J. A. Garrido, and M. Stutzmann, Phys. Rev. B **79**, 201203 (2009).

[124] I. S. Beloborodov, A. V. Lopatin, V. M. Vinokur, and K. B. Efetov, Rev. Mod. Phys. **79**, 469 (2007).

[125] R. Vansweevelt, V. Mortet, J. D'Haen, B. Ruttens, C. V. Haesendonck, B. Partoens, F. M. Peeters, and P. Wagner, Phys. Status Solidi A p. in press (2011).

[126] P. Sheng, Phys. Rev. B **21**, 2180 (1980).

[127] E. Bustarret, Phys. Status Solidi A **205**, 997 (2008).

[128] A. S. Barnard and M. Sternberg, J. Phys. Chem. B **110**, 19307 (2006).

[129] E. A. Ekimov, V. A. Sidorov, E. D. Bauer, N. N. Mel'nik, N. J. Curro, J. D. Thompson, and S. M. Stishov, Nature **428**, 542 (2004).

[130] Y. Takano, M. Nagao, I. Sakaguchi, M. Tachiki, T. Hatano, K. Kobayashi, H. Umezawa, and H. Kawarada, Appl. Phys. Lett. **85**, 2851 (2004).

[131] E. Bustarret, J. Kacmarcik, C. Marcenat, E. Gheeraert, C. Cytermann, J. Marcus, and T. Klein, Phys. Rev. Lett. **93** (2004).

[132] Z. L. Wang, Q. Luo, L. W. Liu, C. Y. Li, H. X. Yang, H. F. Yang, J. J. Li, X. Y. Lu, Z. S. Jin, L. Lu, and C. Z. Gu, Diamond Relat. Mater. **15**, 659 (2006).

[133] M. Nesladek, J. J. Mares, D. Tromson, C. Mer, P. Bergonzo, P. Hubik, and J. Kristofik, Sci. Technol. Adv. Mater. **7**, 41 (2006).

[134] G. Zhang, J. Vanacken, J. V. de Vondel, W. Decelle, J. Fritzsche, V. V. Moshchalkov, B. L. Willems, S. D. Janssens, K. Haenen, and P. Wagner, J. Appl. Phys. **108**, 013904 (2010).

[135] K. Winzer, D. Bogdanov, and C. Wild, Physica C **432**, 65 (2005).

[136] T. Yokoya, T. Nakamura, T. Matsushita, T. Muro, Y. Takano, M. Nagao, T. Takenouchi, H. Kawarada, and T. Oguchi, Nature **438**, 647 (2005).

[137] B. Sacepe, C. Chapelier, C. Marcenat, J. Kacmarik, T. Klein, F. Omnes, and E. Bustarret, Phys. Status Solidi A **203**, 3315 (2006).

[138] M. Ortolani, S. Lupi, L. Baldassarre, U. Schade, P. Calvani, Y. Takano, M. Nagao, T. Takenouchi, and H. Kawarada, Phys. Rev. Lett. **97** (2006).

[139] N. Dubrovinskaia, G. Eska, G. A. Sheshin, and H. Braun, J. Appl. Phys. **99** (2006).

[140] K. W. Lee and W. E. Pickett, Phys. Rev. Lett. **93** (2004).

[141] L. Boeri, J. Kortus, and O. K. Andersen, Phys. Rev. Lett. **93** (2004).

[142] X. Blase, C. Adessi, and D. Connetable, Phys. Rev. Lett. **93** (2004).

[143] H. J. Xiang, Z. Y. Li, J. L. Yang, J. G. Hou, and Q. S. Zhu, Phys. Rev. B **70** (2004).

[144] Y. Ma, J. S. Tse, T. Cui, D. D. Klug, L. Zhang, Y. Xie, Y. Niu, and G. Zou, Phys. Rev. B **72**, 014306 (2005).

[145] J. Bardeen, L. N. Cooper, and J. R. Schrieffer, Phys. Rev. **108**, 1175 (1957).

[146] Y. Shapira and G. Deutscher, Phys. Rev. B **27**, 4463 (1983).

[147] H. M. Jaeger, D. B. Haviland, B. G. Orr, and A. M. Goldman, Phys. Rev. B **40**, 182 (1989).

[148] K. Kagawa, K. Inagaki, and S. Tanda, Phys. Rev. B **53**, R2979 (1996).

[149] B. L. Willems, G. Zhang, J. Vanacken, V. V. Moshchalkov, S. D. Janssens, O. A. Williams, K. Haenen, and P. Wagner, J. Appl. Phys. **106**(3) (2009).

[150] B. L. Willems, G. Zhang, J. Vanacken, V. V. Moshchalkov, I. Guillamon, H. Suderow, S. Vieira, S. D. Janssens, K. Haenen, and P. Wagner, Physica C **470**, 853 (2010).

[151] W. Escoffier, C. Chapelier, N. Hadacek, and J. C. Villegier, Phys. Rev. Lett. **93** (2004).

[152] T. Nishizaki, Y. Takano, M. Nagao, T. Takenouchi, H. Kawarada, and N. Kobayashi, Physica C **460**, 210 (2007).

[153] B. van Grinsven, N. V. Bon, L. Grieten, M. Murib, S. D. Janssens, K. Haenen, E. Schneider, S. Ingebrandt, M. J. Schoning, V. Vermeeren, M. Ameloot, L. Michiels, R. Thoelen, W. D. Ceuninck, and P. Wagner, Lab Chip (2011).

[154] S. Wenmackers, S. D. Pop, K. Roodenko, V. Vermeeren, O. A. Williams, M. Daenen, O. Douheret, J. D'Haen, A. Hardy, M. K. V. Bael, K. Hinrichs, C. Cobet, M. vandeVen, M. Ameloot, K. Haenen, L. Michiels, N. Esser, and P. Wagner, Langmuir **24**, 7269 (2008).

[155] J. Pote, P. Rosse, W. Rosselli, V. T. Van, and W. Wildi, Chemosphere **61**, 677 (2005).

[156] E. A. Tindall, D. C. Petersen, P. Woodbridge, K. Schipany, and V. M. Hayes, Human Mutation **30**, 876 (2009).

[157] M. Bonnauron, S. Saada, C. Mer, C. Gesset, O. A. Williams, L. Rousseau, E. Scorsone, P. Mailley, M. Nesladek, J. C. Arnault, and P. Bergonzo, Phys. Status Solidi A **205**, 2126 (2008).

Publications

Journals

1. **S.D. Janssens**, S. Drijkoningen, M. Saitner, H.-G. Boyen, K. Haenen, P. Wagner, 'The surface energy of hydrogen terminated nanocrystalline CVD diamond', submitted to Chemical Physics Letters (2011).

2. **S.D. Janssens**, K. Haenen, P. Wagner, 'How to deal with noisy Hall effect measurements', submitted to Physica Status Solidi (a) (2011).

3. V. Petrak, L. Grieten, A. Taylor, F. Fendrych, M. Ledvina, **S.D. Janssens**, M. Nesladek, K. Haenen, P. Wagner, 'Peptide induced disruption of artificial lipid membranes constructed on boron doped nanocrystalline diamond - in situ impedimetric study', submitted to Physica Status Solidi (a) (2011).

4. L. Grieten, **S.D. Janssens**, A. Ethirajan, N. Vanden Bon, M. Ameloot, L. Michiels, K. Haenen, P. Wagner, 'Real-time study of protein adsorptionon thin nanocrystalline diamond', submitted to Physica Status Solidi (a) (2011).

5. **S.D. Janssens**, P. Pobedinskas, J. Vacik, V. Petrakova, B. Ruttens, J. D'Haen, M. Nesladek, K. Haenen, P. Wagner, 'Separation of the intra- and intergranular magnetotransport properties in nanocrystalline diamond films on the metallic side of the metal-insulator transition', submitted to New Journal of Physics (2011).

6. V. Vermeeren, L. Grieten, N. Vanden Bon, N. Bijnens, S. Wenmackers, **S.D. Janssens**, K. Haenen, P. Wagner, L. Michiels, 'Real-time impedimetric detection of C-Reactive protein with a diamond-based immunosensor', Sensors & Actuators B: Chemical, in press (2011).

7. B. van Grinsven, N. Vanden Bon, L. Grieten, M. Murib, **S.D. Janssens**, K. Haenen, E. Schneider, S. Ingebrandt, M.J. Schoning, V. Vermeeren, M. Ameloot, L. Michiels, R. Thoelen, W. De Ceuninck, P. Wagner, 'Rapid assessment of the stability of DNA duplexes by impedimetric real-time monitoring of chemically induced denaturation', Lab on a Chip 11/9, 1656-1663 (2011).

8. T. Clukers, B. Van Grinsven, T. Vandenryt, **S.D. Janssens**, P. Wagner, W. De Ceuninck, R. Thoelen, M. Daenen, K. Haenen, 'Boron doped nanocrystalline diamond temperature regulator for sensing application', Physica Status Solidi (a) 207/9, 2110-2113 (2010).

9. B.L. Willems, G. Zhang, J. Vanacken, V.V. Moshchalkov, **S.D. Janssens**, K. Haenen, P. Wagner, 'Granular superconductivity in metallic and insulating nanocrystalline boron-doped diamond films', Journal of Physics D: Applied Physics 43/37, 374019 (2010). [Invited Article-Cluster issue on Carbon Related Nano-Materials and Nanotechnology]

10. B.L. Willems, G. Zhang, J. Vanacken, V.V. Moshchalkov, I. Guillamon, H. Suderow, S. Vieira, **S.D. Janssens**, K. Haenen, P. Wagner, 'In/extrinsic granularity in superconducting boron-doped diamond', Physica C: Superconductivity and its Applications 470/19, 853-856 (2010).

11. G. Zhang, J. Vanacken, J. Van de Vondel, W. Decelle, J. Fritzsche, V.V. Moshchalkov, B.L. Willems, **S.D. Janssens**, K. Haenen, P. Wagner, 'Magnetic field-driven super-conductor-insulator transition in boron doped nanocrystalline CVD diamond', Journal of Applied Physics 108/1, 013904 (2010).

12. C.H.Y.X.L. Lim, Y.L. Zhong, **S.D. Janssens**, M. Nesladek, K.P. Loh, 'Oxygen-Terminated Nanocrystalline Diamond Film as an Efficient Anode in Photovoltaics', Advanced Functional Materials 20, 1313-1318 (2010).

13. B.L. Willems, V.H. Dao, J. Vanacken, L.F. Chibotaru, V.V. Moshchalkov, I. Guillamon, H. Suderow, S. Vieira, **S.D. Janssens**, O.A. Williams, K. Haenen, P. Wagner, 'Intrinsic granularity in nanocrystalline boron-doped diamond films measured by scanning tunneling microscopy', Physical Review B 80/22, 224518 (2009). [See also Virtual Journal of Nanoscale Science & Technology 21/2 (2010)]

14. B.L. Willems, G. Zhang, J. Vanacken, V.V. Moshchalkov, **S.D. Janssens**, O.A. Williams, K. Haenen, P. Wagner, 'Negative magnetoresistance in boron-doped nanocrystalline diamond films', Journal of Applied Physics 106/3, 033711 (2009).

Proceedings

1. P. Pobedinskas, **S.D. Janssens**, J. Hernando-Garcia, P. Wagner, M. Nesladek, K. Haenen, 'Selective Seeding and Growth of Nanocrystalline CVD Diamond on Non-Diamond Substrates', MRS Symposium Proceedings (Spring Meeting, San Fancisco, 2011), in press.

2. **S.D. Janssens**, S. Drijkoningen, M. Saitner, H.-G. Boyen, K. Haenen, P. Wagner, 'The surface energy of hydrogen terminated nanocrystalline CVD diamond', MRS Symposium Proceedings (Spring Meeting, San Fancisco, 2011), in press.

3. **S.D. Janssens**, P. Pobedinskas, V. Petrakova, M. Nesladek, K. Haenen, P. Wagner, 'Influence of methane concentration on the electric transport properties in heavily boron doped nanocrystalline CVD diamond films', MRS Symposium Proceedings Volume 1282 (2011), 1282-a15-04. In 'Diamond Electronics and Bioelectronics − Fundamentals to Applications IV', eds. P. Bergonzo, J.E. Butler, C.E. Nebel, M. Nesladek, A.T.S. Wee.

4. T. Clukers, B. Van Grinsven, T. Vandenryt, **S.D. Janssens**, P. Wagner, W. De Ceuninck, R. Thoelen, M. Daenen, K. Haenen, 'Optimization of a boron doped nanocrystalline diamond temperature regulator for sensing applications', MRS Symposium Proceedings Volume 1282, 1282-a11-05 (2011). In 'Diamond Electronics and Bioelectronics − Fundamentals to Applications IV', eds. P. Bergonzo, J.E. Butler, C.E. Nebel, M. Nesladek, A.T.S. Wee.

5. M. Backer, A. Poghossian, M.H. Abouzar, S. Wenmackers, **S.D. Janssens**, K. Haenen, P. Wagner, M.J. Schoning, 'Capacitive field-effect (bio-)chemical sensors based on nanocrystalline diamond films', MRS Symposium Proceedings Volume 1203, 1203-J17-31, 173-178 (2010). In 'Diamond Electronics and Bioelectronics − Fundamentals to Applications III', eds. P. Bergonzo, J.E. Butler, R.B. Jackman, K.P. Loh, M. Nesladek.

Abstracts

Oral presentations

1. Participation on invitation: **S.D. Janssens**, P. Pobedinskas, J. Vacik, V. Petrakova, J. D'Haen, M. Nesladek, P. Wagner, K. Haenen, 'Separation of the intra- and intergranular magnetotransport properties in heavily B-doped nanocrystalline CVD diamond films', 62^{nd} Diamond Conference, University of Warwick, Warwick, UK, July 4-7, 2011.

2. B. Van Grinsven, N. Vanden Bon, L. Grieten, H. Strauven, B. Geerets, **S.D. Janssens**, K. Haenen, S. Ingebrandt, M.J. Schoning, V. Vermeeren, M. Ameloot, L. Michiels, R. Thoelen, W. De Ceuninck, P. Wagner, 'Detecting single nucleotide polymorphisms by impedimetric monitoring of denaturation', the general scientific meeting 2011 of the Belgian Physical Society, University of Namur, Namur, Belgium, May 25, 2011.

3. P. Pobedinskas, **S.D. Janssens**, J. Hernano-Garcia, P. Wagner, M. Nesladek, K. Haenen, 'Selective Seeding and Growth of Nanocrystalline CVD Diamond on Non-Diamond Substrates', MRS Spring Meeting, San Francisco, 2011.

4. Yinggang Lu, J. Verbeeck, G.Van Tendeloo, C.De Dobbelaere, A. Hardy, M. K. Van Bael, **S.D. Janssens**, P. Wagner, K. Haenen, 'The role of TiO_2 on the nucleation process of CVD grown diamond studied by TEM', MRS Spring Meeting, San Francisco, 2011.

5. **S.D. Janssens**, P. Pobedinskas, J. Vacik, V. Petrakova, J. D'Haen, M. Nesladek, P. Wagner, K. Haenen, 'Magnetotransport: fundamentals and application to heavily B-doped NCD', MATCON (Materials and Interfaces for Energy Storage and Conversion) summer school (FP7-ITN-project), University of Oxford, March 28-April 1, 2011.

6. V. Petrak, L. Grieten, A. Taylor, F. Fendrych, M. Ledvina, **S.D. Janssens**, M. Nesladek, K. Haenen, P. Wagner, 'Peptide induced disruption of artificial lipid membranes constructed on boron doped nanocrystalline diamond − in situ impedi-

metric study', Hasselt Diamond Workshop 2011 − SBDD XVI, cultuurcentrum Hasselt, Hasselt, Belgium, February 21-23, 2011.

7. R. Salenbien, B. Verstraeten, P. Pobedinskas, **S.D. Janssens**, C. Glorieux, K. Haenen, 'Thin nanocrystalline CVD diamond films for micro-channel cooling: thermal and elastic properties', MRS 2010 Fall Meeting, Hynes Convention Center & Sheraton Boston Hotel, Boston, MA, USA, November 29-December 3, 2010.

8. T. Clukers, B. Van Grinsven, T. Vandenryt, **S.D. Janssens**, P. Wagner, W. De Ceuninck, R. Thoelen, M. Daenen, K. Haenen, 'Optimization of a boron doped nanocrystalline diamond temperature regulator for sensing applications', MRS 2010 Fall Meeting, Hynes Convention Center & Sheraton Boston Hotel, Boston, MA, USA, November 29-December 3, 2010.

9. **S.D. Janssens**, K. Haenen, G. Zhang, B. Willems, J. Vacik, H. Suderow, J. Vanacken, V.V. Moshchalkov, P. Wagner, 'Boron-doping of nanocrystalline diamond: from insulator to superconductor', Interuniversity Attraction Poles (IAP), Diepenbeek, 2010.

10. R. Salenbien, B. Verstraeten, P. Pobedinskas, **S.D. Janssens**, C. Glorieux, K. Haenen, 'Thermal and elastic properties of thin nanocrystalline CVD diamond films', 21st European Conference on Diamond, Diamond-like Materials, Carbon Nanotubes, and Nitrides, Kempinski Hotel Corvinus Budapest, Budapest, Hungary, September 5-9, 2010.

11. **S.D. Janssens**, S. Drijkoningen, M. Saitner, H.-G. Boyen, K. Haenen, P. Wagner, 'The surface energy of hydrogen terminated nanocrystalline CVD diamond derived from contact angle measurements', Engineering of Functional Interfaces 2010 (EnFI 2010), Philipps Universitat Marburg, Marburg, Germany, July 15-16, 2010.

12. L. Grieten, **S.D. Janssens**, N. Vanden Bon, J. Bex, B. van Grinsven, V. Vermeeren, W. De Ceuninck, K. Haenen, M. Ameloot, L. Michiels, P. Wagner, 'Coplanar diamond electrodes for the label-free detection of proteins', Engineering of Functional Interfaces 2010 (EnFI 2010), Philipps Universitat Marburg, Marburg, Germany, July 15-16, 2010.

13. K. Haenen, L. Zhang, M. Daenen, **S.D. Janssens**, A. Hardy, J. Verbeeck, M.K. Van Bael, G. Van Tendeloo, M. Nesladek, 'SEM, TEM and EELS study of diamond: growth mechanism', MRS 2009 Fall Meeting, Hynes Convention Center & Sheraton Boston Hotel, Boston, MA, USA, November 30-December 4, 2009.

14. Invited presentation: S. Wenmackers, V. Vermeeren, S.D. Pop, A. Riskin, R. Vansweevelt, L. Grieten, **S.D. Janssens**, A. Hardy, M.K. Van Bael, C. Cobet, N. Esser, M. Ameloot, L. Michiels, K. Haenen, P. Wagner, 'Biosensors on diamond, silicon and carbon-nanowalls', MRS 2009 Fall Meeting, Hynes Convention Center & Sheraton Boston Hotel, Boston, MA, USA, November 30-December 4, 2009.

15. K. Haenen, M. Daenen, L. Zhang, **S.D. Janssens**, P. Cosemans, A. Hardy, J. Verbeeck, M.K. Van Bael, M. Nesladek, G. Van Tendeloo, 'Thin nanocrystalline CVD diamond films based on nanodiamond/TiO_2 sol-gel composites', Innovations in Thin Films Processing and Characterisation 2009 (ITFPC09), Amphitheatre 8, Faculte des Sciences et Techniques, Universite Henri Poincare Nancy I, Nancy, France, November 17-20, 2009.

16. **S.D. Janssens**, O.A. Williams, K. Haenen, P. Wagner, V.H. Dao, L. Chibotaru, B.L. Willems, J. Vanacken, V.V. Moshchalkov, 'Scanning tunnelling microscopy/spectroscopy and magnetoresistance measurements on heavily boron-doped nanocrystalline diamond', 20th European Conference on Diamond, Diamond-like Materials, Carbon Nanotubes, and Nitrides, Athens Ledra Marriott, Athens, Greece, September 6-10, 2009.

17. A. Taylor, I. Kratochvilova, Y. Liang, A. Kruger, **S.D. Janssens**, F. Fendrych, K. Haenen, P. Wagner, M. Nesladek, 'Raman and luminescence imaging of treated nanodiamond particles', 20th European Conference on Diamond, Diamond-like Materials, Carbon Nanotubes, and Nitrides, Athens Ledra Marriott, Athens, Greece, September 6-10, 2009.

18. W. Wenmackers, V. Vermeeren, L. Grieten, **S. Janssens**, L. Michiels, K. Haenen, S.D. Pop, K. Hinrichs, N. Esser, P. Wagner, 'Covalent coupling of nucleic acids and antibodies to semiconductors: enabling techniques for label-free real-time biosensors', Prague Congress Centre, European and International Forum on Nanotechnology-EuroNanoForum 2009 'Nanotechnology for Sustainable Economy', Prague, Czech Republic, June 2-5, 2009.

19. V. Petrak, A. Kruger, **S.D. Janssens**, I. Gregora, I. Kratochvilova, F. Fendrych, K. Haenen, P. Wagner, M. Nesladek, 'Tip-enhanced Raman and luminescence imaging of treated nanodiamond particles', Hasselt Diamond Workshop 2009-SBDD XIV, cultuurcentrum Hasselt, Hasselt, Belgium, March 2-4, 2009.

20. O.A. Williams, **S. Janssens**, V. Mortet, M. Daenen, K. Haenen, 'The diamond microbalance', 19th European Conference on Diamond, Diamond-like Materials, Carbon Nanotubes, and Nitrides, Melia Sitges Hotel, Sitges, Spain, September 7-11, 2008.

21. B.L. Willems, **S. Janssens**, O. Williams, J. Vanacken, V.V. Moshchalkov, K. Haenen, M. Daenen, P. Wagner, 'Transport properties of ultra thin boron-doped diamond samples', BPS General Scientific Meeting 2008, Universite Libre de Bruxelles, Brussels, Belgium, May 21, 2008.

22. Participation on invitation: A. Taylor, I. Kratochvilova, Y. Liang, A. Kruger, **S.D. Janssens**, F. Fendrych, K. Haenen, P. Wagner, M. Nesladek, 'Raman and luminescence imaging of treated nanodiamond particles', 60th Diamond Conference, University of Warwick, Warwick, UK, July 7-10, 2009.

Poster presentations

1. L. Grieten, **S.D. Janssens**, T. Vandenryt, N. Vanden Bon, V. Vermeeren, K. Haenen, M. Ameloot, L. Michiels, P. Wagner, 'Do diamond an proteins like each other?', Biomedica, Eindhoven, 2011.

2. **S.D. Janssens**, S. Drijkoningen, M. Saitner, H.-G. Boyen, P. Wagner and K. Haenen, 'The diamond-solution interface: the surface energy of hydrogen terminated nanocrystalline CVD diamond derived from contact angle measurements", MRS Spring Meeting, San Francisco, 2011.

3. L. Grieten, **S.D. Janssens**, V. Vermeeren, N. Vanden Bon, W. De Ceuninck, M. Ameloot, K. Haenen, L. Michiels, P. Wagner, 'Immunosensing based on patterned B-doped NCD electrodes', MRS Spring Meeting, San Francisco, 2011.

4. N. Vanden Bon, V. Vermeeren, B. Van Grinsven, L. Grieten, **S.D. Janssens**, D.T. Tran, J. Lammertyn, M. Ameloot, K. Haenen, W. De Ceuninck, P. Wagner, L. Michiels, 'The use of diamond as a flexible surface for the attachment of different bioreceptors in the development of impedimetric biosensors', MRS 2011 Spring Meeting, Moscone West & San Francisco Marriott, San Francisco, CA, USA, April 25-29, 2011.

5. **S.D. Janssens**, K. Haenen and P. Wagner, 'The influence of contacts on Hall effect measurements performed on a heavily boron-doped nanocrystalline diamond film', Hasselt Diamond Workshop2011 − SBDD XVI, cultuurcentrum Hasselt, Hasselt, Belgium, February 21-23, 2011.

6. B. van Grinsven, N. Vanden Bon, M. Backer, V. Vermeeren, L. Michiels, **S.D. Janssens**, K. Haenen, P. Wagner, M.J. Schoning, 'NCD − electrodes for probing the stability of DNA duplexes by electronic denaturation monitoring', Hasselt Diamond Workshop 2011 − SBDD XVI, cultuurcentrum Hasselt, Hasselt, Belgium, February 21-23, 2011.

7. Y. Lu, J. Verbeeck, C. De Dobbelaere, A. Hardy, M.K. Van Bael, **S.D. Janssens**, P. Wagner, K. Haenen, G. Van Tendeloo, 'TEM investigation on the role of TiO_2 on the nucleation process of CVD grown diamond', Hasselt Diamond Workshop 2011 − SBDD XVI, cultuurcentrum Hasselt, Hasselt, Belgium, February 21-23, 2011.

8. L. Grieten, **S.D. Janssens**, M. Saitner, B. Conings, R. Thoelen, T. Cleij, H.-G. Boyen, K. Haenen, P. Wagner, 'Probing the electrochemical properties in function of grain-sizes in diamond films', Hasselt Diamond Workshop 2011 − SBDD XVI, cultuurcentrum Hasselt, Hasselt, Belgium, February 21-23, 2011.

9. G. Zhang, **S.D. Janssens**, J. Vanacken, J. Van de Vondel, B.L. Willems, W. Decelle, J. Fritzsche, I. Guillamon, H. Suderow, S. Vieira, K. Haenen, P. Wagner, V.V. Moshchalkov, 'Granular nature of the transport properties in superconducting boron-doped CVD diamond', MRS 2010 Fall Meeting, Hynes Convention Center & Sheraton Boston Hotel, Boston, MA, USA, November 29-December 3, 2010.

10. V. Petrak, P. Cigler, M. Ledvina, V. Rezacova, J. Masek, J. Turanek, **S.D. Janssens**, K. Haenen, M. Nesladek, 'Ionic strength as a driving force of nanodiamond aggregation in aqueous solution', MRS 2010 Fall Meeting, Hynes Convention Center & Sheraton Boston Hotel, Boston, MA, USA, November 29-December 3, 2010.

11. **S.D. Janssens**, S. Drijkoningen, M. Saitner, H.-G. Boyen, K. Haenen, P. Wagner, 'The surface energy of hydrogen terminated nanocrystalline CVD diamond derived from contact angle measurements', Engineering of Functional Interfaces 2010 (EnFI 2010), Philipps Universitat Marburg, Marburg, Germany, July 15-16, 2010.

12. L. Grieten, **S.D. Janssens**, N. Vanden Bon, J. Bex, B. van Grinsven, V. Vermeeren, W. De Ceuninck, K. Haenen, M. Ameloot, L. Michiels, P. Wagner, 'Coplanar diamond electrodes for the label-free detection of proteins', Engineering of Functional Interfaces 2010 (EnFI 2010), Philipps Universitat Marburg, Marburg, Germany, July 15-16, 2010.

13. **S.D. Janssens**, K. Haenen, P. Wagner, 'Boron-doped nanocrystalline diamond films deposited under variable methane/hydrogen ratios', 4th International Conference on New Diamond and Nano Carbons (NDNC2010), Garden Hotel, Suzhou, China, May 16-20, 2010.

14. L. Grieten, **S.D. Janssens**, V. Vermeeren, N. Vanden Bon, B. Vangrinsven, W. De Ceuninck, K. Haenen, M. Ameloot, L. Michiels, P. Wagner, 'Immunosensing based on patterned B-doped NCD electrodes', Hasselt Diamond Workshop 2010-SBDD XV, cultuurcentrum Hasselt, Hasselt, Belgium, February 22-24, 2010.

15. M. Backer, A. Poghossian, M. H. Abouzar, **S.D. Janssens**, K. Haenen, P. Wagner, M.J. Schoning, 'Nanocrystalline diamond films as transducer material for capacitive field-effect (bio-)chemical sensors', Hasselt Diamond Workshop 2010-SBDD XV, cultuurcentrum Hasselt, Hasselt, Belgium, February 22-24, 2010.

16. G. Zhang, J. Vanacken, J. Van de Vondel, W. Decelle, J. Fritzsche, V.V. Moshchalkov, **S.D. Janssens**, K. Haenen, P. Wagner, 'Magnetic field driven superconductor-insulator transition in boron doped granular diamond', Hasselt Diamond Workshop 2010-SBDD XV, cultuurcentrum Hasselt, Hasselt, Belgium, February 22-24, 2010.

17. T. Clukers, T. Vandenryt, B. van Grinsven, **S.D. Janssens**, P. Wagner, R. Thoelen, M. Daenen, W. De Ceuninck, K. Haenen, 'Boron doped nanocrystalline diamond thermistor for bio sensing applications', Hasselt Diamond Workshop 2010-SBDD XV, cultuurcentrum Hasselt, Hasselt, Belgium, February 22-24, 2010.

18. **S.D. Janssens**, P. Pobedinskas, K. Haenen, P. Wagner, 'The influence of methane on the boron incorporation and resistivity in B-doped nanocrystalline diamond films', Hasselt Diamond Workshop 2010-SBDD XV, cultuurcentrum Hasselt, Hasselt, Belgium, February 22-24, 2010.

19. **S.D. Janssens**, P. Pobedinskas, V. Mortet, K. Haenen, P. Wagner, 'The influence of methane concentration on the structure and transport properties of B-doped

nanocrystalline CVD diamond films', MRS 2009 Fall Meeting, Hynes Convention Center & Sheraton Boston Hotel, Boston, MA, USA, November 30-December 4, 2009.

20. R. Salenbien, C. Glorieux, P. Pobedinskas, **S.D. Janssens**, V. Mortet, K. Haenen, 'Determination of the thermo-elastic properties of thin nanocrystalline CVD diamond films for heat spreading applications', 15th International Workshop on Thermal Investigations on ICs and Systems-Therminic 2009, Leuven, Belgium, October 7-9, 2009.

21. B.L. Willems, G. Zhang, J. Vanacken, V.V. Moshchalkov, H. Suderow, **S.D. Janssens**, K. Haenen, P. Wagner, 'In/extrinsic granularity in superconducting boron-doped diamond', Sixth International Conference in School Format on Vortex Matter in Nanostructured Superconductors (VORTEX VI), Aldemar Paradise Royal Mare, Rhodes, Greece, September 17-24, 2009.

22. **S.D. Janssens**, P. Pobedinskas, V. Mortet, K. Haenen, P. Wagner, 'The influence of methane on the boron incorporation in B-doped nanocrystalline diamond films', 20th European Conference on Diamond, Diamond-like Materials, Carbon Nanotubes, and Nitrides, Athens Ledra Marriott, Athens, Greece, September 6-10, 2009.

23. **S.D. Janssens**, O.A. Williams, K. Haenen, P. Wagner, V.H. Dao, L. Chibotaru, B.L. Willems, J. Vanacken, V.V. Moshchalkov, 'A non-BCS temperature dependence of the superconducting gap in nanocrystalline B-doped CVD diamond films', Hasselt Diamond Workshop 2009-SBDD XIV, cultuurcentrum Hasselt, Hasselt, Belgium, March 2-4, 2009.

24. **S.D. Janssens**, B. Willems, O.A. Williams, K. Haenen, J. D'Haen, J. Vanacken, V.V. Moshchalkov, P. Wagner, 'Preparation and characterisation of superconducting diamond films', BPS General Scientific Meeting 2008, Universite Libre de Bruxelles, Brussels, Belgium, May 21, 2008.

25. B.L. Willems, J. Vanacken, V.V. Moshchalkov, O.A. Williams, M. Daenen, **S. Janssens**, K. Haenen, P. Wagner, 'Transport properties of ultra thin boron doped diamond samples: metal to variable range hoping (VRH) to superconducting (SC) transitions', Hasselt Diamond Workshop 2008-SBDD XIII, cultuurcentrum Hasselt, Hasselt, Belgium, February 25-27, 2008.

26. **S.D. Janssens**, F. De Proft, P. W. Ayers and P. Geerlings, 'Thermal and Photochemical Electrocyclisation Reactions: Woodward-Hoffmann rules vs. DFT based Reactivity Indices and Principles', Chemical Reactivity Conference, Brussels, Belgium, 2006.